

22 Novembre 2005

IPNO-T-05-11

Thèse

présentée par **GIBELIN Julien**

pour obtenir le grade de

Docteur de l'Université Paris XI

**Search for low lying dipole strength
in the neutron rich nucleus ^{26}Ne**

THÈSE de DOCTORAT
de
L'UNIVERSITÉ PARIS XI

Spécialité :

Physique Nucléaire

présentée par :

GIBELIN Julien

Pour obtenir le grade de :

DOCTORAT de l'UNIVERSITÉ PARIS XI

Sujet de thèse:

Search for low lying dipole strength
in the neutron rich nucleus ^{26}Ne

Soutenue le 22 Novembre 2005

devant le jury composé de :

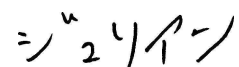
Prof. Tiina SUOMIJARVI	(Présidente)
Dr. Thomas AUMANN	(Rapporteur)
Dr. Didier BEAUMEL	(Examineur)
Dr. Yorick BLUMENFELD	(Directeur de Thèse)
Dr. Alain GILLIBERT	(Rapporteur)
Prof. Tohru MOTOBAYASHI	(Examineur)

Acknowledgment

L'écriture des remerciements est reconnue comme une tâche difficile mais ô combien satisfaisante, puisque qu'elle se déroule une fois toutes difficultés surmontées. De loin la partie la plus personnelle, il apparaîtra normal à ceux qui me connaissent que je ne peux m'empêcher de la compliquer un peu plus en voulant l'écrire dans trois langues différentes. Que l'on veuille cependant bien m'excuser, les détails des remerciements se situent uniquement dans la partie anglaise. Ainsi dans ma langue maternelle, comme en Japonais, je serai bref et me contenterai de remercier l'ensemble de mes collaborateurs pour leur gentillesse, leur patience, leur aide et leur conseils qui ont permis, lors de ces trois années, la réalisation de tous mes projets.



全ての方にうまく感謝の辞を述べる事はたやすいことではありませんが、全ての困難を乗り越えた後にこのようにお礼を申し上げることができ大変感謝しています。最も個人的ではありますが、今までの経験から考え3カ国語でさせて頂くのが最もだという考えに至りました。誠に勝手ながら感謝の詳細については英語だけで述べさせていただきます。母国語と日本語においては3年間に及ぶ計画の再現に関して全ての協力者と関係者の心遣い、忍耐、援助、助言に手短にお礼を申し上げます。



These acknowledgments present a main difficulty linked to the nature of this work: experimental nuclear physics is most of the time the work of a group and the Franco/Japanese collaboration multiply the number of collaborators and friends I am thankful to by a factor two. Despite the distances and the differences I owe equally to the French and the Japanese research teams which strongly supported me. I also wanted this part to be vivid and personal and I could not avoid explanations and anecdotes on how this thesis saw the light of day.

First and foremost I would like to express my deep and sincere gratitude to my two *unofficial* supervisors, Dr. Didier Beaumel & Pr. Tohru Motobayashi. Didier you helped me at first to spend my three month training period of Magistère in Japan. It was a great experience and by chance an experiment in the domain I was interested in was already accepted at Riken... During that period I meet Motobayashi-*sensei* who also welcomed this collaboration and everything could start. Both of you gave me more than useful advice and discussions by trusting me and I thank you.

I am deeply grateful to my three (!) official supervisors, Dr. Yorick Blumenfeld, Dr. Simone Fortier & Pr. Kazuoshi Kurita. Now why *three*? Simone was enough kind to accept at first to make the link with university, without which nothing would have been possible. Circumstances made Yorick my second official supervisor in France in addition to being a participant to the experiment and the analysis. Yorick, I owe you also for revising the English of my manuscript. I should not forget to mention the good ambiance that sharing your office can create. I had the chance to belong to Rikkyo University during one year with Pr. Kazuoshi Kurita as supervisor. Kurita-*sensei*, you made this collaboration a real international adventure and letting me being an English-speaking Teaching Assistant for laboratory courses is an experience I will never forget (and neither will my Japanese students!).

I wish to express my warm and sincere thanks to two more professors for their availability and soundness: Pr. Nimet Frascaria, whose support and

confidence made everything start six years ago, and Pr. Takashi Nakamura without who a huge part of the experiment and analysis would have not been possible.

I owe my most sincere gratitude to the referees, Dr. Thomas Aumann & Dr. Alain Gillibert for their detailed review, constructive criticism and excellent advice and Pr. Tiina Suomijärvi, who initiated the experiment many years ago, for presiding this jury.

My warm thanks are due to Dr. Naoki Fukuda, Dr. Tomoko Gomi, Dr. Toshiyuki Kubo, Dr. Yoshiteru Satou, Dr. Satoshi Takeuchi, Dr. Yoshiyuki Yanagisawa & Dr. Koichi Yoshida for their guidance and discussion before, during and after my experiment. This experiment would have not been possible without the help of my colleagues and friends: Dr. Hidetada Baba, Dr. Zoltan Elekes, Kazuhiro Ishikawa, Dr. Victor Lima, Akito Saito, Takashi Sugimoto, Eri Takeshita aka ‘Erippa’, Dr. Takashi Teranishi, Yasuhiro Togano & Dr. A. M. Vinodkumar.

My sincere thanks are due to Pr. Ma, Dr. Li-Gang Cao, Dr. Elias Khan, Dr. Jérôme Margueron, Dr. Sophie Péru, Dr. “Jass” Scarpaci & Pr. Peter Ring for helping me understand theory and for sharing with me their latest results. I warmly thank Dr. Laurence Lavergne, Valerie Le Ven & Mikael Le Fur for their work on the detectors.

I do not want to forget the kindness, the support and the fruitful discussions I had with Pr. Takato Hirayama, Dr. Nobuaki Imai, Dr. Meiko Kurokawa, Dr. Ken-ichiro Yoneda, Dr. Kazunari Yamada and Pr. Susumu Shimoura during my two years in Japan & Dr. Pierre Desesquelles, Dr. Azaiez Faical, Dr. Jacques Guillot & Dr. Jürgen Kiener during my stay in France.

I warmly thank Pr. Zsolt Dombrádi, Dr. Zsolt Fülöp, Pr. Hans Hemling & Dr. Przemyslaw Adrich for their interesting discussion and advice.

During this work I have collaborated with many colleagues for whom I have great regard, and I wish to extend my warmest thanks to all those who have helped me with my work in Riken, at the Institut de Physique Nucléaire d’Orsay, in the Departments of Physics of Rikkyo University, of

Tokyo Institute of Technology, of Tokyo University, in Atomki (Debrecen), in the Centre de Spectrométrie Nucléaire et de Spectrométrie de Masse (Orsay), in the Dapnia (CEA Saclay) & at Bruyères-le-Châtel (CEA).

I wish a very good luck to my fellow students: Emilie, Sophie, Alexandre, Baba-*san*, Laurent & Yamada-*san* for their future research and Charlotte, Erippa, Kanchan, Marlène, Albert, Jin-*kun*, Kondo-*kun*, Mathieu, Saito-*san*, Sugimoto-*san* & Togano-*kun* to reach the end of their thesis.

I am grateful to Anne-Marie Dujardin, Tomoko Iwanami & Rie Kuwana for their sympathetic help in secretarial work.

My special gratitude is due to my parents for their loving support. I owe my loving thanks to my wife: without her patience, encouragement and understanding it would have been impossible for me to finish this work.

The work have been financially supported by the French Ministry of Foreign Office through a Lavoisier Scholarship , the Consortium Japonais du Collège doctoral Franco-Japonais & by the CNRS *via* a Doctor/Engineer Scholarship (BDI).



Table of Contents

Acknowledgment	iv
Introduction	1
I Giant resonances: from stable to unstable nuclei	2
I.1 Overview on Giant Resonances	2
I.1.1 Macroscopic picture	3
I.1.2 Microscopic picture	4
I.1.3 Damping of Giant Resonances	6
I.1.4 Collectivity, sum rule	7
I.1.5 Giant Dipole Resonances	7
I.2 Collective excitations in neutron rich nuclei	9
I.2.1 Dipole excitation and sum rule evolution	9
I.2.2 Prediction of low lying dipole strength in ^{26}Ne	12
I.3 Experimental considerations	13
I.3.1 Virtual photon method	14
I.3.2 DWBA	17
I.3.3 ^{26}Ne decays of resonances	18
I.3.4 Invariant mass method	19
II Experimental Setup	22
II.1 Production of Secondary Beams	22

Table of Contents

II.1.1	The RIKEN Projectile fragment Separator (RIPS) . . .	22
II.1.2	Production of the ^{26}Ne beam	25
II.1.3	Cyclotrons tuning and radio frequency	26
II.2	Detection System at F3 focal point	26
II.2.1	Beam line counters and Targets	27
II.2.2	Hodoscope for Outgoing Fragments	30
II.2.3	Gamma-ray Detector	31
II.2.4	Neutron Wall	33
II.3	Electronics and Data Acquisition	36
II.3.1	Triggers	36
II.3.2	Data Acquisition System (DAQ)	39
II.3.3	Data sets	40
III	Data Analysis	42
III.1	Beam	42
III.1.1	Particle Identification	43
III.1.2	PPAC calibration and beam profile	44
III.1.3	Alignment	46
III.2	γ -rays	48
III.2.1	Energy calibration	49
III.2.2	Photo-peak efficiency	50
III.2.3	Doppler shift correction	52
III.2.4	Background reduction via time gate	54
III.2.5	Resolution and accuracy	56
III.3	Silicon detectors	59
III.3.1	Energy calibration and resolution	59
III.3.2	Particle Identification (PID)	61
III.3.3	Geometrical acceptance	62
III.4	Neutron detection	63
III.4.1	Neutron detectors calibration	64
III.4.2	Energy calibration of light output	64
III.4.3	Time calibration	66

III.4.4 Slew (walk) correction	70
Description	70
Slew correction procedure	72
III.4.5 Position calibration	73
III.4.6 Efficiency and Angular acceptance	74
Efficiency	74
Angular acceptance and angular resolution	76
IV Results	77
IV.1 Elastic scattering of ^{26}Ne	78
IV.1.1 Optical potential	78
IV.1.2 Extraction of experimental angular distributions	79
Method	79
Results	81
IV.2 Inelastic scattering below the neutron emission threshold	83
IV.2.1 DWBA	83
IV.2.2 $B(E2)$ calculation	85
^{26}Ne gamma decay analysis	85
$B(E2)$ extraction using angular distributions	87
$B(E2)$ extraction using the equivalent photon method	89
Theoretical considerations	89
Results	90
Discussion on $B(E2)$	92
IV.3 ^{26}Ne excitation energy above S_n	96
IV.3.1 The method	96
Illustration by a simplified case	97
Simulation	98
IV.3.2 Level scheme of daughter nucleus ^{25}Ne via γ -decay	100
Analysis by means of simulations, contributions	101
Confirmation of the 2 MeV excited state	103
Analysis of events with multiplicity equal to two	104
Conclusion on the ^{25}Ne level scheme	105

Table of Contents

IV.3.3	^{26}Ne excitation energy spectrum	106
	Extraction	107
	Excitation energy spectra, $^{25}\text{Ne}+n$ channel	108
	Extraction of the Coulomb excitation cross section	112
	Method 1: Integrated cross sections	112
	Method 2: Angular distribution	113
IV.3.4	Discussion on the $B(E1)$ value	116
	Comparison with mean-field calculations	116
	Comparison with other models	119
	Decay of pygmy resonances in ^{26}Ne	120
IV.3.5	Estimation of the direct break-up	121
	Results	124
	Summary & Conclusion	125
	A Extraction of ^{26}Ne excitation energy distribution, simulation test case	128
	B Description of the simulation code	133
	B.1 Description of the simulation code	133
	B.2 Beam simulation	133
	B.3 Inelastic scattering and decay	135
	B.3.1 Inelastic scattering	135
	B.3.2 Decay	135
	B.3.3 Illustration	135
	B.4 DALI simulation	136
	B.5 Silicon hodoscope simulation	138
	B.6 Neutron wall simulation	139
	C Relativistic Kinematics	140
	C.1 Notations, Basic relations	140
	C.1.1 Notations	140
	C.1.2 Basic (one body) relations	141

C.2	Two-body reaction: Center of Mass (CM) frame	141
C.2.1	Notations	142
C.2.2	Relations	142
C.3	Two-body decay	142
C.3.1	Doppler Effect	143
C.4	Three-body breakup	144
	Résumé	155
	Abstract	155

List of Tables

II.1	Data set summary	41
III.1	PPAC position offset	48
III.2	γ -ray source energies & exp. deviation	51
III.3	Neon isotopes Doppler corrected γ -rays	58
III.4	Energy loss calibration in silicons	60
III.5	Protons and tritium TOF	69
IV.1	Optical parameters	81
IV.2	^{26}Ne 2^+ $B(E2)$ variations	93
IV.3	^{25}Ne γ -rays contributions	103
IV.4	B(E1) values	117
IV.5	Branching ratios	120
A.1	Branching ratio from the ^{26}Ne excited state to difference state of the ^{25}Ne for the lead and the aluminum target. . .	130

List of Figures

I.1	Illustration of GR modes	3
I.2	GR and major shells	5
I.3	Illustration of GR damping	6
I.4.a	Energy of neon's pygmy with two fluids framework	10
I.4.b	S_{TRK} of neon's pygmy with two fluids framework	10
I.5	Pygmy sum rule in neutron rich oxygens	11
I.6.a	Theor. IV Dipole strength in Neons, $A = 20 \rightarrow 28$	13
I.6.b	Compared Theor. IV Dipole strength, ^{26}Ne and ^{20}Ne	13
I.7.a	Electromagnetic field of a relativistic nucleus	14
I.7.b	Consequent plane waves and photons	14
I.8	Coulomb excitation cross sections, selectivity	16
I.9	$L = 1$ vs $L = 2$ or 3 angular distribution	17
I.10	Particles emission threshold in ^{26}Ne	18
I.11	Coulomb excitation	19
II.1	RIKEN Accelerator Research Facility	23
II.2	RIKEN Projectile fragment Separator	24
II.3	Experimental setup	27
II.4	Experimental setup, scaled view	28
II.5	PPAC drawing	29
II.6	Silicon setup drawing	30

List of Figures

II.7.a	Gamma detector array drawing: DALI(I)	32
II.7.b	Gamma detector array drawing: DALI(II)	32
II.8	View of the whole DALI	33
II.9	Photograph of DALI(II)	34
II.10	View of the neutron plastics array	35
II.11	Photograph of the neutron wall	36
II.12	Circuit diagram for BEAM detectors.	37
II.13	Circuit diagram for silicon hodoscope.	37
II.14	Circuit diagram for DALI.	38
II.15	Circuit diagram for neutron wall.	38
II.16	Circuit diagram for total trigger.	39
II.17	DAQ configuration	40
III.1.a	Beam PID: F2(dE) vs TOF	43
III.1.b	Beam PID: TOF	43
III.2.a	Beam profile at PPAC A	45
III.2.b	Beam profile at PPAC B	45
III.2.c	Beam angle	45
III.2.d	Beam profile at SSD	45
III.3	Timing sum in PPACs	46
III.4.a	Alignment: $X_{PPAC@SSD} - X_{SSD}$	48
III.4.b	Alignment: $X_{PPAC@SSD}$ vs X_{SSD}	48
III.5	γ -ray sources calibration	49
III.6.a	DALI ^{60}C standard source simulation	52
III.6.b	DALI efficiency	52
III.7.a	DALI acceptance for ^{22}Na standard source	53
III.7.b	DALI acceptance: 2018 keV γ , $\beta = 0.32$ moving emitter	53
III.8	Doppler correction example	54
III.9	Doppler correction test	55
III.10	DALI time windows, background rejection	56
III.11.a	NaI intrinsic energy resolution	58
III.11.b	DALI energy resolution	58

III.12.a	E- ΔE identification in silicons	61
III.12.b	Neon mass number identification	61
III.13.a	Angular acceptance of silicon hodoscope	62
III.13.b	Angular acceptance of silicon for ^{26}Ne beam	62
III.14.a	Muons deposited energy	65
III.14.b	Light attenuation in plastics	65
III.15.a	Plastic amplitude/position dependence before correction	66
III.15.b	Plastic amplitude/position dependence after correction	66
III.16.a	$\langle \text{TOF} \rangle_{\text{F0} \rightarrow \text{F2}}$ and $\langle \text{TOF} \rangle_{\text{F2} \rightarrow \text{Target}}$ definition	67
III.16.b	$\langle \text{TOF} \rangle_{\text{F0} \rightarrow \text{F2}}$ vs $\langle \text{TOF} \rangle_{\text{F2} \rightarrow \text{Target}}$	67
III.17.a	TOF spectrum in plastic using brass target	68
III.17.b	TOF vs amplitude in plastic using brass target	68
III.18.a	Explanation of the walk effect	70
III.18.b	Slew effect in plastic	70
III.19	Slew propagation method scheme	71
III.20.a	Muon tracking	73
III.20.b	Muon position shift	73
III.21	Use of plastic vetoes for position calibration	74
III.22.a	Neutron efficiency vs amplitude threshold	75
III.22.b	Neutron efficiency vs neutron incident energy	75
III.23.a	Neutron wall angular acceptance	76
III.23.b	Neutron wall angular resolution	76
IV.1.a	Elastic $\frac{d\sigma}{d\Omega} / \frac{d\sigma}{d\Omega_{\text{Ruth}}}$, lead target	82
IV.1.b	Elastic $\frac{d\sigma}{d\Omega} / \frac{d\sigma}{d\Omega_{\text{Ruth}}}$, aluminum target	82
IV.2	Adopted levels and gammas in ^{26}Ne	85
IV.3	^{26}Ne Doppler corrected gamma energy distribution	86
IV.4	Gamma analysis, multiplicity 2, ^{25}Ne	87
IV.5.a	Exp. ^{26}Ne γ distribution w/ fitted background, $^{\text{nat}}\text{Pb}$ target	88
IV.5.b	Angular distribution, first 2^+ of ^{26}Ne , $^{\text{nat}}\text{Pb}$ target	88
IV.6.a	Exp. ^{26}Ne γ distribution w/ fitted background, $^{\text{nat}}\text{Al}$ target	89
IV.6.b	Angular distribution, first 2^+ of ^{26}Ne , $^{\text{nat}}\text{Al}$ target	89

List of Figures

IV.7	^{26}Ne 218 keV gamma angular distribution	92
IV.8	$B(E2)$ value, function of the extraction method	93
IV.9.a	$E_{2_1^+}$ for even neon isotope	95
IV.9.b	$B(E2; 0^+ \rightarrow 2^+)$ for even neon isotope	95
IV.10	Simulated simplified ^{26}Ne decay	97
IV.11.a	Simulated E^* inclusive spectrum	99
IV.11.b	Simulated E^* spectrum in coincidence w/ decay γ -ray	99
IV.12	^{25}Ne level scheme	101
IV.13	^{25}Ne Gamma energy distribution	102
IV.14.a	Gamma energy distribution vs neon mass number	104
IV.14.b	PID in silicon detectors	104
IV.15	Gamma analysis, multiplicity 2, ^{25}Ne	105
IV.16	Scheme of decay from ^{26}Ne	106
IV.17	^{26}Ne relative energy spectrum	109
IV.18.a	^{26}Ne E^* for lead target and background	110
IV.18.b	^{26}Ne E^* for lead target, background subtracted	110
IV.18.c	^{26}Ne E^* for aluminum target and background	110
IV.18.d	^{26}Ne E^* for aluminum target background subtracted	110
IV.19.a	Example of angular distribution, Lead	111
IV.19.b	Example of angular distribution, Aluminum	111
IV.20.a	$E^* = 9\text{MeV}$ state angular distribution, lead	114
IV.20.b	$E^* = 9\text{MeV}$ state angular distribution, aluminum	114
IV.21.a	Angular distribution, $L = 1$ and $L = 2$ fit	116
IV.21.b	Values retained	116
IV.22.a	$dB(e1)/dE^*$, QRPA, Cao <i>et al.</i>	117
IV.22.b	$dB(e1)/dE^*$, QRPA, Khan <i>et al.</i>	117
IV.23.a	$dB(e1)/dE^*$, QRPA, Péru <i>et al.</i>	118
IV.23.b	$dB(e1)/dE^*$, RQRPA, Ring <i>et al.</i>	118
IV.24	Neutron angular distribution for Pb	121
IV.25.a	^{26}Ne trajectory on lead	123
IV.25.b	^{26}Ne trajectory on aluminum	123

A.1	Scheme of decay from ^{26}Ne	129
A.2	^{26}Ne relative energy spectrum	131
A.3	^{26}Ne relative energy spectrum	132
B.1	Experimental setup	134
B.2	Arbitrary ECIS 97 $^{26}\text{Ne}+^{208}\text{Pb}$ angular distribution (plain line) compared with the reconstruction just after break-up into $^{25}\text{Ne}+n$ (filled circles) as given by the simulation. The dotted line is obtain after simulation of the detection and illustrates the effect if the latter.	136
B.3.a	DALI ^{60}C standard source simulation	137
B.3.b	DALI efficiency	137
B.4	Test on Geant 3 accuracy reproducing energy loss in silicon. Here the black contour is obtained from ^{25}Ne from ^{26}Ne break-up. It is superimposed to experimental results	138
C.1	Illustration of the notations	141
C.2	Two body decay	143
C.3	Doppler Effect	143
C.4	Three body decay	144

Introduction

Giant Resonances are general properties of all but very light nuclei. Well understood in stable nuclei, the development of radioactive beams over the past 20 years enable us to investigate their behaviour for nuclei far from the valley of stability. We present here experimental work which aims to highlight the presence of a low energy dipole strength in the neutron rich nucleus ^{26}Ne .

This dissertation is organized as follow: in a first chapter we will introduce notions concerning Giant Resonances and more specifically the Dipole modes. We will emphasize on the evolution of their properties in neutron rich nuclei. Then we will describe the experimental tools: the Coulomb excitation, the Distorted Wave Born Approximation and the invariant mass method. The second chapter is dedicated to the description of the experimental setup composed of beam trackers, a γ -ray detector, a charged fragment hodoscope and a neutron detection wall. In the third part, we will analyze the data obtained with these four detectors. Finally the first part of the chapter four will present results on excited states below the one neutron emission threshold including the extraction of the $B(E2; 0^+ \rightarrow 2^+)$ value. In a second part, using the invariant mass method, the excited states between the one and the two neutron threshold will be analyzed and the results compared to predictions of mean field calculations.

Chapter I

Giant resonances: from stable to unstable nuclei

I.1 Overview on Giant Resonances

Giant Resonances (GR) are high frequency collective excitation modes of the nucleus, which involve a large number of nucleons. The collectivity means that their characteristics depend on the bulk structure of the nucleus and they are a general property of nuclei present in all but very lightest species. Their parameters vary smoothly with the mass number A and they exhaust a large part of the appropriate sum rule. GR were first observed in 1937 by means of photo-absorption onto ^{63}Cu nucleus [Bothe 37]. But one had to wait until 1947 before a systematic study was performed by Baldwin and Klaiber [Baldwin 47] with the development of new accelerators. In stable nuclei, Giant Resonances are characterized by an excitation energy higher than the particle emission threshold (10–20 MeV) and a broad width Γ of 2.5–6 MeV. For a comprehensive and up-to-date discussion of GR the reader is referred to [Van Der Woude 01].

I.1.1 Macroscopic picture

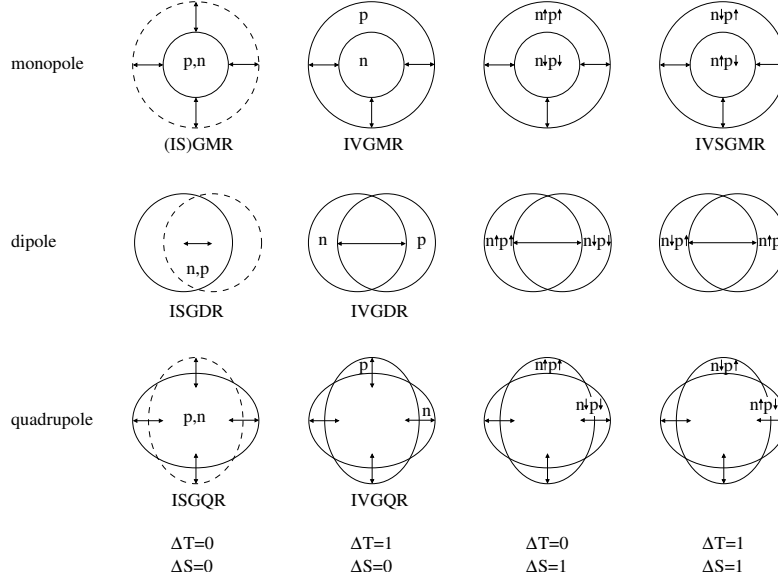


Figure I.1: Schematic representation of various collective modes within the liquid-drop model. From [Zegers 99].

Giant Resonances are collective phenomenon and can be described as small-amplitude oscillations of a liquid drop about its equilibrium shape. Considering that the nuclear fluids consist of protons and neutrons with spin up or down this leads to rich resonance phenomenology that can be classified according to three quantum numbers: their angular momentum L , isospin T and spin S as illustrated in Fig. I.1:

According to the isospin T the modes are classified as:

Isoscalar ($\Delta T = 0$): in which neutrons oscillate in phase with protons.

Isovector ($\Delta T = 1$): in which neutrons and protons oscillate in opposite phase.

And according to the spin S the modes are:

Electric ($\Delta S = 0$): in which nucleons vibrate following a multipole pattern given by L .

Magnetic ($\Delta S = 1$): in which nucleons with spin \uparrow vibrate against nucleons with spin \downarrow , following a multipole pattern given by L .

The three lowest angular momentum modes are:

the Giant Monopole Resonance (GMR), $\Delta L = 0$, or “breathing mode”. It is a density oscillation consisting of cyclic phases of compression and expansion.

the Giant Dipole Resonance (GDR), $\Delta L = 1$, is a density/shape oscillation which is often pictured as vibrational displacement of two fluids which nature depends upon the two other quantum numbers.

the Giant Quadrupole Resonance (GQR), $\Delta L = 2$, is a surface oscillation where the two fluids considered are distorted in two orthogonal directions.

If the macroscopic model can explain most of the macroscopic features of the Giant Resonance it does not describe all the width properties and how the nucleons organize themselves, for which a microscopic picture is necessary.

I.1.2 Microscopic picture

The microscopic models are often based on the mean-field concept which consists in describing the n-body problem of the interactions between all the nucleons as a sum of interactions of one nucleon inside a potential created by all the other nucleons, plus a small residual interaction. One of the most used methods to calculate the best non correlated ground state is called Hartree-Fock (HF), method based on variational principals. From here, a very commonly-used approximation called Random Phase Approximation (RPA) helps to include the ground state correlation and the pairing. The RPA ground state $|RPA\rangle$ is hence a superposition of particle-hole states (1p-1h). In this framework, and by taking into account the residual interaction, the GRs are described as a coherent superposition of many particle-hole excitations, resulting from the action of an operator $\mathcal{O}_{\lambda,\sigma,\tau}^\dagger$ on $|RPA\rangle$:

$$|GR\rangle = \mathcal{O}_{\lambda,\sigma,\tau}^\dagger |RPA\rangle \quad \text{with} \quad \mathcal{O}_{\lambda,\sigma,\tau} |RPA\rangle = |0\rangle \quad (\text{I.1})$$

where λ, σ, τ are multipolarity*, spin and isospin structure.

*Microscopic equivalents of L, T and S in Sec. I.1.1

I.1 Overview on Giant Resonances

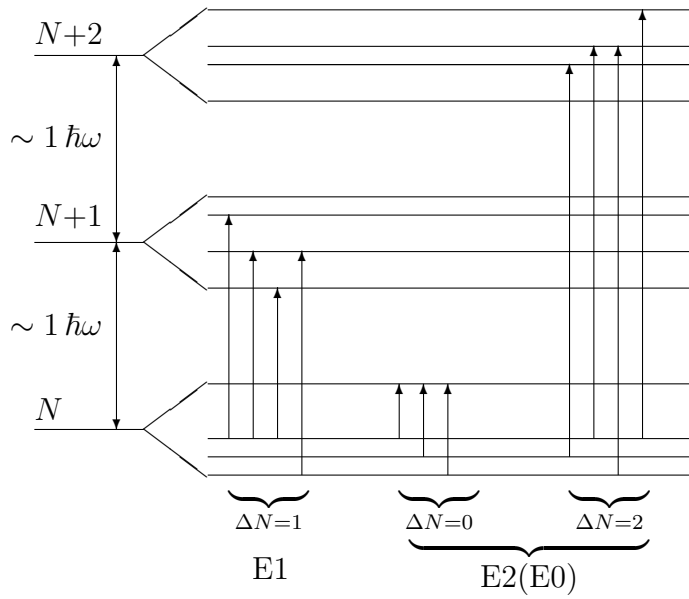


Figure I.2: Schematic picture of E1 and E2 (E0) single particle transitions between shell model states.

Qualitative aspects can be understood using a schematic shell model picture. In such an independent particle model, the energy associated to one vibration is a multiple of the difference between two shells $N, N+1, \dots$ *i.e.* $\hbar\omega = \Delta N \times 41 A^{-1/3}$ MeV. Due to momentum and parity conservation, a $\sigma = 0, \tau = 0$ excitation will correspond to a transition with $\Delta N \leq \lambda$ and with $(-1)^{\Delta N} = (-1)^\lambda$ for parity conservation, as illustrated in Fig. I.2. Now in a correlated approach since the residual interaction is attractive for isoscalar and repulsive for isovector excitations, isoscalar resonances will be located below and the isovector above the unperturbed $\hbar\omega$ energies.

These simple considerations also show on the difficulties of studying Giant Resonances experimentally: the excitation energy of different types of GR can be located around the same value. The overlap is increased by the large GR width. In order to disentangle them, specific selective probes should be used.

I.1.3 Damping of Giant Resonances

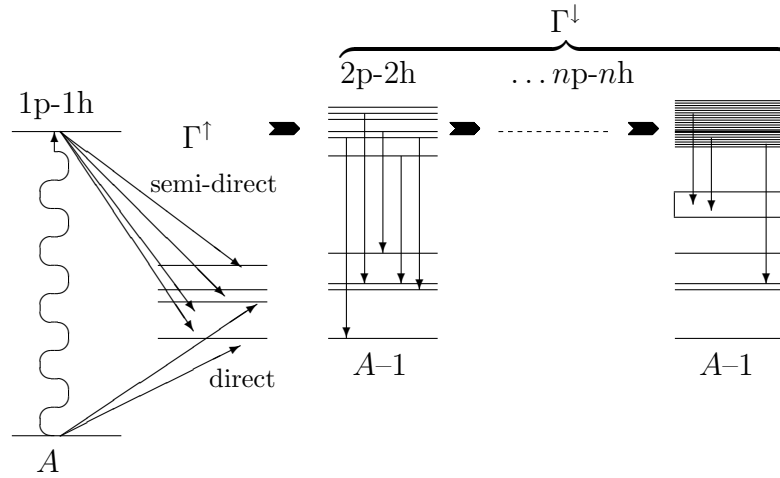


Figure I.3: Schematic picture of the width of the collective (1p-1h) state into a direct component $\Gamma \uparrow$ and a spreading component $\Gamma \downarrow$. Note that in principle the intermediate states can also decay as indicated by $\Gamma^{\uparrow\downarrow}$. From [Van Der Woude 01]

Damping and decay of Giant Resonances are strongly connected to their width. The width can be written:

$$\Gamma = \Delta\Gamma + \Gamma^{\uparrow} + \Gamma^{\downarrow} \quad (\text{I.2})$$

where :

$\Delta\Gamma$ is the Landau damping. It arises from the fact that the collective (1p-1h) strength is spread over many states. This damping is found especially in light nuclei.

Γ^{\uparrow} is the escape width and it comes from the coupling of the collective (1p-1h) ‘doorway’ state with the continuum. This leads to a (semi)-direct decay of a nucleus ${}^A\text{X}$ to a nucleus ${}^{A-1}\text{X}$. It is dominant light nucleus.

Γ^{\downarrow} is the spreading width. It is dominant in heavy nuclei and correspond to coupling to more complex states such as (2p-2h), which again couples to (3p-3h), etc. . . to (np-nh) until a statistical equilibrium is reached. The system can decay at any intermediate state and contribute to the pre-equilibrium

I.1 Overview on Giant Resonances

with $\Gamma^{\uparrow\downarrow}$. In case a fully equilibrated system is reached it decays by evaporation of particles and contribute to the width *via* the statistical width $\Gamma^{\uparrow\downarrow}$.

The study of the direct decay of giant states constitute the strongest test for the models predicting the wave function of the modes.

I.1.4 Collectivity, sum rule

In the analysis of GR spectra, it is very useful to make use of sum rules which are derived from the transition operator previously described. We can define the n^{th} moment of the transition probability distribution by:

$$m_n = \sum_v (E_v - E_0)^n \left| \langle 0 | \mathcal{O}_{\lambda,\sigma,\tau} | \nu \rangle \right|^2 \quad (\text{I.3})$$

where $|\nu\rangle$ is a state which composes the Giant Resonance state: $|GR\rangle = \sum_\nu |\nu\rangle$. Note that Eq. I.3 can be seen as the complete sum of “partial” sum rules $(E_v - E_0)^n \left| \langle 0 | \mathcal{O}^{\lambda,\sigma,\tau} | \nu \rangle \right|^2$ for a given $|\nu\rangle$ state. In most of the cases, the ratio between one of this “partial” sum rule and the total one gives information on the collectivity of the $|\nu\rangle$ state.

The moment m_1 , called Energy Weighted Sum Rule (EWSR), is of a particular importance for Giant Resonances. It can be evaluated independently of the models and depends only on the ground state properties of the nucleus. It is also expressed by:

$$m_1 = \frac{1}{2} \langle 0 | [\mathcal{O}^{\lambda,\sigma,\tau}, [H, \mathcal{O}^{\lambda,\sigma,\tau}]] | 0 \rangle \quad (\text{I.4})$$

where H is the Hamiltonian of the system.

I.1.5 Giant Dipole Resonances

The Giant Dipole Resonance (GDR) was the first mode of GRs to be discovered owing to the use of photo-nuclear reactions[†] as experimental tool. This

[†]*i.e.* reactions in which a nucleus is bombarded with energetic γ -rays

reaction is very selective. It strongly disadvantages the high multi-polarities and almost only dipole excitations are induced.

The total cross sections for GDR excitations are of the order of hundreds of millibars and its distribution in heavy nuclei is well reproduced by a Lorentzian distribution:

$$\sigma_{\gamma}(E) = \frac{\sigma_{\max}}{1 + [(E^2 - E_{\text{GDR}}^2)/E\Gamma]^2} \quad (\text{I.5})$$

where E_{GDR} is the resonance energy, σ_{\max} the maximum cross section and Γ the width of the distribution. These parameters are smooth function of the nucleus mass number A .

The Giant Dipole Resonance was first theoretically explained in terms of collective vibration by Goldhaber and Teller in 1948 [Goldhaber 48] and by Steinwedel and Jensen in 1950 [Steinwedel 50]. In both cases the GDR is described as an out-of-phase oscillation of protons against neutrons which separates the center of mass from the center of charge, producing a dipole moment. The first authors described the phenomenon in terms of incompressible and rigid fluids. The whole nucleus is then deformed and its response is proportional to a surface energy. For the second authors the GDR is a compressional mode with an out-of-phase density oscillation of the neutron against the proton fluid, with in this case a response proportional to the volume energy term. They predicted a dependence in excitation energy in $A^{-1/6}$ and $A^{-1/3}$ respectively but in reality, the vibration is both a volume and a surface vibration and the excitation energy dependence with A is well reproduced in stable nuclei by:

$$E_{\text{GDR}}^*(A) = 31.2 A^{-1/3} + 20.6 A^{-1/6} \text{ MeV} \quad (\text{I.6})$$

The EWSR, defined in Sec. I.1.4, can here be expressed using only the atomic Z and mass number A of the nucleus of interest. The so called Thomas-Reiche-Kuhn (TRK) sum-rule is directly related to the GDR photo-nuclear reaction cross section:

$$\int_0^{+\infty} \sigma_{\gamma} dE = \frac{2\pi^2 e^2 \hbar N Z}{mc} \frac{1}{A} \approx 60 \frac{Z(A-Z)}{A} \text{ mb MeV} \quad (\text{I.7})$$

I.2 Collective excitations in neutron rich nuclei

A current topic of interest in nuclear physics is the evolution of the nuclear structure for nuclei far from the valley of stability. When going towards the neutron drip-line the neutron density distribution become more diffuse at the surface. This results in neutron halos in light nuclei and neutron skins in heavy nuclei. In the past decade, several theoretical studies performed in the framework of the liquid drop model [Suzuki 90, Van Isacker 92] predicted a redistribution of the multipole strengths, essentially at lower energy compared to the stable nuclei. In general, all mean-field calculations predict these low-lying structures, often call *pygmy resonances*, which carry a small fraction of the full strength. Experimentally few results are available and almost essentially for the dipole resonances in light nuclei like ^{11}Li . Among other impacts, the measurement of the properties of these modes will help tuning the forces or the field implemented in the calculations [Reinhard 99].

In the following we will describe more in details the case of the dipole resonance within a simple two-fluids model. Then we will present recent experimental results on the oxygen and the tin isotopic chains. Finally, we will introduce mean-field calculations describing the dipole strength in our nuclei of interest: the neutron-rich neon isotopes.

I.2.1 Dipole excitation and sum rule evolution

In this section we will introduce simple concepts for the pygmy dipole resonance within the liquid drop model.

The *pygmy resonance* can be tentatively explained by the presence of loosely bound neutrons which can create a halo or a neutron skin. A very simple picture of this phenomenon is given within the liquid drop model [Suzuki 01] if we suppose a deeply bound core surrounded by neutrons. A plane-wave impinging of this object will displace the charged core with respect to its skin. This will separate the center of mass from the center of

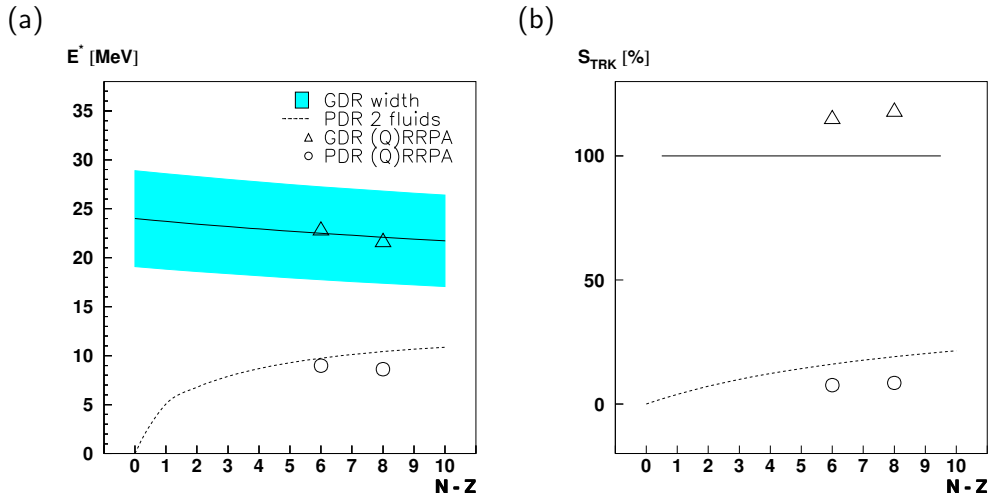


Figure I.4: (a) Energy of neon's isotopes pygmy dipole resonance (PDR) within two (dashed line) fluids framework. For comparison the shaded area represent the GDR region. Results from (Q)RRPA calculation [Cao 05b] are also shown (see sections above). (b) Ratio of Thomas-Reiche-Kuhn (TRK) sum rule exhausted by the GDR and the PDR. Same legend as figure (a).

charge and will produce a dipole moment. Then the oscillation occurs thanks to the restoring strong forces, like in the Giant Dipole Resonance case of Sec. I.1.1. The difference here is the energy needed, smaller, since there is no full separation of proton and neutron distributions. We show in Fig. I.4 the results of calculation using this two fluids model framework, for the neon isotopes. We suppose here that the core is ^{20}Ne to which we add 1 to 10 neutrons. Following [Suzuki 01] the energy at which the pygmy resonance occur E_{PDR} is a fraction of the GDR average energy E_{GDR} :

$$E_{\text{PDR}} = \sqrt{\frac{Z(N - N_c)}{N(Z + N_c)}} E_{\text{GDR}} \quad (\text{I.8})$$

where N_c is the number of neutron in the core, Z and N the number of protons and neutrons of the nucleus of interest. The same considerations relate the total classical sum rule S_{tot} and the sum rule exhausted by the

I.2 Collective excitations in neutron rich nuclei

pygmy S_{PDR} :

$$S_{\text{PDR}} = 0.857 \frac{Z(N - N_c)}{N(Z + N_c)} S_{\text{tot}} \quad (\text{I.9})$$

If this simple model does not reproduce accurately nor the energy centroid neither the fraction of sum rule exhausted, partly because of the possible non-collective nature of the pygmy as will be discussed further, it gives an good idea of the trends with the neutron richness. As one can see on Fig. I.4, both the energy and the strength of the pygmy resonance is increasing with the number of neutrons.

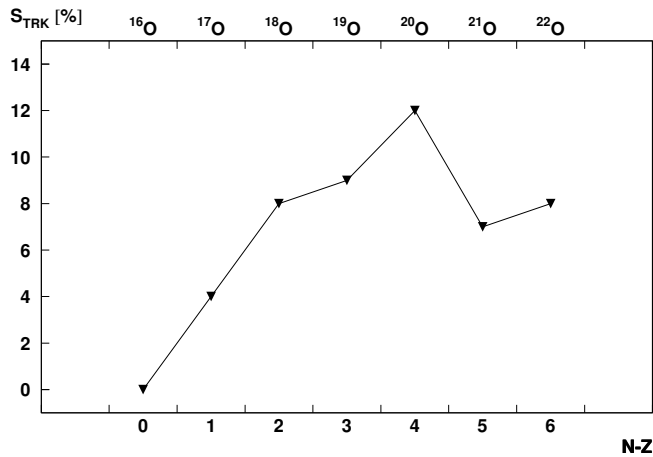


Figure I.5: Experimental evolution with the mass number of the sum rule of the low-lying E1 resonance in oxygen isotopic chain [Leistenschneider 01].

Up to now few experiments were performed in that direction, especially due to the fact that it involves (very) exotic nuclei. In light nuclei like ^{11}Be a large low lying dipole strength has been measured above the neutron threshold, which can be related to the direct break-up mechanism [Nakamura 97, Palit 03]. In the oxygen chain, if for the stable ^{16}O the photo-absorption cross section shows mainly the expected major peak at 23-25 MeV excitation energy, in the ^{18}O , structures already appear between 10-20 MeV [McLean 91]. The first systematic study in that direction, using exotic beam,

was performed in GSI by the LAND collaboration [Leistenschneider 01]. Using the Coulomb excitation of secondary oxygen beams in reverse kinematics at $\sim 600 \text{ MeV}/n$, they measured the dipole strength exhausted by the pygmy resonance in $^{17-22}\text{O}$. Their experimental results are displayed Fig. I.5 and they found that the pygmy strength increases with the oxygen mass number and exhaust up to 12% of the TRK sum rule in ^{20}O . But they measured a clear drop after ^{20}O which is against the trend predicted by the simple liquid drop model presented previously. This means that our naive model of ^{16}O surrounded by a neutron skin is no longer applicable for these isotopes and these observations challenge the collective picture of the excitations. The same group recently performed the same type of experiments on neutron rich tin isotopes [Adrich 05a, Adrich 05b]. Again if they measured a low-lying dipole strength, its collective nature is still under debate.

I.2.2 Prediction of low lying dipole strength in ^{26}Ne

As previously mentioned, mean field calculations are one of the main theoretical tools which can explain and predict excitation energies and their strength. We present in Fig. I.6 (a) Quasiparticle Relativistic Random Phase Approximation (QRRPA)[‡] calculation performed by Cao and Ma [Cao 05a] for the iso-vector dipole strength in even-even neon isotopes of mass $A = 20 \rightarrow 28$. If the main peak of the GDR follows the systematics of Eq. I.6 (gray line), a structure clearly appears around 10 MeV excitation energy from ^{24}Ne up. We then focus on ^{26}Ne , which we compare to ^{20}Ne in Fig. I.6 (b) (up) and (down) respectively. We superimpose to Relativistic Random Phase Approximation the QRRPA calculations for ^{26}Ne and to the experimental results for ^{20}Ne . On this figure it is clear again that both ^{20}Ne and ^{26}Ne shows a maximum of strength around the expected (Eq. I.6 gives $E^* = 22\text{--}24 \text{ MeV}$) giant dipole resonance excitation energy. However, if all the strength is concentrated around this value in ^{20}Ne , in ^{26}Ne a fragmentation at low en-

[‡]Note that some authors call this last method, equivalently, Relativistic Quasiparticle Random Phase Approximation (RQRPA)

I.3 Experimental considerations

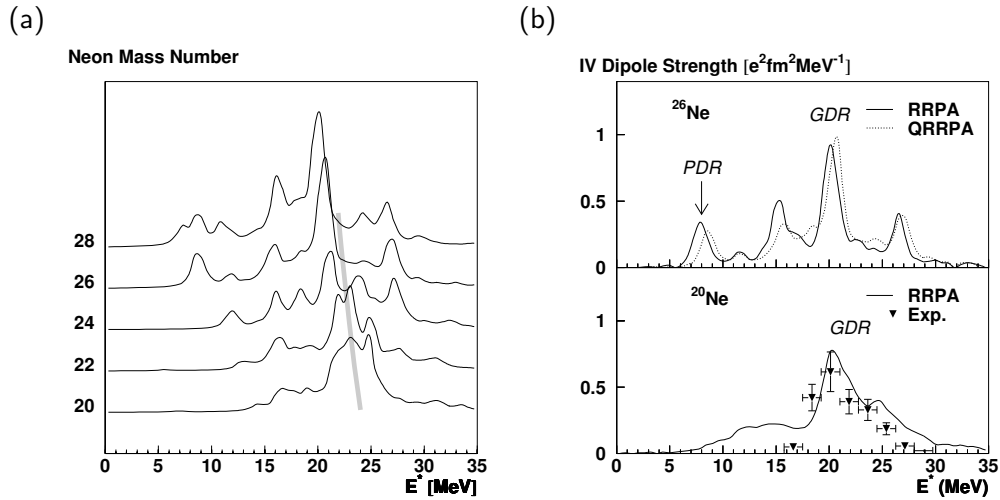


Figure I.6: (a) Comparison for a QRRPA calculation of the IVGDR strength for $A = 20 \rightarrow 28$ neon isotopes. The gray line is the prediction of Eq. I.6. (b) Isovector dipole strength functions in: the neutron rich ^{26}Ne (up) and the stable ^{20}Ne (down). The QRRPA response with pairing (dashed line) are compared to RRPA calculation without pairing (solid line) for the ^{26}Ne case. The experimental result obtained from photo nuclear reactions [Varlamov 00] is displayed as triangles for ^{20}Ne .

ergy clearly appears. From now we will focus on the lowest peak centered around $E^* = 8.34$ MeV, which the calculation predicts to exhaust 4.9% of the Thomas-Reiche-Kuhn (TRK) energy weighted sum-rule (Eq. I.7). We compared on Fig. I.4 the values predicted by this (Q)RRPA calculation with the values predicted by the two-fluids model. Interestingly, we observe that the trends for excitation energy and sum rule are comparable.

I.3 Experimental considerations

Up to the early 80's, Giant Resonances have been studied mainly using light probes such as protons, deuterium or alpha particles on stable nuclei. The development of intermediate-energy heavy-ion accelerators like GANIL and RIKEN opened new perspectives in this field. The first heavy ion studies

showed [Barrette 88, Suomijärvi 89] a strong enhancement of the iso-vector giant dipole resonance (IVGDR) cross section. In the early nineties, Radioactive Ion Beams became available and the study of GR in exotic nuclei feasible, but progress has been slow due to low beam intensities and technical difficulties.

In this case the beam is the nucleus of interest and is probed by the target, which is called inverse kinematics. This method was first used in GSI for the study of Giant Dipole Resonances and multi-phonon excitation [Aumann 98]. Since GRs are located above the particle emission threshold, the projectile-like nucleus will break-up and all the products (fragments, particles, gammas) need to be collected to perform a complete kinematical reconstruction of the excitation energy. Since the Coulomb excitation is the dominant mechanism involved for highly charged heavy ions, we will introduce in the next section its description *via* the so-called semi-classical virtual photon theory. At the RIKEN energies, angular distributions of the outgoing fragment can also be measured which will allow to disentangle the different multipolarities excited, as we will show in Sec. I.3.2. Finally, a study of the excited ^{26}Ne decay in Sec. I.3.3 will bring us to introduce the invariant mass method in Sec. I.3.4.

I.3.1 Virtual photon method

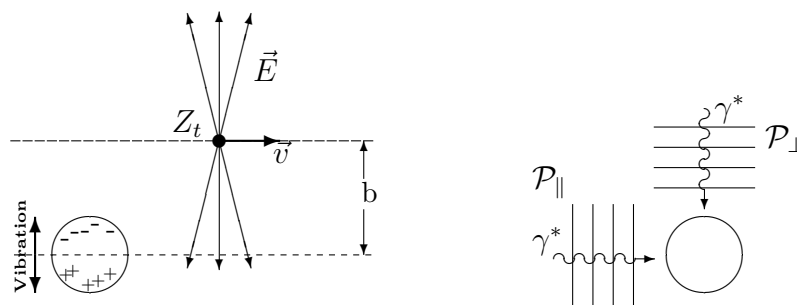


Figure I.7: (a) Schematic drawings of a relativist ion incident on a target. The electromagnetic field can induce excitation in the target nucleus. (b) It can be seen as the production of two pulses of plane waves. From [Bertulani 88].

I.3 Experimental considerations

Coulomb excitation is the excitation of a target nucleus by the electromagnetic field of the projectile and vice-versa. The simplest way to describe its reaction mechanism at relativistic energies is given by the so called virtual photon method. It was introduced by Fermi [Fermi 24] and independently developed by Weiszäcker [Weiszäcker 34] and Williams [Williams 34]. A complete description can be found in the Jackson textbook [Jackson 99]. For other details on the induced reaction, the reader is referred to the work of Winther and Alder [Winther 79] or Bertulani and Baur [Bertulani 88].

Let's consider a fixed target nucleus (A_p, Z_p) and neglect the recoil. The electromagnetic field created by a moving nucleus with the velocity $\vec{v} = \vec{\beta}c$ along a straight line has two components: one parallel to the direction of motion (noted \parallel) and one perpendicular \perp , given by:

$$E_{\parallel}(t) = -Z_p e \frac{\gamma vt}{[b^2 + (\gamma vt)^2]^{3/2}} \quad ; \quad B_{\parallel}(t) = 0 \quad (\text{I.10})$$

$$E_{\perp}(t) = Z_p e \frac{\gamma b}{[b^2 + (\gamma vt)^2]^{3/2}} \quad ; \quad B_{\perp}(t) = \beta E_{\perp}(t) \quad (\text{I.11})$$

where b is the impact parameter and $\gamma = 1/\sqrt{1-\beta^2}$. The field generated by the projectile looks contracted in the direction perpendicular to the motion. For $\gamma \gg 1$ and if we add a minor magnetic field $B_{\parallel}(t) = \beta E_{\parallel}(t)$ the two plane-polarized radiation \mathcal{P}_{\perp} and \mathcal{P}_{\parallel} falling on the target become two photons. They hence act during a very short time $\Delta t \approx b/\gamma c$.

By analogy we can calculate the incident energy $I(\omega, b)$ on the target and associate the field generated to a real photon spectrum. The probability for a certain electromagnetic process to occur hence reads:

$$P(b) = \int I(\omega, b) \sigma_{\gamma}(\hbar\omega) d\hbar\omega = \int N(\omega, b) \sigma_{\gamma}(\omega) \frac{d\omega}{\omega} \quad (\text{I.12})$$

where $\sigma_{\gamma}(\omega)$ is the *real* photo cross-section for the photon of energy $E_{\gamma} = \hbar\omega$. $N(\omega, b)$ can then be interpreted as the *equivalent photon number* per unit area that falls on the target. We can now express the Coulomb excitation cross section, taking into account the polarities ($\pi\lambda$) of the excitation and the fact

that it will be dominant only above a minimum impact parameter R at least greater than the sum of the two radii:

$$\sigma = \int_R^\infty 2\pi b P(b) db = \sum_{\pi\lambda} \int n_{\pi\lambda}(\omega) \sigma_\gamma^{(\pi\lambda)}(\omega) \frac{d\omega}{\omega} \quad (\text{I.13})$$

Here $n_{\pi\lambda}(\omega)$ is the equivalent photon number of energy $\hbar\omega$ and of multipolarity $(\pi\lambda)$ [§]. $\sigma_\gamma^{(\pi\lambda)}$ is the photo-nuclear absorption cross section for a *real* photon and for a given multipolarity $\pi\lambda$. It is directly proportional to the the reduced transition probability $B(\pi\lambda)$.

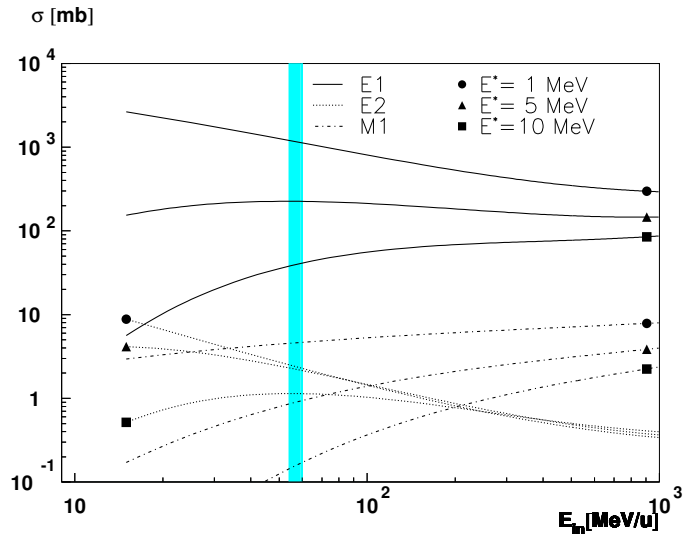


Figure I.8: ^{26}Ne Coulomb excitation cross section impinging on ^{208}Pb target for three different transitions, calculated using the equivalent photon method, function of the ^{26}Ne incident energy. We supposed $B(E1) = B(E2) = B(M1) = 1$ W.u. for three different excitation energies: $E^* = 1, 5$ and 10 MeV. The shaded region is the region accessed in our experiment.

Using the virtual photon method, we calculated the cross section for $E1, E2$ and $M1$ transitions with $B(E1) = B(E2) = B(M1) = 1$ W.u., for three different excitation energies: $E^* = 1, 5$ and 10 MeV of the ^{26}Ne incoming nucleus impinging on ^{208}Pb target. We suppose the minimum impact

[§]Its expression will be detailed for electric transitions in Eq. IV.23 and Eq. IV.23.

I.3 Experimental considerations

parameter to be equal to the sum of the two radii. The results are plotted in Fig. I.8 and show a clear dominance of E1 cross section at intermediate and high incident energy.

I.3.2 Distorted Wave Born Approximation

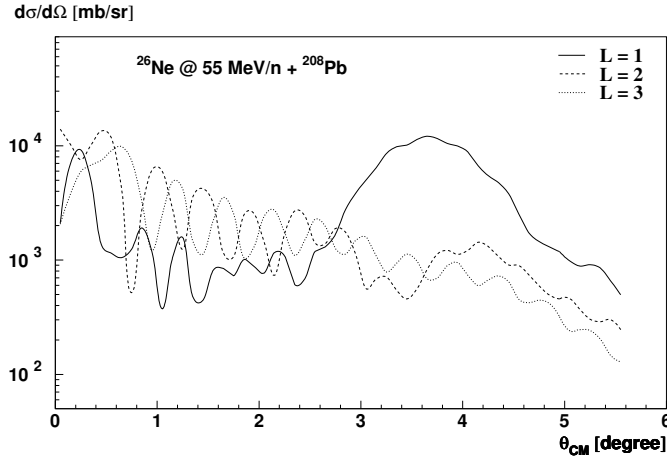


Figure I.9: Typical angular distribution obtain for ^{26}Ne impinging on ^{208}Pb at 55 MeV/n, using ECIS 97 code, for three different multipolarities.

In direct nuclear reactions, Distorted Wave Born Approximation (DWBA) or Coupled Channel (CC) calculations are extensively used. With heavy ions at intermediate energy their predictions show a very distinct angular distribution between transitions of multipolarity $L = 1$ and other multipolarities. Without detailing the procedure[‡] we present in Fig. I.9 the theoretical angular distribution in the center-of-mass system as given by ECIS 97 code [Raynal 97] for a ^{26}Ne at 55 MeV/n impinging on ^{208}Pb target. In a vibrational approach, we suppose here that 10% of the Thomas-Reiche-Kuhn sum rule is exhausted by a 9 MeV excited state. It can be seen on the figure that around the grazing angle ($\sim 3.5^\circ$) the shape of the $L = 1$ angular distribution strongly differs from the $L = 2$ or $L = 3$ ones. Note that however the

[‡]Which will be done in the following chapters

different $L \geq 2$ distributions present a rather similar shape. If we are able to measure the angular distributions with sufficient precision, they will provide a powerful tool to identify $L = 1$ strength among all possible excitations.

I.3.3 ^{26}Ne decays of resonances

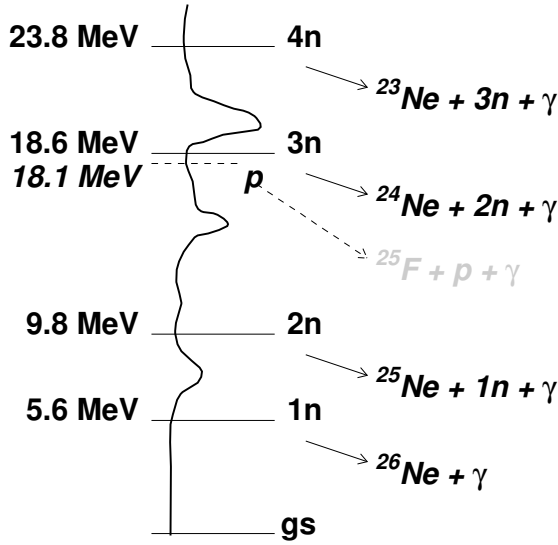


Figure I.10: Theoretical iso-vectorial strength function in ^{26}Ne (plain line), calculation from [Cao 05b], compared to neutron and proton emission thresholds, plotted with their subsequent decays. The predicted pygmy resonance at $E^* = 8.34$ MeV is located between the one and the two neutrons threshold.

^{26}Ne is a neutron rich nuclei. By consequence, the first neutron emission threshold is located at rather low energy ($S_n = 5.6$ MeV) compared to the stable isotopes, and one should expect the high excitation energy states composing the giant resonances to decay essentially by neutron evaporation rather than by photon emission. This is experimentally demonstrated in the same experimental condition of ours for example for ^{20}O in [Triggstad 01] where almost no γ -rays are observed decaying from excited states located above the neutron emission threshold. We then look at the particle emission thresholds in ^{26}Ne , plotted in Fig. I.10. We compare them with the theoretical iso-vector strength function predicted by Cao and Ma [Cao 05b] and we can see that the pygmy resonance of interest at around 8 MeV excitation energy is located between the one neutron emission threshold S_n and the two neutron emission threshold S_{2n} . Hence in order to investigate this region, we

I.3 Experimental considerations

must look at the $^{26}\text{Ne}^* \rightarrow ^{25}\text{Ne}^* + n$ decay channel and perform a complete kinematics experiment.

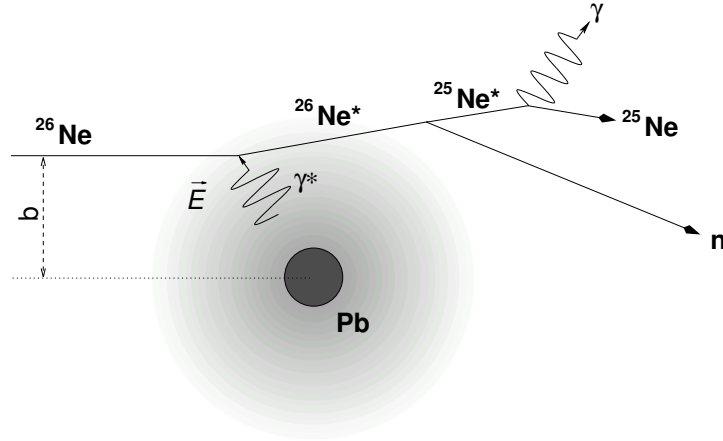


Figure I.11: Schematic drawing for Coulomb excitation followed by break-up. The projectile enters the strong electric field gradient produced by a highly charged nucleus. The reaction is illustrated by the main case studied here: the Coulomb excitation of ^{26}Ne and its subsequent scattering, followed by decay by neutron emission. ^{25}Ne is then here assumed to be produced in an excited state which decays by emission of gamma ray.

An illustration of the reaction is presented in Fig. I.11: The ^{26}Ne impinges on a highly charged target (here lead), which produces Coulomb excitation of the projectile[‡]. The incoming nucleus is thus scattered and decays by emitting a neutron. The remaining ^{25}Ne maybe left in an excited state which decays by gamma-ray emission. The invariant mass method, whose characteristic features will be developed in Sec. I.3.4, applied to the decay channel $^{26}\text{Ne}^* \rightarrow ^{25}\text{Ne}^* + n \rightarrow ^{25}\text{Ne} + \gamma + n$ forces our setup to need a neutron, a charged fragment and a gamma-rays detector.

[‡]It is modelized here by the absorption of a virtual photon γ^* , explained in the Sec. I.3.1.

I.3.4 Invariant mass method

The invariant mass method is a powerful tool for measuring excitation energies of unbound states, especially when used in inverse kinematics. Mathematically speaking the invariant mass is defined as the squared norm of the momentum four-vector $\widehat{P} = (E, \vec{p})$, which is a Lorentz invariant. Choosing a system of units where $c = 1$ it is written:

$$M_{\text{inv}}^2 = \left| \widehat{P} \right|^2 = E^2 - \vec{p}^2 \quad (\text{I.14})$$

where E is the total energy and \vec{p} the total momentum. It corresponds to the total energy in the rest frame of the system of interest. Consequently, for a system composed of i subsystems of rest mass M_i , of energy E_i and momentum p_i :

$$M_{\text{inv}} = M_0 + E^* = \sqrt{\sum_i E_i^2 - \sum_i \vec{p}_i^2} \quad (\text{I.15})$$

When the system conserves its energy during the reaction, the invariant mass relates the energy before the reaction to the energy of the outgoing subsystems. The invariant mass method then overcomes the poor resolution that can be associated with a secondary beam, for which the momentum spread can be large.

In the following we will restrain our system to the break-up of an excited nucleus of rest mass M_0 in two outgoing fragments which can be also in excited states. We thus write:

$$M_0^* = \sqrt{(E_1 + E_2)^2 - (\vec{p}_1 + \vec{p}_2)^2} = E_{\text{rel}} + M_1^* + M_2^* \quad (\text{I.16})$$

where E_{rel} is the relative energy between the constituents. The excitation energy of the mother nucleus E^* is hence related to the relative energy E_{rel} by $E^* = E_{\text{rel}} + E_S$ where E_S represents the separation energy for the decay channel. In the case of excited nucleus decaying by neutron emission in the ground state of the daughter nucleus, E_S is simply equal to the neutron emission threshold S_n . However, if the daughter nucleus is generated in an excited state of energy E_x , $E_S = S_n + E_x$.

I.3 Experimental considerations

Finally, two important properties of the invariant mass method must be mentioned: the relative energy resolution is proportional to the square root of the incident energy per nucleon [Nakumura 95] which allows to use rather energetic beams. Hence by increasing the energy, we can perform the experiment using a thick target. Furthermore, in inverse kinematics at intermediate and high incident energy, the fragments of interest are focused forwards which considerably reduces the surface that must be covered by the detectors.

In the next chapter we will describe the setup used for our reverse kinematics experiment. It included beam tracking detectors, silicon detector telescopes, a 4π gamma-ray array and a large acceptance neutron wall.

Chapter II

Experimental Setup

In this chapter the experimental setup used in the Coulomb Excitation of ^{26}Ne is described. The experimental goal was to obtain the excitation energy spectrum of ^{26}Ne using the invariant mass method. As explained in Sec. I.3.4, this requires a complete kinematics measurement of all reaction products, *i.e.* charged fragments, neutrons and gammas.

The experiment was carried out at the RIKEN Accelerator Research Facility (RARF) [Yano 89], using the RIKEN Projectile fragment Separator (RIPS) [Kubo 92]. The ^{26}Ne beam was produced using projectile fragmentation of a stable beam of ^{40}Ar . A description of the facilities is given in Sec. II.1, the detector systems used for incoming and outgoing nuclei, and for γ rays and neutrons are respectively described in Sec. II.2 and Sec. II.3 is devoted to electronics and data acquisition system.

II.1 Production of Secondary Beams

II.1.1 The RIKEN Projectile fragment Separator (RIPS)

The RIKEN Projectile fragment Separator is part of the RIKEN Accelerator Research Facility (RARF), see Fig. II.1. A scheme of the RIPS is presented

II.1 Production of Secondary Beams

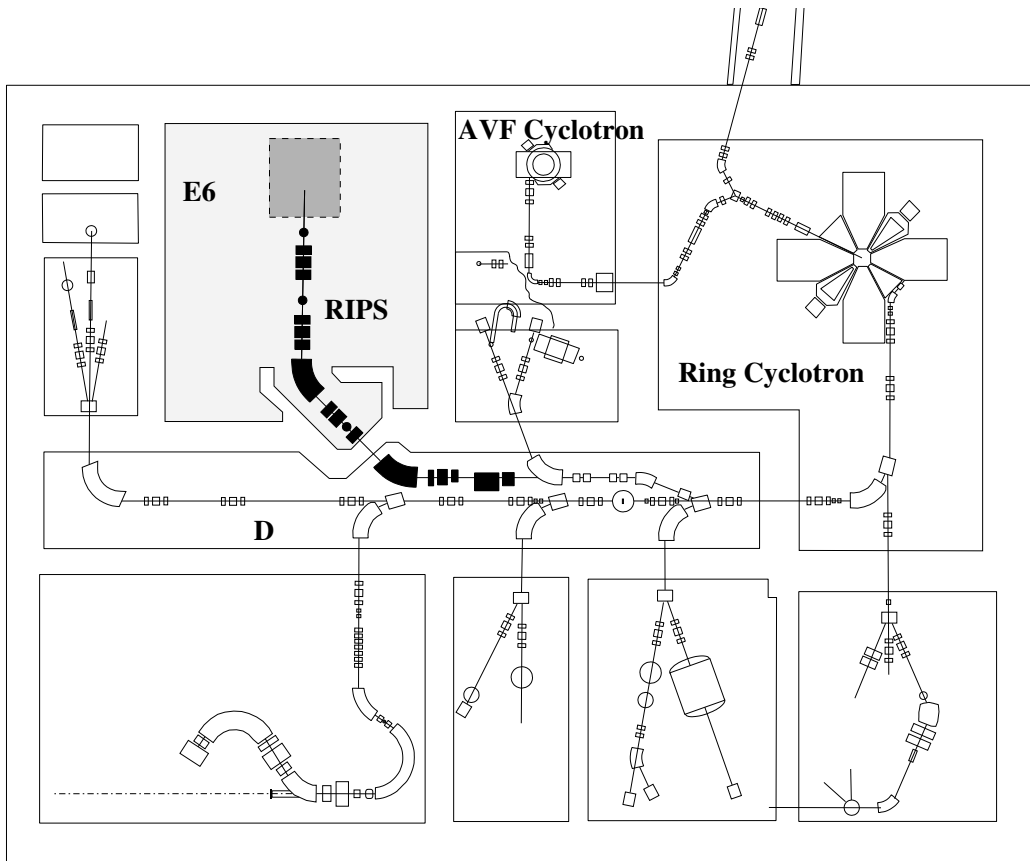


Figure II.1: Schematic layout of the RIKEN Accelerator Research Facility. A stable ^{40}Ar beam was accelerated by the ring cyclotron and was transported through the beam transport line onto the production target of the RIPS, in room D. Thought, the experimental area lays in E6 room, with the rest of the spectrometer.

in Fig. II.2. It is composed of two 45° dipole magnets (D1 and D2), twelve quadrupoles (Q1 to Q12) and four sextupoles (SX1 to SX4). It can be divided into three sections :

1. The section from the production target at F0 to the first focus point F1 includes the first dipole magnet D1 which gives a dispersive focus and analyzes the magnetic rigidity of projectile fragments.
2. From F1 to F2, the dispersion is compensated and the beam is refocused

at the achromatic focal plane F2.

3. Finally the last quadrupole triplet refocuses the beam onto the experimental focal point F3.

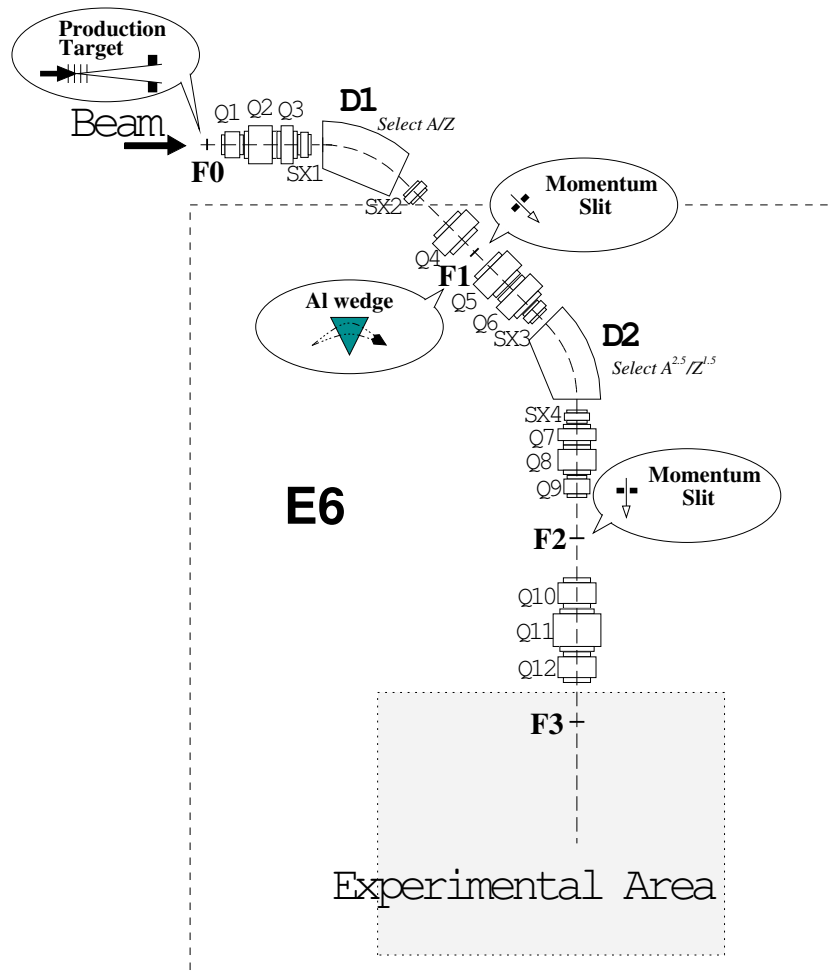


Figure II.2: Layout of the RIKEN Projectile fragment Separator. The primary beam impinges on the production target at F0 point. Projectile-like fragments are analyzed and selected in two steps, first by a dispersive D1 magnet to F1 focal point then refocused by D2 magnet to F2 focal point. Finally the secondary beam is focused on F3 focal point where the reaction target and detection setup are installed

II.1 Production of Secondary Beams

The production of a secondary exotic beam in those conditions is achieved using the projectile-like fragmentation reaction of an intense primary heavy-ion beam impinging onto a light production target placed at F0. A large variety of nuclei are created and emitted at forward angles with almost the same velocity as the primary beam. The first dipole magnet provides a magnetic rigidity $B\rho = p/Q$ selection, with p the momentum and Q the charge of the fragment. For nuclei of mass number $A \lesssim 80$, species are fully stripped [Imai 04] so that the magnetic rigidity is directly proportional to the A/Z ratio. Nuclei are then selected by interposing a slit at the exit of the first dipole magnet.

After this A/Z selection, nuclei pass through a wedge-shape degrader installed at the focal point F1, where the energy loss properties modify the rigidity. The wedge shape allows to compensate the momentum dispersion for a given isotope*. After passing the second magnet D2, slits placed at its exit select the ions with a $B\rho$ approximately proportional to $A^{2.5}/Z^{1.5}$ [Dufour 86].

Finally, the selected isotopes are transported to the achromatic focal plane F3 where the experimental setup is placed.

II.1.2 Production of the ^{26}Ne beam

In this experiment, the primary beam was ^{40}Ar at 95 MeV/n with an average intensity of 60 pA. The production target was a 2 mm thick ^9Be plate. We used, for the ^{26}Ne beam production, a 700.0 mg/cm², 3.3° Al wedge-shaped degrader at F1. ^{26}Ne beam was produced with an energy of 58 MeV/n, a 80% purity, an average rate of 10⁴ pps and a momentum spread of 2%. For calibration purposes other beams were produced and they are detailed in Table II.1.

Due to the presence of silicon detectors setup located close to the beam

*The thickest part is placed across the path of the highest energy nuclei which then loose more energy than the lowest energy isotopes which cross the thinnest part of the wedge.

axis nearly 2 m after the normal focal point F3, RIPS was tuned to focus on the empty center of the silicon hodoscope in order to minimize the number of beam particles hitting directly the silicon detector. The beam spot size at the target was 1.9 cm (FWHM) horizontally and 2.2 cm (FWHM) vertically, see Sec. III.1.2 for a detailed analysis.

II.1.3 Cyclotrons tuning and radio frequency

The stable ^{40}Ar beam was accelerated by two cyclotrons placed in series: the K70 AVF cyclotron is used to inject the beam into the K540 ring cyclotron, see Fig. II.1. To accelerate ^{40}Ar with a 17^+ charge state at 95 MeV/n, the Radio Frequency (RF) of the K540 is 28.1 MHz. The AVF radio frequency, which is tunable from 12 MHz to 24 MHz, is tuned with a frequency of 14.05 MHz to be in phase with the ring cyclotron. Theoretically, to one bunch in AVF should correspond one bunch at the ring cyclotron exit. However two bunches 35.6 ns ($1/28.1$ Hz) apart from each other are often observed, the one with biggest amount of particles called “mother” the other one “daughter”. This is due to the mixture of different turns of accelerated beam when they are extracted.

II.2 Detection System at F3 focal point

The invariant mass method requires complete kinematics measurement of all outgoing particles. Since ^{26}Ne is neutron rich, we expect it, in the high excite states, to decay essentially by neutron emission. We thus needed to record energy and position of the daughter nuclei and neutrons. However, the daughter nuclei may be produced in excited states which will decay by gamma emission. An additional gamma detector was thus required.

An overview of the whole setup is given in Fig. II.3: the ^{26}Ne beam was tracked by 2 PPACs [Kumagai 01] before the target, surrounded by the γ detector array DALI [Takeuchi 02]. The beam pipe of the RIPS was evacuated, whereas the target and detectors were set in the air. In order to

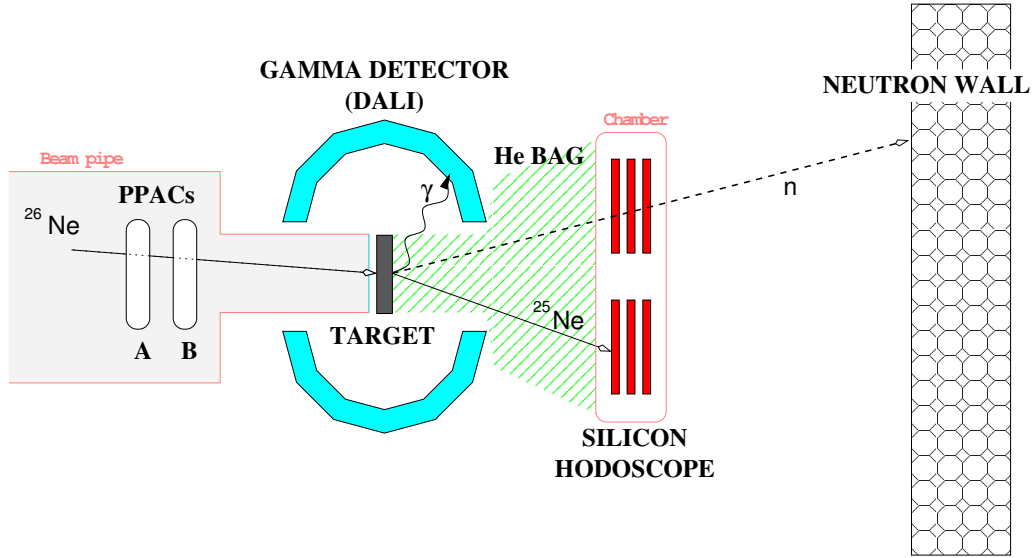


Figure II.3: Simplified scheme of the experimental setup.

limit reactions between charged particles and air after the target we placed a bag filled with helium gas till the silicon detector. Charged fragments of interest stopped in the last layer of a silicon hodoscope, ~ 1.3 m downstream from the target. Neutrons were detected in a neutron plastic array, 3.6 m downstream from the target.

In the following sections, we will describe the geometries and the characteristics for the beam line counters, the hodoscope for charged fragment collection, the 4π gamma detector and finally the neutron detector wall.

II.2.1 Beam line counters and Targets

The nuclei of interest were selected on an event-by-event basis using the Time of Flight (TOF) method. To achieve this goal, a thin (0.5 mm) plastic scintillator was placed at F2 focal point. This detector was also the timing trigger for electronics. RF being the Radio Frequency signal from the cyclotron, the RF-Plastic_{F2} time difference provides the TOF between F0 and F2 (*i.e.* a path length of 21.3 m). It has been used for beam particle identification

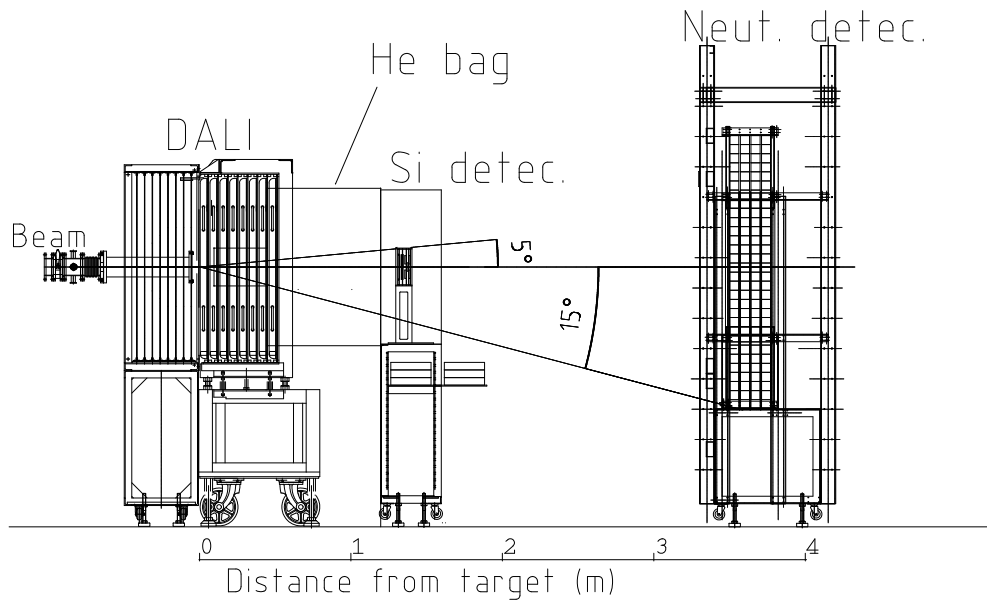


Figure II.4: Scaled overview of setup. It shows position length and maximum acceptance angle for charged particle (5°) and for neutrons (15°).

(Sec. III.1.1).

To achieve a better resolution in the reconstruction of the invariant mass, the information on the position and the angle of the incident nuclei on the target is necessary. For this purpose, the beam was tracked by two parallel-plate avalanche counters (PPAC) placed upstream of the target respectively at 148 cm for PPACa and at 118 cm for PPACb. They are of delay-line type [Kumagai 01], in which two $100 \times 100 \text{ mm}^2$ cathode plates with 2.4 mm pitch strips in horizontal and vertical axis are installed. The strips were connected by a chain of delay lines and the difference between time signals (left and right or up and down) directly provides the incoming charged particle position. Typically the resolution of these PPACs is 1.5 mm in r.m.s, which correspond to 6 mm position resolution on the target.

The beam line section under vacuum was terminated by a $25 \mu\text{m}$ kapton window right before ($\sim 2 \text{ cm}$) the target plate.

II.2 Detection System at F3 focal point

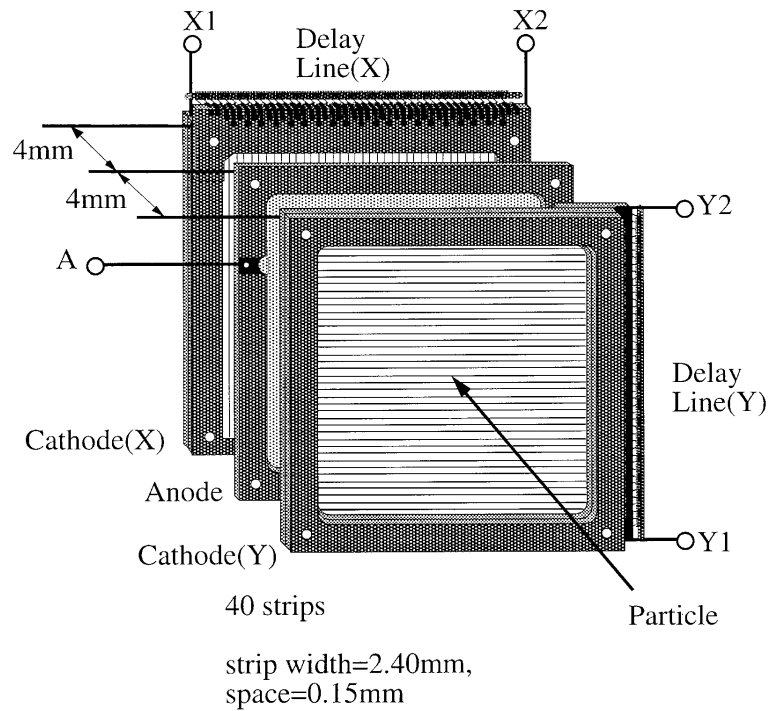


Figure II.5: Exploded view of the delay line parallel avalanche counter (PPAC)
[Kumagai 01]

As explained in Sec. I.3.1, heavy target nuclei strongly induce Coulomb excitations. In this experiment we used natural $10 \times 10 \text{ cm}^2$ Pb of 230 mg/cm^2 thickness. For further subtraction of nuclear excitation, $10 \times 10 \text{ cm}^2$ ^{27}Al of 130 mg/cm^2 was chosen as a light target. ^{27}Al was preferred to more often used carbon target for kinematic reasons: the hodoscope presents a hole in its middle and with a light target such as carbon, most of the scattered particles could not be detected. In front of the silicon detector setup we placed the helium bag. Its entrance and exit windows were made of $16 \text{ }\mu\text{m}$ mylar[†] to minimize interactions with the charged particle of interest and the pressure inside was kept around 1 atm.

[†]Thinner than the rest of the envelope of the bag ($\sim 50 \text{ }\mu\text{m}$)

II.2.2 Hodoscope for Outgoing Fragments

In this experiment the identification of charged fragments as well as the measurement of their energy and angle were performed using eight silicon telescopes placed 1.2 m downstream of the target. One telescope was composed of two layers of silicon strip detectors (SSD) and one layer of lithium drifted silicon (Si(Li)). They were placed in air but inside an aluminum chamber to protect them from light and electronic noises. The entrance window of the chamber was made of $7\ \mu\text{m}$ aluminized mylar to minimize interactions with the incoming charged particles.

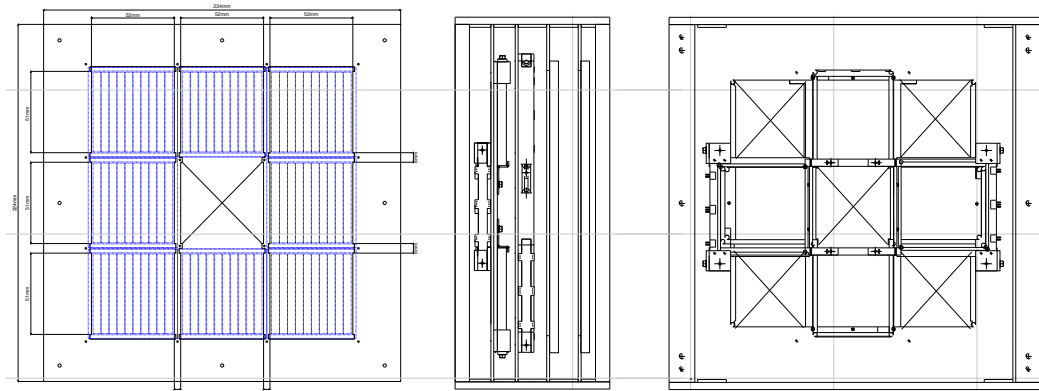


Figure II.6: Left: First layer of silicon strip detectors (SSD) , for X position measurement. We see the 3×3 matrix with a hole (\boxtimes) in the middle to avoid the beam. The 8 SSD are mounted on an aluminum frame. Each SSD is divided in 10 strips of $500\ \mu\text{m}$ each. Middle: Side view of the whole hodoscope. We see the 4 layers with from left to right: SiLi, SiLi, SSD Y, SSD X. The beam is coming from the right. Right: Back view that shows the cross-shaped last layer of SiLi, composed of 4 detectors. Again \boxtimes stands for hole. Note that this is only one layer of 4 SiLi detectors and a second one was placed upstream with the remaining 4 units.

The two first layers of SSD were arranged in a 3×3 matrix, with a hole in the middle to avoid silicon detectors to be directly hit by the beam, as presented in Fig. II.6 (left). Each SSD has a $50\times 50\ \text{mm}^2$ active area, an $0.5\ \text{mm}$ thickness and was divided into 10 strips of $5\ \text{mm}$ each. They were espe-

II.2 Detection System at F3 focal point

cially designed for this kind of invariant-mass measurement and fabricates by Hamamatsu Photonics Corporation. The first layer has vertical strips and the second layer, placed 2.2 cm downstream, horizontal strips. They respectively measure the horizontal position and the vertical position of the outgoing heavy ions. In order to reduce the number of channels, vertical strips of adjacent detectors on the left and on the right side of the first layer of the hodoscope were connected two by two, resulting in 15 cm long strips. Similarly adjacent horizontal strips on the top and bottom side of the second layer were also connected. Finally, the signal from the back sides of SSD were used for energy (ΔE) measurement.

The energy measurement was performed by 3-mm-thick lithium drifted silicons (SiLi) from the MUST[‡] array [Blumenfeld 99]. New pre-amplifiers have been built for this experiment since the original ones have a too limited dynamic range, MUST being dedicated to the detection of light particles. Due to a bigger active area of 5.5×5.5 cm², their positions were chosen to minimize the dead zones and the 8 detectors were shared among two layers of 4 units each. All nuclei of interest stopped in the SiLi detectors, allowing a total energy measurement. The particle identification (PID) was done using the E - ΔE technique, see Sec. III.3.2 for details.

II.2.3 Gamma-ray Detector

Gamma-rays were detected using the 4π detector named DALI(I and II)[§]. It consisted, in this experiment, of 152 NaI(Tl)s surrounding the target. Modules of DALI(I) consist of a scintillator of rectangular shape of $6 \times 6 \times 12$ cm³ coupled to a 5.1 cm diameter (ϕ) photomultiplier tube (PMT) giving a typical intrinsic resolution of 7% for the 1.275 MeV γ -ray of the ²²Na source [Iwasaki 01]. For the newest part, DALI(II), the size is $4 \times 4 \times 16$ cm³ and the diameter of the PMT is 3.8 cm, its resolution $\sim 8\%$ at 662 keV (¹³⁷Cs, standard source) [Takeuchi 02].

[‡]Mur à Strip, *i.e.* french for “strip wall”

[§]Detector Array for Low Intensity radiation

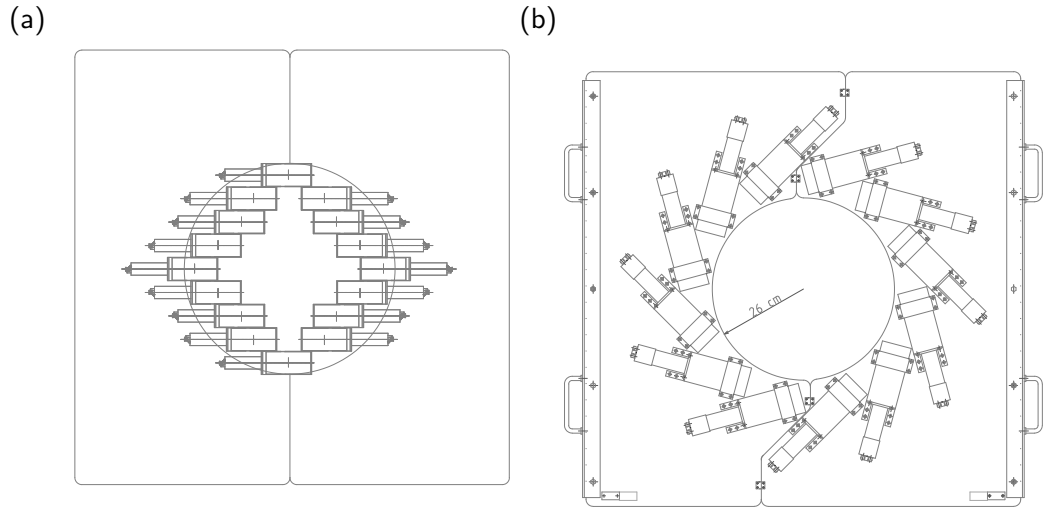


Figure II.7: (a) Front view of one typical layer of DALI(I) (b) Front face of one typical layer of DALI(II)

The whole setup counted 12 rings perpendicular to the beam axis. The 3 most upstream layers were from DALI(I), the 9 others from DALI(II). The NaI(Tl) crystals within a layer of DALI(I) are placed like bricks in a wall (see Fig. II.7(a)) whereas DALI(II) are placed in diaphragm configuration around a circle, as shown in Fig. II.7(b). The diameter of these circles is minimum for the most upstream and downstream layers (~ 40 cm and ~ 25 cm respectively) and maximum in the middle (52 cm). This geometry is a compromise between efficiency, angular resolution and simple mechanical aspects. The whole detector, presented in Fig. II.8, hence forms a sphere around the target. However, in order to increase the acceptance of the detectors placed more downstream (see following Sections), the last two layers were opened, which lead more to a vase shape (\odot) with beam axis as symmetry axis, rather than a spherical shape (\ominus).

The angular information was used for Doppler correction, since the emitting sources were beam-like nuclei with typically $\beta \sim 0.3$ (see Sec. III.2.3). For the DALI(I) part the angular resolution is 20° in average. For the DALI(II) part the angular resolution is 7° at 90° from beam direction, angle

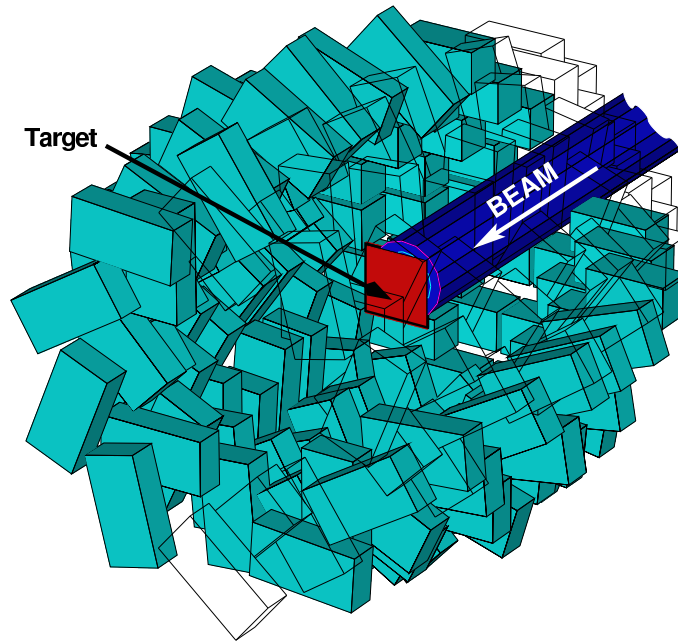


Figure II.8: Exploded view of the γ -ray detector DALI [Takeuchi 02]: only 3/4th of the setup is drawn, allowing to see inside: the end of the beam pipe and the square-shaped target.

where the Doppler effect on resolution is the most important as described in Sec. III.2.5.

II.2.4 Neutron Wall

The outgoing neutrons were detected using an array of 116 plastic scintillator rods made from BC408 material from BICRON [BICRON]. As compared to the usual BC400, BC408 offers longer bulk light attenuation length (380 cm against 250 cm) more suitable for long rods. Rods of two different length were used: the **Short Neutron detectors (SN)** have a dimension of 6 cm (thick) \times 6 cm (vertical) \times 110 cm (horizontal) whereas **Long Neutron detec-**

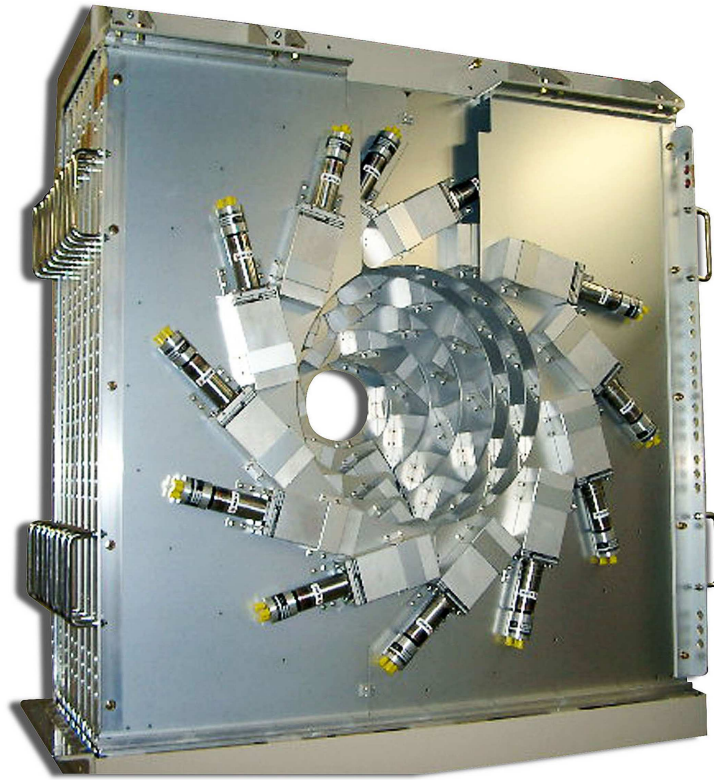


Figure II.9: Photograph of DALI(II)

tors (LN) have the same section but a length of 210 cm.

The counters were packed into 4 layers, placed side by side with only a 1.2 cm gap. Each layer consisted of 8 SN, 13 LN and again 8 SN creating a shape of a cross of dimensions 210 cm (horizontal) \times 175 cm (vertical). A diagram is displayed in Fig. II.10 . The distance between the front face of the first layer and the target was 3.6 m. The 2nd, 3rd and 4th layers were at 3.67, 3.74 and 3.81 m, respectively. Each plastic had both ends coupled to a photo-multiplier tube ($\phi = 51$ mm) for light-output read out of the scintillator. The neutron time-of-flight (TOF) was deduced from the sum of the two PMT's timings. The neutron hit position was given: in the horizontal direction by the timing difference between PMTs ; in the vertical position by identifying the rod that fired.

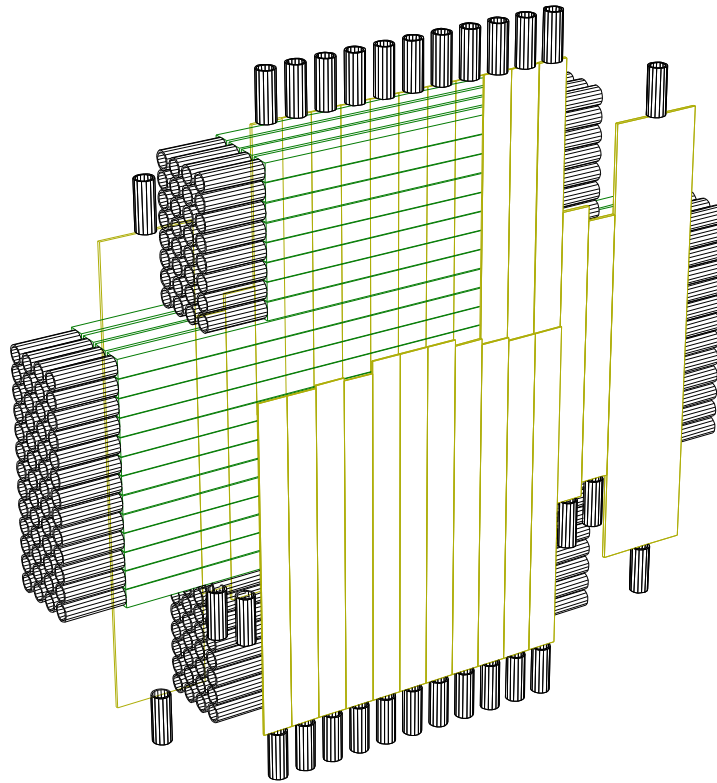


Figure II.10: Exploded view of neutron detector. One can guess the cross-shaped layers of parallelepipedic neutron detectors, equipped at both end by one photomultiplier (PMT). On the front face, the thin plastic vetoes, with almost all of them mounted with just one PMT. In reality the entire front face is covered by 28 vetoes, whereas 18 are represented here.

Thin plastic detectors (displayed in Fig. II.10) were placed right in front of the neutron wall in order to identify charged particles hitting the wall. They were used as veto detectors as well as ^{26}Ne beam dump. Their thicknesses were of 0.5 cm or 1 cm. According to the code CECIL [Cecil 79], the neutron reaction probability in these detectors is typically 3%.

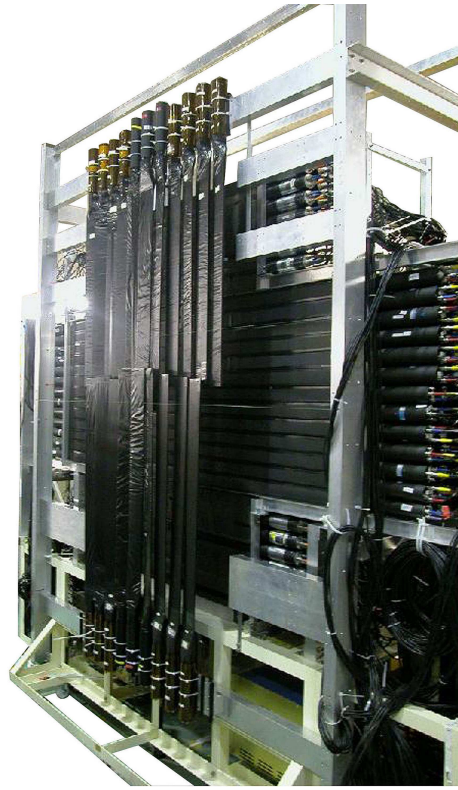


Figure II.11: Photograph of the neutron wall

II.3 Electronics and Data Acquisition

II.3.1 Triggers

The electronics schemes are displayed in Fig. II.12-II.15. Each detection component (beam, gamma, fragment, neutron) has an independent trigger made from a logical OR of time signals of individual detectors. For plastic detectors with 2 PMTs (F2 beam plastic and neutron detectors), coincidence between both PMT was required. All amplitude and time information was recorded, except time information for the strips of silicon detectors.

Beam events were defined as a hit in F2 plastic which made both ends fire, see circuit diagram in Fig. II.12. An event in SSD was defined as at least one event in the second (Y) layer to reject low energy particles, see

II.3 Electronics and Data Acquisition

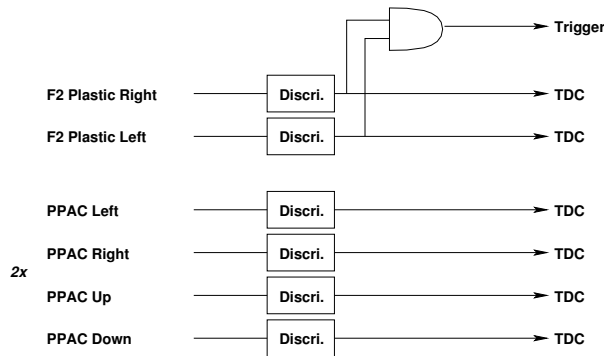


Figure II.12: Circuit diagram for BEAM detectors.

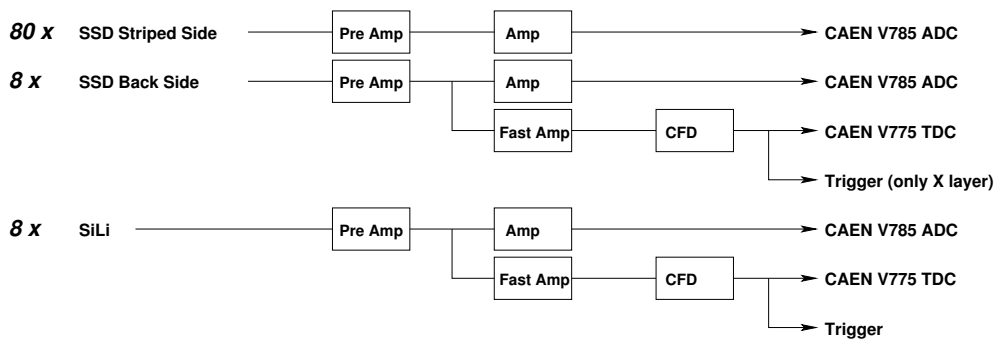


Figure II.13: Circuit diagram for silicon hodoscope.

complete electronic diagram in Fig. II.13. An event in DALI corresponded to at least one NaI crystal hit. Similarly for the neutron wall, only one hit was requested with both corresponding PMTs firing. For DALI electronic diagram see Fig. II.14 and for neutron wall Fig. II.15. Neutron wall vetoes and beam PPACs data were not part of any triggers and were recorded for each event.

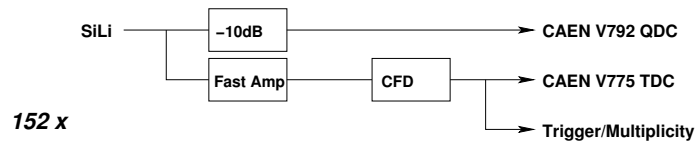


Figure II.14: Circuit diagram for DALI.

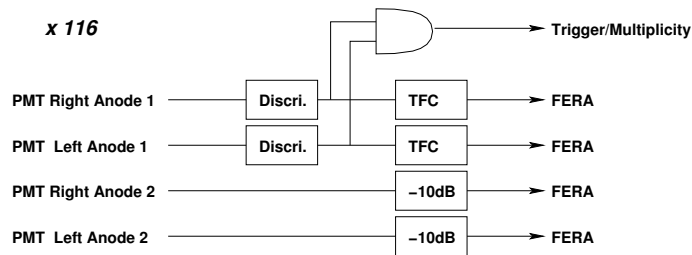


Figure II.15: Circuit diagram for neutron wall.

Four individual triggers were defined as follow :

$$\begin{aligned}
 BEAM &= F2 PLASTIC LEFT \otimes F2 PLASTIC RIGHT \\
 NEUT &= \bigoplus_{ALL} (PLASTIC LEFT \otimes PLASTIC RIGHT) \\
 DALI &= \bigoplus_{ALL} NaI \\
 SSD &= \bigoplus_{ALL} SSD (Y LAYER)
 \end{aligned}$$

The F2 beam plastics was used as start for time measurements. All other time signals were delayed with 300 ns on average. Individual triggers were combined to obtain the main trigger signal for the data acquisition system (DAQ), see illustration in Fig. II.16:

II.3 Electronics and Data Acquisition

$$DSB = \text{DOWN SCALED BEAM (1/500)}$$

$$BSN = BEAM \otimes NEUT \otimes SSD$$

$$BSD = BEAM \otimes DALI \otimes SSD$$

$$COIN = DSB \oplus BSN \oplus BSD$$

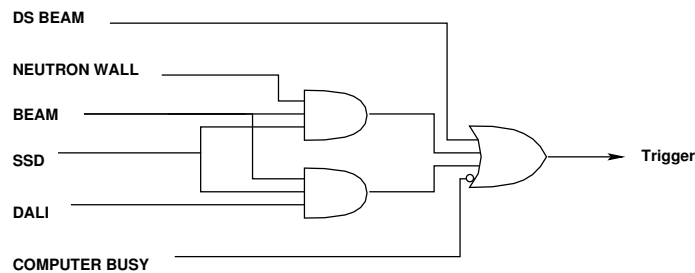


Figure II.16: Circuit diagram for total trigger.

In addition, for calibration runs, the following triggers were also used, see details in Sec. II.3.3:

$$BN = BEAM \otimes NEUT$$

$$BS = BEAM \otimes SSD$$

II.3.2 Data Acquisition System (DAQ)

The data acquisition system used here is called “BabarlDAQ” [Baba 01]. It is based on personal computers (PC) with a RTLinux (**R**eal **T**ime **L**inux) operating system connected to a CAMAC crate controller *via* a Kinetic 3922 crate controller and a Kinetic 2915 PCI Interface to 3922 ; or connected to VME *via* SBS 620 PCI-VME card and optical cable. The BabarlDAQ

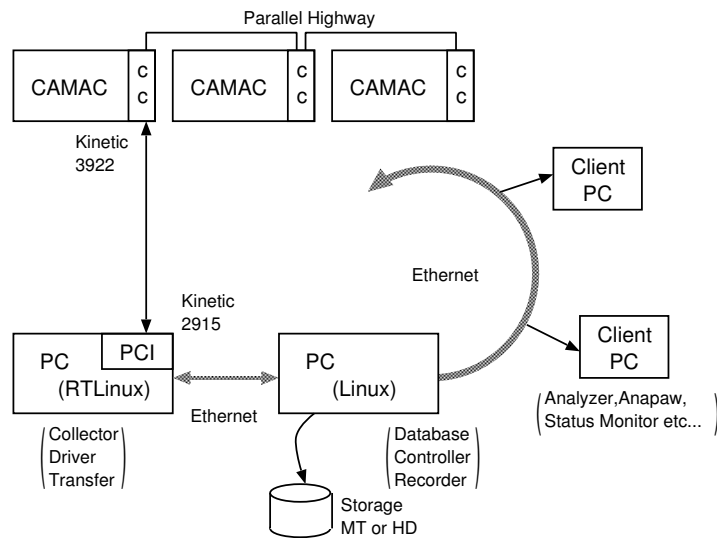


Figure II.17: Typical configuration of BabarDAQ. Some client PCs can lie on the Ethernet

processes each event using a PC instead of an auxiliary crate controller. It can store data on hard-drive or magnetic tape and most of its component can be distributed to other PCs via Ethernet.

The on-line control and histogramming is made using “Anapaw” [Baba 01], an analysis software based on the CERN Program Library PAW [Brun 89]. It can be run on-line by analyzing data from BabarDAQ through the Ethernet or off-line reading data files.

II.3.3 Data sets

Experimental data were taken under several conditions as summarized in Table II.1. Mainly, RIPS tuning was done to produce ^{26}Ne which impinged on lead or aluminum targets or labeled “empty runs” *i.e.* without target, for background measurement.

Furthermore, for silicon hodoscope calibration, three different energy (50, 55 and 60 MeV/n) ^{25}Ne beams were prepared. For neutron detector calibration four different energy (30, 40, 50 and 70 MeV/n) secondary proton beams

II.3 Electronics and Data Acquisition

and a 87 MeV/n tritium beam were tuned. The tritium run was performed because of its high kinetic energy, which allowed it to penetrate deeply into the plastic wall. A run was performed using a very thick target (here ≈ 1 cm brass) in order to produce photons at the target position to calibrate the neutron time of flight. The method is described in Sec. III.4.3.

Beam	Energy (RIPS D2 magnet)	Momentum spread	Target	Trigger	Beam Events
^{26}Ne	58.6 MeV/n	$\Delta P/P = 2\%$	Pb	COIN	$16.5 \cdot 10^8$
^{26}Ne	58.6 MeV/n	$\Delta P/P = 2\%$	Al	COIN	$6.8 \cdot 10^8$
^{26}Ne	58.6 MeV/n	$\Delta P/P = 2\%$	<i>none</i>	COIN	$3.1 \cdot 10^8$
^{26}Ne	58.6 MeV/n	$\Delta P/P = 2\%$	Brass	BN	
proton	29.6 MeV/n	$\Delta P/P \approx .5\%$	Pb	BN	
proton	29.6 MeV/n	$\Delta P/P \approx .5\%$	<i>none</i>	BN	
proton	40.3 MeV/n	$\Delta P/P \approx .7\%$	Pb	BN	
proton	49.7 MeV/n	$\Delta P/P \approx .7\%$	Pb	BN	
proton	69.7 MeV/n	$\Delta P/P \approx .7\%$	Pb	BN	
tritium	87.7 MeV/n	$\Delta P/P \approx .1\%$	Pb	BN	
^{25}Ne	60.0 MeV/n	$\Delta P/P = .1\%$	Pb	BS	
^{25}Ne	55.3 MeV/n	$\Delta P/P = .1\%$	Pb	BS	
^{25}Ne	49.5 MeV/n	$\Delta P/P = .1\%$	Pb	BS	

Table II.1: Data set summary. For details on trigger see Sec. II.3.1. Beam events are calculated taking into account live time from acquisition

Chapter III

Data Analysis

As described in the previous chapter, our experiment involved several types of detectors, for which a specific calibration and analysis treatment should be performed. This will be presented within this chapter. It is organized in the same way as the description of the setup, *i.e.* from upstream to downstream. Hence the Sec. III.1 is devoted to the calibration of beam detectors, beam tracking and identification. Sec. III.2 deals with the characteristics of the γ -ray array. Sec. III.3 is dedicated to the calibration of charge particle silicon detector and particle identification. Finally, neutron wall calibration procedures are described in Sec. III.4.

III.1 Beam

The nuclei of interest were produced by fragmentation of a primary stable beam. This section presents the calibration of the secondary beam detectors. In a first step we present the beam particle identification, then we move to beam tracking and finally explain the alignment procedures of the beam detectors with the silicon telescopes placed downstream.

III.1.1 Particle Identification

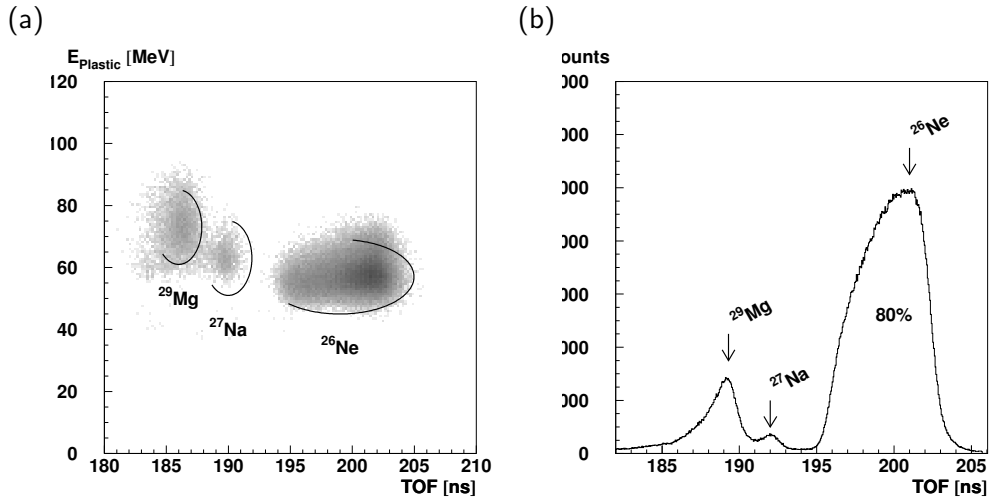


Figure III.1: (a) Energy loss in F2 plastic versus TOF for the cocktail beam. (b) TOF measurement of secondary beam nuclei, with identification.

The secondary exotic ^{26}Ne beam was obtained with the RIKEN Projectile Fragment Separator (RIPS) spectrometer from the stable ^{40}Ar beam as presented in Chapter II. During the experiment, the particle identification of the beam was performed using a calibrated silicon detector placed at F2 and the F0 to F2 time-of-flight. Fig. III.1 (a) shows the amplitude from F2 plastic instead of the F2 silicon versus the TOF information. Calibration of ΔE signal was performed thanks to the theoretical energy loss of the identified nuclei in the plastic. We superimposed the identification, obtained by comparing the position of the nuclei with theoretical calculations from code Intensity [Winger 92].

The F0 to F2 TOF is obtained from a time measurement using the plastic located at F2 and the RF signal of the cyclotron which is known to shift, here within 0.5 ns, in the course of an experiment. We correct this effect by applying a correcting time offset for each run, obtained from the time shift of each three nuclear species present in the cocktail beam (see below).

The average purity of the ^{26}Ne beam is $\approx 80\%$, the main contaminant being ^{27}Na ($\approx 5\%$) and ^{29}Mg ($\approx 15\%$). Due to a good separation of the nuclei in time, the identification could be performed using the time-of-flight information only. The identification resulting from TOF measurement, after calibration, is illustrated in Fig. III.1 (b).

III.1.2 PPAC calibration and beam profile

The incident beam profile was monitored using two parallel-plate avalanche counters (PPAC A and B) placed in the F3 chamber ≈ 120 cm in front of the target. A typical profile of the beam on these detectors is displayed in Fig. III.2 (a). The sizes in Full-Width Half-Maximum (FWHM) are $\Delta X = 35$ mm and $\Delta Y = 41$ mm for PPAC A and $\Delta X = 29$ mm and $\Delta Y = 37$ mm for PPAC B. The angular spread of the beam is measured to be $\Delta\theta_X = 1.4^\circ$ and $\Delta\theta_Y = 1.2^\circ$ as shown in Fig. III.2 (c). The position in PPAC is obtained from the time difference between both sides of a delay line for both horizontal (X) and vertical (Y) directions, namely:

$$x \text{ [mm]} = c_x \times (T_{\text{right}} - T_{\text{left}}) + X_0^{\text{offset}}, \quad (\text{III.1})$$

$$y \text{ [mm]} = c_y \times (T_{\text{down}} - T_{\text{up}}) + Y_0^{\text{offset}}, \quad (\text{III.2})$$

where $T_{\text{right, left, down, up}}$ are PPAC timing information with respect to the F2 plastic and c_x or c_y are constants for time to length conversion. These constants are obtained before the experiment by injecting a pulser signal at one side of the delay line and by measuring the time difference between left and right side or up and down, for which we know the corresponding length. Typically $c_{x,y} \approx 1.3$ mm/ns.

If a single event occurs in PPAC, the sum $T_{\text{right}} + T_{\text{left}}$ (or $T_{\text{down}} + T_{\text{up}}$) should be constant. Multi-hit events will lead to a smaller value for the time sum*. Consequently, by setting gates as illustrated in Fig. III.3, we reject partly beam pile-up events.

*If the device is hit in more than one place, the total distance between the hit positions and the closest side is smaller and so the timing.

III.1 Beam

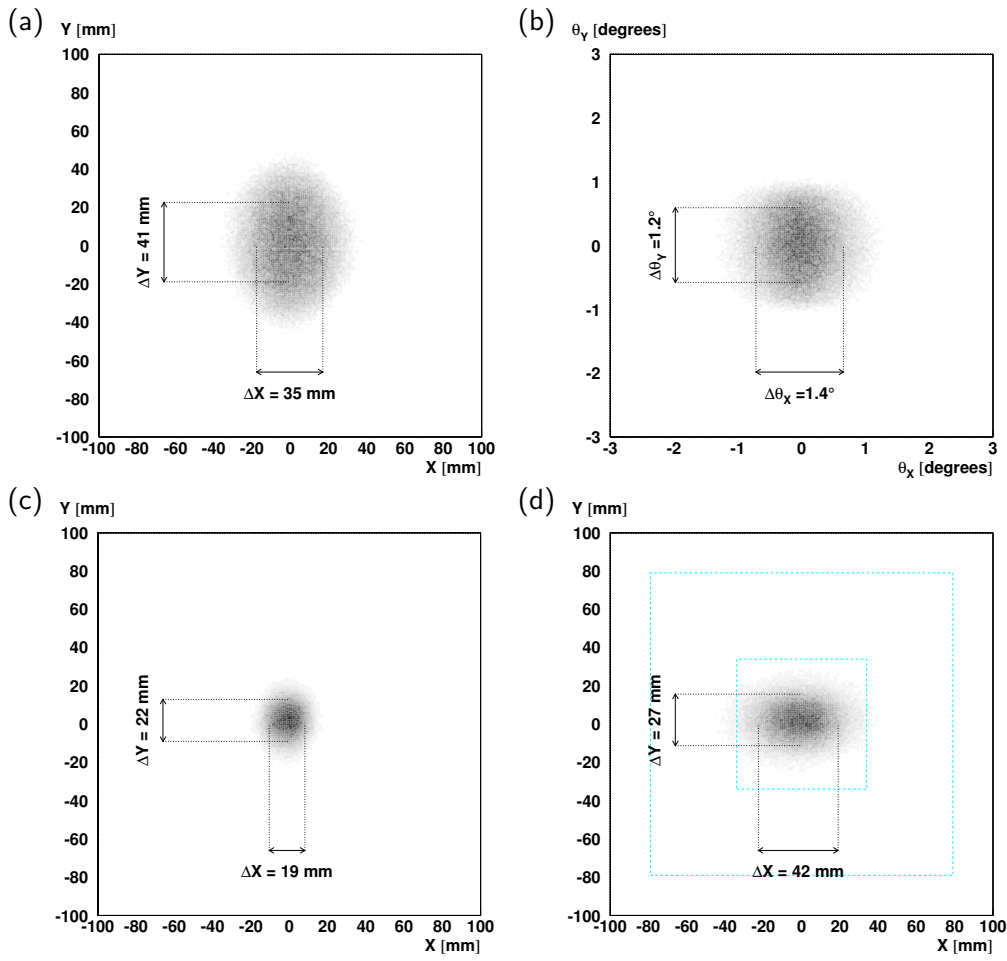


Figure III.2: (a) Cocktail beam profile at PPAC A. The profile at PPAC B looks the same with different sizes: $\Delta X = 29$ mm and $\Delta Y = 37$ mm. (b) Beam divergence angle in degrees. (c) Beam profile at target position extrapolated using PPACs. (d) Beam profile at silicon setup position extrapolated using PPACs. The dashed line sketches the position of the edge of silicon detector. In all four cases the arrow tags represent the size in FWHM.

The PPAC efficiency was estimated by comparing the number of events in F2 plastic and the number of events in PPACs. We obtained 97% and 96% for PPAC A and PPAC B respectively.

We obtained the beam profile at target and silicon setup positions, us-

ing PPAC A and B information. Results displayed in Fig. III.2 (c) and in Fig. III.2 (d) respectively show a beam spot size (FWHM) of $22 \times 19 \text{ mm}^2$ at target position and of $27 \times 42 \text{ mm}^2$ at the silicon position. We also represented in dashed line the frame of the silicon setup. The beam was tuned in order to avoid the beam to hit the silicon detectors and one can see that almost all the beam goes through the hole. However, a small tail of the beam in the horizontal direction hit the telescopes and produces noise. It was used for alignment, as described below.

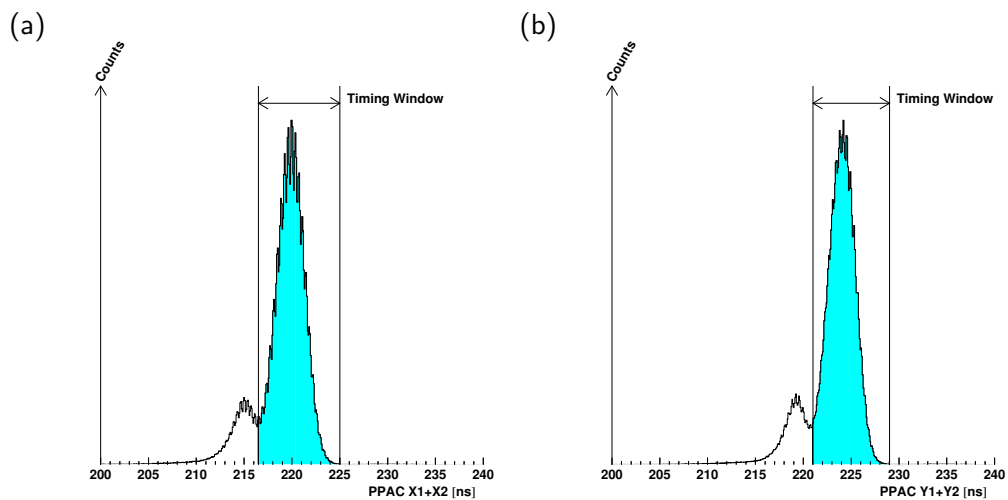


Figure III.3: Sum of time signals of both horizontal and vertical delay lines of PPAC A. Shaded area is the time gate used to remove pile-up events.

III.1.3 Alignment

The mechanical alignment of the two PPACs was done before the experiment and checked after, using in both cases a transit and a laser. The method consists in setting the laser spot position to reproduce the beam axis. A graduated mask whose center corresponds to the geometrical center of the PPAC is taped on it. The values of the possible shifts are then evaluated.

III.1 Beam

A final adjustment on the alignment of the PPACs with the silicon setup (*i.e.* the evaluation of X_0^{offset} and Y_0^{offset} parameters in Eq. III.1 and Eq. III.2) was done by comparing the position on silicon strip detectors (SSD) as extrapolated from the PPAC measurements ($X_{PPAC@SSD}$ and $Y_{PPAC@SSD}$) with the position given by the SSD themselves (X_{SSD} and Y_{SSD}), which should be equal when the incident particle is not scattered. This was done by using the ^{26}Ne beam run without target and selecting beam particles of the beam tails hitting directly the silicon detectors. Since only the relative position between PPACs and silicon setup is important, we assumed the position given by the silicon setup absolute and each SSD position known.

Then, we have to adjust each PPAC horizontally and vertically, thus 4 parameters in total. We made a linear regression with the two distributions:

$$X_{PPAC@SSD} = \Lambda_X X_{SSD} + \Delta_X, \quad (\text{III.3})$$

$$Y_{PPAC@SSD} = \Lambda_Y Y_{SSD} + \Delta_Y, \quad (\text{III.4})$$

where Λ and Δ are coefficients which, if everything is perfectly aligned, should be 1 and 0 respectively. The first term essentially probes the calibrations between the two lengths whereas the second is more directly connected to alignment. Gates on the two distributions $\Delta'_X = X_{PPAC@SSD} - X_{SSD}$ and its equivalent Δ'_Y were set around the peak to suppress events being scattered in helium bag or windows because they correspond to large values of Δ'_X or Δ'_Y . It also provided a cross check for alignment. Results after correction for Δ_X as well as X linearity is displayed in Fig. III.4, and the shifts applied on PPACs and their effect are listed in Table III.1.

The width of the $X_{PPAC@SSD} - X_{SSD}$ (respectively $Y_{PPAC@SSD} - Y_{SSD}$) distribution is ≈ 7.5 mm. It can be reproduced by the error generated by SSD position measurement (for 5 mm strips: $\sigma = 5/\sqrt{12} = 1.5$ mm), the error on the PPAC extrapolation on SSD ($\sigma \approx 7$ mm), as well as the error due to straggling in crossed material ($\sigma \approx 3$ mm). We concluded that the error generated by this method of alignment is negligible.

Direction	Offset [mm]		Δ'	Δ	Λ
	PPAC A	PPAC B			
X	-0.65	-0.2	0.03	-0.04	0.98
Y	-0.35	1.1	0.00	0.03	1.04

Table III.1: Software offset applied to PPAC position to correct their alignment with silicon detector setup and their effects. See text for the definition of Δ' , Δ and Λ .

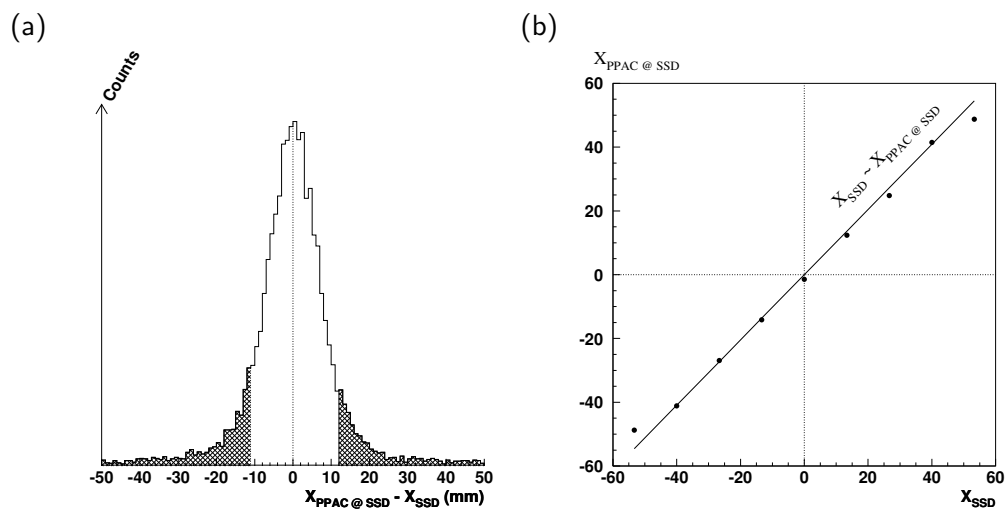


Figure III.4: (a) $X_{PPAC@SSD} - X_{SSD}$ distribution. The shaded distribution corresponds to beam particles that were scattered. Hence, for our purpose, we selected only the center part, not shaded here. (b) 2D distribution of $X_{PPAC@SSD}$ vs X_{SSD} fitted by linear function

III.2 γ -rays

As described in Chapter II the reaction target was surrounded by a 4π NaI γ -ray detector DALI. In the following, the energy calibration procedure, the detection efficiency, the Doppler shift correction and the background reduction methods, as well as the resolution are discussed. All these procedures

III.2 γ -rays

were performed with the whole array of 152 modules selecting events with multiplicity one.

III.2.1 Energy calibration

The energy calibration of the NaI of the DALI array was done using standard γ -ray sources of ^{22}Na (511 keV and 1275 keV), ^{60}Co (1173 keV and 1333 keV), ^{137}Cs (662 keV), and the mixture of Am-Be (4439 keV, 3928 keV and 3417 keV). The individual energy distributions are shown in Fig. III.5.

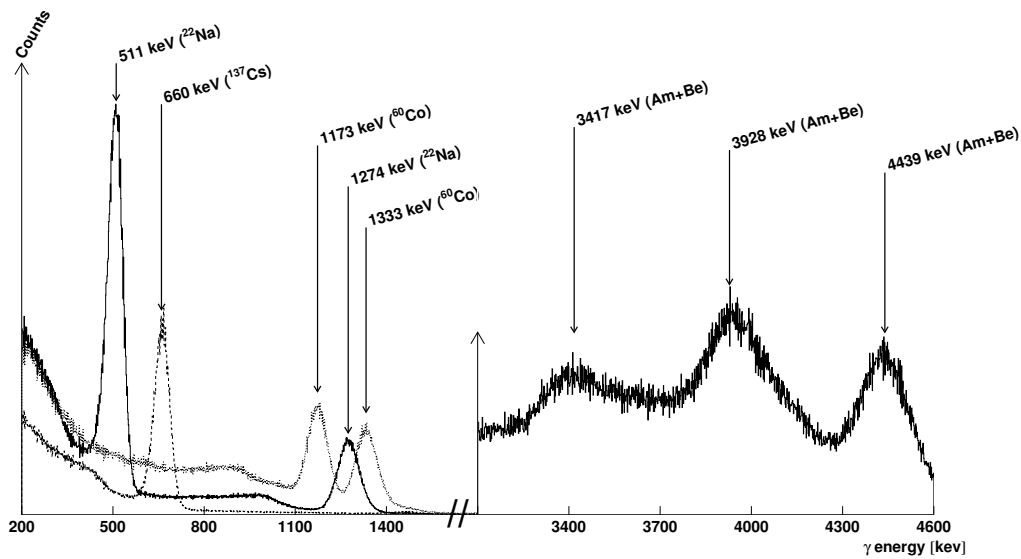
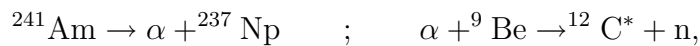


Figure III.5: Illustration of the different observed γ -ray spectra in DALI from standard sources.

In the case of the mixture of ^{241}Am and ^9Be the presence of three peaks is due to the reactions:



where $^{12}\text{C}^*$ immediately de-excites to the ground state by emitting a γ -ray at 4.439 MeV. But at that energy, pair production $\gamma \rightarrow e^+ + e^-$ occurs with

a large probability in detector material. The annihilation $e^+ + e^- \rightarrow 2\gamma$ in the matter produces two 511 keV γ -rays which can escape from the detector. This results in three peaks in the NaI detector at 4.391 MeV, $4.391 \text{ MeV} - 511 \text{ keV} = 3.928 \text{ MeV}$ and $4.391 \text{ MeV} - 2 \times 511 \text{ keV} = 3.417 \text{ MeV}$.

Table III.2 shows the comparison between the tabulated γ energies and the values deduced after the calibration for the whole array. The resolution weighted average deviation of 0.3% was retained as the systematic uncertainty on the γ -ray energy.

A simulation using the Geant 3 code [Brun 86] was performed to reproduce the energy spectra of the whole detector for all energies. Geant 3 being not able to simulate the intrinsic resolution, it was convoluted with simulations output. The resolution was determined by using ^{137}Cs standard source which gave the coefficient of proportionality for the dependence of the resolution in the square root of the energy, as explained in detail in Sec. III.2.5. A comparison of a simulated energy spectrum with the experimental ^{60}Co spectrum is shown in Fig. III.6 (a). The background, also shown in Fig. III.6 (a), was not simulated in Geant 3, but measured by removing all sources and putting DALI in self triggering mode. It was normalized on the high energy part of the spectrum.

III.2.2 Photo-peak efficiency

The energy dependence of the efficiency was calculated using Geant 3. It was checked for some energies by using standard sources, whose initial intensity and date of production is known. We hence estimated how many γ -rays they produce now *via* the element half life and the branching ratio. By counting the number of detected photons using DALI self trigger, we deduced its efficiency. The Am-Be source was placed inside a 2 cm high, 1 cm radius cylindrical lead shield against neutrons. From an attenuation length of 0.483 cm^{-1} , we estimated by Monte-Carlo simulation that only 10% of the produced γ -rays were able to emerge from the shield.

As can be seen in Fig. III.6 (b), the simulation reproduces nicely the

III.2 γ -rays

Source Type	γ Energy:			
	Tabulated [keV]	Measured [keV]	Deviation [%]	Resolution (σ) [keV]
^{137}Cs	661.660	660.6	0.16	28.5
^{60}Co	1173.237	1173.6	0.03	30.0
	1332.501	1335.8	0.25	34.0
^{22}Na	1274.532	1275.9	0.11	34.7
	511.	506.2	0.94	23.5
$^9\text{Be} + ^{241}\text{Am}$	4439.1	4435.	0.09	76.6
	3928.1	3939.	0.28	136.
	3417.1	3418.	0.03	153.

Table III.2: Energy of γ -ray emitted from standard sources, and corresponding measured energies in the whole DALI after calibration. The deviation is defined by $|E_{\text{tab.}} - E_{\text{meas.}}|/E_{\text{tab.}}$.

trend of the energy dependence of the efficiency. However some experimental values are slightly lower and since they correspond to the same γ -ray source of ^{60}Co , we supposed its intensity was overestimated. From the discrepancies we deduce that on average the efficiency is obtained with a $\sim 10\%$ relative error.

The same computer code was used to calculate the angular acceptance of the DALI. An example is shown in Fig. III.7 (a) where the angular acceptance was determined using 1275 keV ^{22}Na source and compared to the simulated results, assuming an isotropic emission of the γ -rays. We then calculated this acceptance in the center of mass system of a ^{26}Ne emitting a 2018 keV γ -ray at a $\beta = 0.32$ velocity (Fig. III.7 (b)). We see that despite some fluctuations essentially due to some non-covered angles in the laboratory frame, the region between 40 and 140 degrees gives an average equal to 12%, close to the overall

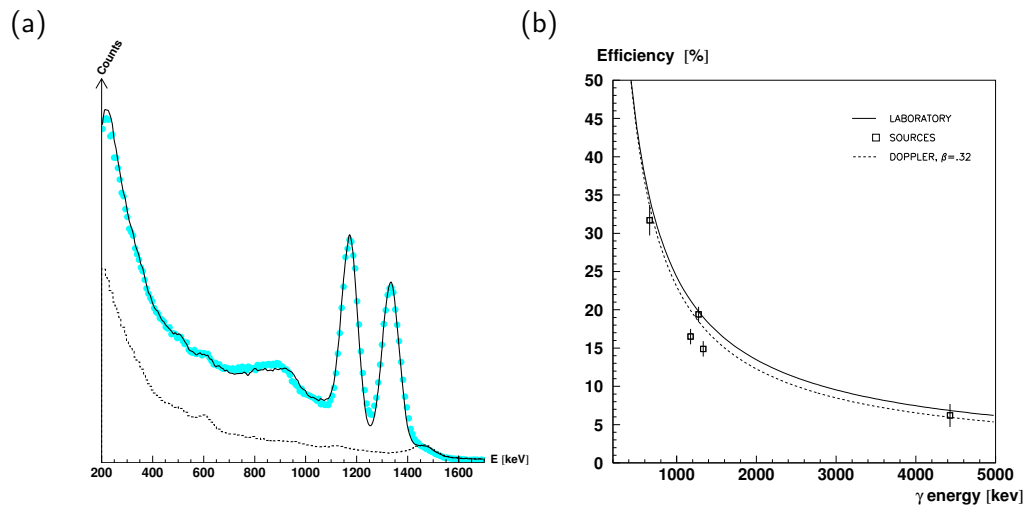


Figure III.6: (a) Deposited energy from 1173 and 1333 keV γ -ray emitted from ^{60}Co standard source (\bullet) in the whole DALI array, compared with simulation by Geant 3 (solid line). The measured background (dashed line) was added to simulation. (b) Evaluated DALI total efficiency for source emitter at rest (solid line) in addition to experimental values (\square), see details for experimental values in Sec. III.2.2. Efficiency (in %) is well reproduced by $8.7 \cdot 10^3 / E_\gamma^{0.87}$ with E_γ in keV. The dashed line is obtained by simulating a source emitting at velocity $\beta = 0.32$.

efficiency value.

III.2.3 Doppler shift correction

A γ emitted in a moving frame has its energy in the laboratory frame shifted depending on the angle between the direction of the emitter and the observer: this is called Doppler shift. In our case, the emitting nuclei were traveling at $\beta \approx 0.3$. Hence we retrieved the γ -ray energy value in the rest frame E_γ^\star using the measured energy in the laboratory frame E_γ^{lab} through the formula:

$$E_\gamma^\star = E_\gamma^{\text{lab}} \gamma (1 - \beta \cos \theta^{\text{lab}}) \quad (\text{III.5})$$

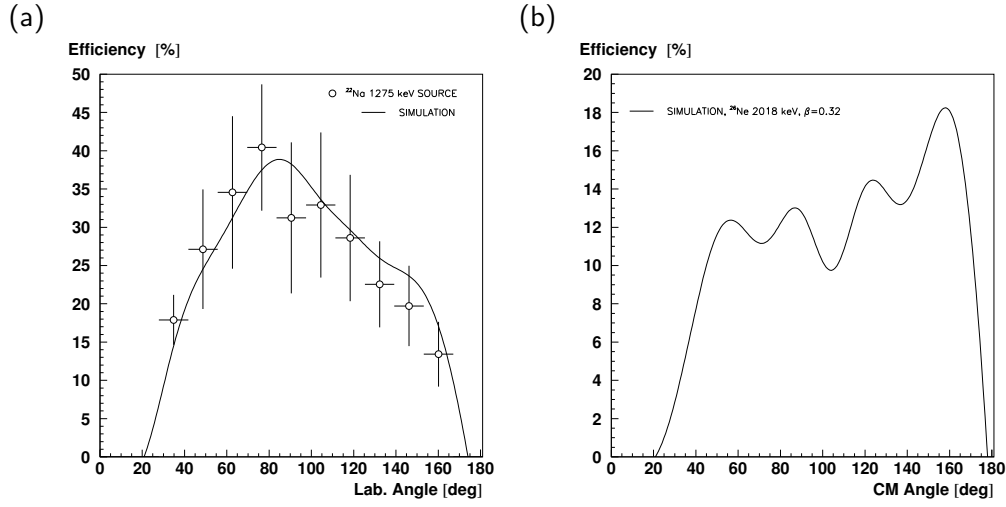


Figure III.7: (a) Acceptance of the DALI, in laboratory frame for the 1275 keV γ from ^{22}Na source. (b) Simulation of the acceptance of a 2018 keV γ emitted from a moving ($\beta = 0.32$) ^{26}Ne nucleus.

where β is the relativistic velocity and γ the Lorentz factor of the nuclei in the laboratory frame. The angle θ^{lab} was determined by the geometrical information of position of the center of the crystal, with respect to the target position where the de-excitation occurs. The angle θ^{lab} is here defined with respect to the beam axis and not with respect to the direction of the outgoing nucleus. The induced error ($\sigma \sim 1.5^\circ$) is smaller compared to the the resolution on the γ angle measurement using DALI ($\sigma \sim 2.6^\circ$) as explained below in Sec. III.2.5. The reaction was supposed to occur in the center of the target inducing a small error of $\sigma \sim 0.6^\circ$ on the angle of emission. The outgoing charged fragment crosses many materials including a thick target before stopping in the silicon and since the kinematic energy difference between the incoming nucleus and the outgoing nucleus are comparable to the kinematic energy at the center of the target, the β value at the center of the target was calculated event-by-event using the velocity of the incoming nucleus. The velocity was obtained *via* the time-of-flight of the incoming nucleus in RIPS spectrometer, in the same way as $\text{TOF}_{\text{F2} \rightarrow \text{Target}}$ was calculated in Sec. III.4.3.

A typical result of Doppler shift correction is shown in Fig. III.8 which represents the photon energy distribution obtained in coincidence with ^{26}Ne particles in the silicon hodoscope before and after Doppler correction. The γ -ray line at 2018.2 keV from $2^+ \rightarrow 0^+(gs)$ transition in ^{26}Ne is not distinguished in laboratory frame, but clearly seen in the Doppler corrected energy distribution.

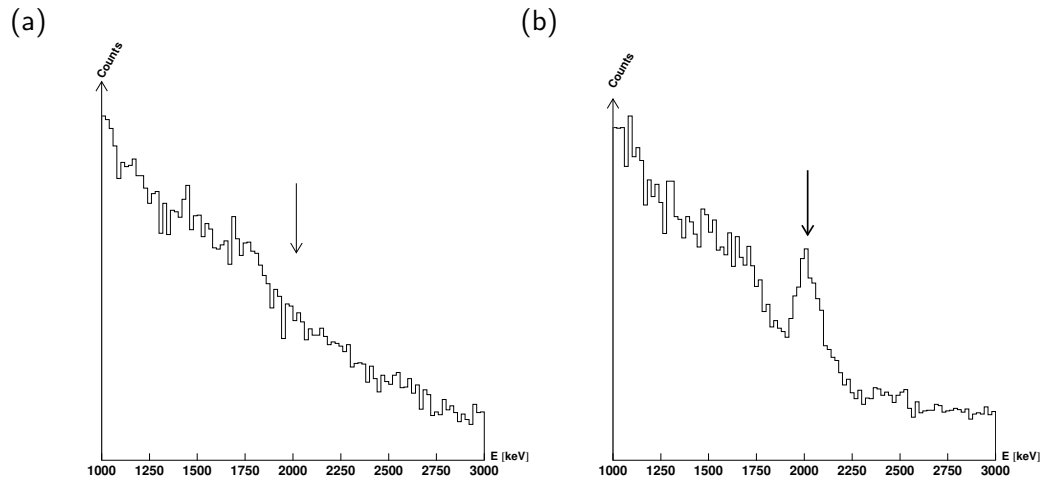


Figure III.8: Illustration of Doppler correction in the whole DALI array. (a) Deposited energy distribution in DALI, in coincidence with a ^{26}Ne fragment in the silicon hodoscope. (b) Same conditions, but Doppler corrected case with a constant $\beta \approx 0.32$. A peak at 2016 keV appears.

To test if the Doppler correction has been efficiently carried out, the energy dependence of the same γ -ray is plotted versus the detection angle, as in Fig. III.9 (a). No angle dependence is observed after the correction was applied (Fig. III.9 (a)).

III.2.4 Background reduction via time gate

NaI γ -ray detectors are not sensitive only to γ but also to neutrons or charged particles. In addition, the photons detected are not emitted only from re-

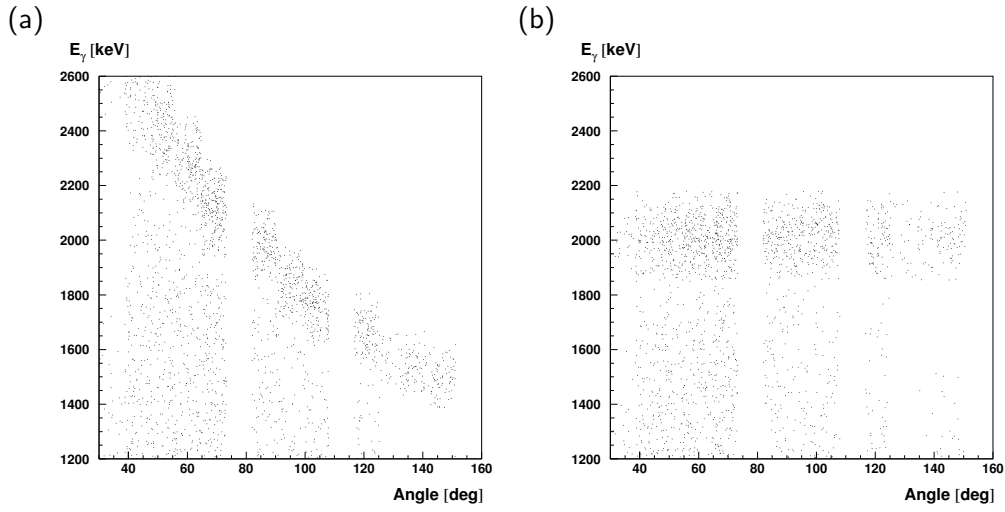


Figure III.9: Energy/angle dependence of the tabulated (2^+) 2018 keV γ -ray emitted from ^{26}Ne , (a) before and (b) after Doppler correction. The angle in degree is the position of center of NaI crystal with respect to beam direction. No obvious dependence in (b) is shown which confirms the good Doppler correction.

actions of interest but also by natural background like 1461 keV transition in ^{40}K . It is thus necessary to reduce the background of random events by setting a time window for each crystal.

The first step was to align all time spectra to set a single gate. We used the $^{26}\text{Ne } 2^+ \rightarrow 0^+$ transition γ for which the time coincidence peak was fixed to an arbitrary value of 100 ns. The summed time spectra for the $2^+ \rightarrow 0^+$ transition and for all γ energies are shown in Fig. III.10 (a) and Fig. III.10 (b) respectively. In a second step, a time window was set on the peak which rejects events on the right produced by neutrons or charged particles hitting the crystals and events on the left which correspond to random coincidences with background γ -rays.

Note the resolutions for a given detector is $\sigma \sim 1.9$ ns and for the whole detector $\sigma \sim 2.0$ ns which indicates that the timing alignment is satisfactory.

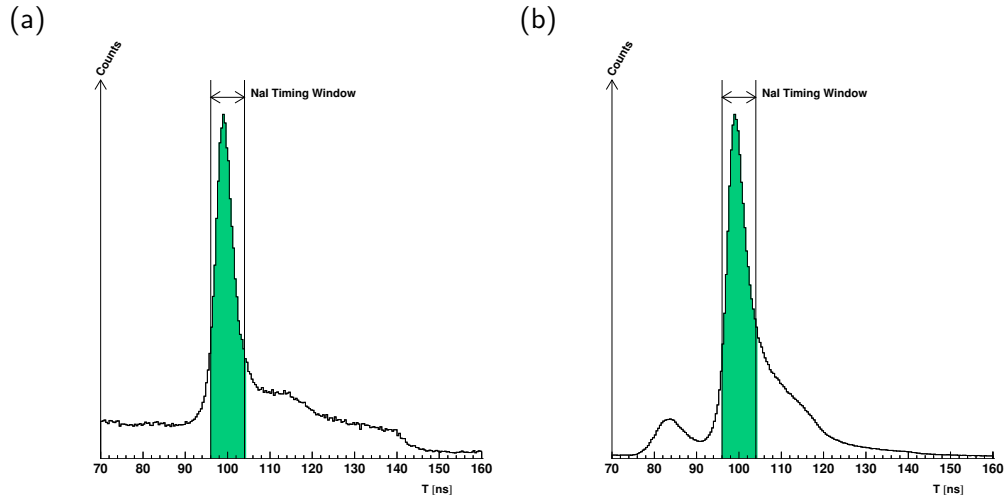


Figure III.10: Time window for the whole DALI in case of: (a) ^{26}Ne 2018 keV γ in coincidence; (b) all events. Time is shifted to 100 ns for convenience. The selected area ($100 \text{ ns} \pm 7 \text{ ns}$ *i.e.* $100 \text{ ns} \pm 3.5\sigma$) corresponds to more than 99% of ^{26}Ne 2018 keV γ events in case of Gaussian distribution.

III.2.5 Resolution and accuracy

Errors on the velocity of the emitting nuclei as well as the finite angular aperture of the crystals, lead to broaden the γ -ray peaks obtained after Doppler correction. Based on Eq. III.5, the resolution of the energy in the frame of the emitting nucleus E^\star can be written:

$$\left(\frac{\Delta E_{\gamma^\star}}{E_{\gamma^\star}}\right)^2 = \left(\frac{\beta \sin \theta^{\text{lab}}}{1 - \beta \cos \theta^{\text{lab}}}\right)^2 (\Delta \theta^{\text{lab}})^2 + \left(\frac{\beta \gamma^2 (\beta - \cos \theta^{\text{lab}})}{1 - \beta \cos \theta^{\text{lab}}}\right)^2 \left(\frac{\Delta \beta}{\beta}\right)^2 + \left(\frac{\Delta E^{\text{lab}}}{E^{\text{lab}}}\right)^2. \quad (\text{III.6})$$

The first contribution, $\Delta \theta^{\text{lab}}$, is due to the finite size of NaI crystals and is defined as the average angle between two DALI layers, *i.e.* $\Delta \theta^{\text{lab}} \approx 9^\circ$. This corresponds to a variance $\sigma_{\theta^{\text{lab}}} = \Delta \theta^{\text{lab}} / \sqrt{12} \approx 2.6^\circ$. Since here we determined the angle without taking into account neither the incident nor

III.2 γ -rays

the outgoing angle, we must add to this variance a $\sigma_{\theta\text{beam}} \approx 1.5^\circ$. The indetermination of the reaction position in target create an additional effect of $\sigma_{\theta\text{target}} \approx 0.6^\circ$. The summed contribution leads to $\sigma_{\theta\text{lab}} \approx 3.1^\circ$.

The second term is driven by the error on beam velocity due to time resolution as well as energy loss in target. We estimate it to be $\sigma_\beta/\beta \approx 1.7\%$.

Finally, the last term corresponds to the intrinsic resolution of crystals. It can be written: $\frac{\sigma E^{\text{lab}}}{E^{\text{lab}}} \propto \sqrt{E^{\text{lab}}}$ [Iwasaki 01]. The square root dependence comes from the fact that statistical uncertainty in scintillation-photon collection is the main factor which determines the intrinsic resolution. The number of photons collected is roughly proportional to the energy, thus the energy resolution must be proportional to $\sqrt{E^{\text{lab}}}$. The factor of proportionality has been determined experimentally from the test of each crystal using standard ^{137}Cs source placed closed to the crystal. We illustrated the trend in Fig. III.11 (a), where the values of the resolution were obtained during experiment, hence in different conditions. We obtained here a factor of $0.04 \text{ MeV}^{-1/2}$ and one could see that the square-root tendency is nicely reproduced.

The calculated effects of all contributions are plotted in Fig. III.11 (b). The dominant effect at all angles on the resolution comes from the intrinsic resolution. The finite size of the detector affects angles close to the beam axis whereas the spread on beam velocity plays a role around 90° . We compared our trends to the results of simulation, in good agreement. The statistic did not allow us to measure the resolution experimentally at each angle, but for the whole DALI we obtained $\sigma = 3 \pm 0.15\%$ in good agreement with the average result from simulation.

The measurement of the first well known excited state of neon isotopes from ^{22}Ne to ^{26}Ne allowed us to perform a check of the Doppler correction by identifying the corresponding de-excitation γ in coincidence with the isotope of interest in the silicon hodoscope. Results are reported in Table III.3 and shows an accuracy in average better than 1% on the energy centroid, after Doppler correction.

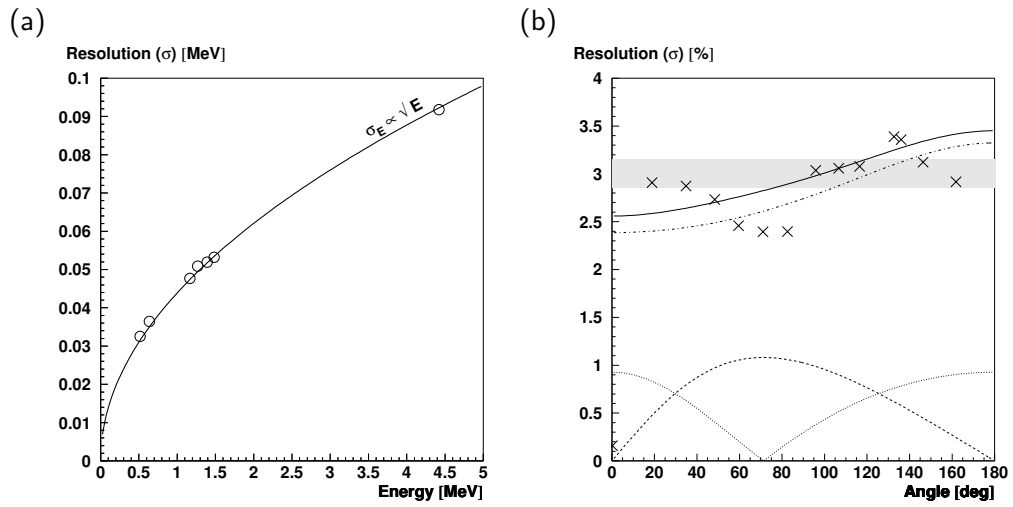


Figure III.11: (a) Experimental intrinsic energy resolution function of the γ energy for one crystal, fitted by $\sigma_E = \alpha\sqrt{E}$ function. Here $\alpha \approx 0.04 \text{ MeV}^{-1/2}$. (b) Calculated energy resolution contributions for a 2.018 MeV γ -ray from a ^{26}Ne at $\beta \approx 0.32$. Dashed line is the finite detector angle contribution, dotted line is the contribution of the spread in beam velocity, dash-dot line is the contribution from the intrinsic resolution. Finally the solid line is the quadratic sum. Cross (×) points are the result from simulation and shaded area the average from experiment.

Isotope	Tabulated γ Energy (keV)	Measured Energy (keV)	Absolute Deviation (%)
^{26}Ne	2018.2	2021.	$\approx 0.1\%$
^{24}Ne	1981.6	1980.	$\approx 0.1\%$
^{23}Ne	1701.5	1720.	$\approx 1.0\%$
^{22}Ne	1274.5	1281.	$\approx 0.5\%$

Table III.3: De-excitation γ -ray energy measured after Doppler Correction from various neon isotopes, compared with tabulated values.

III.3 Silicon detectors

Silicon strip and silicon lithium drifted detectors were placed after the reaction target in order to identify the charged fragments as well as to measure their energy. The calibrations and data analysis of these detectors are described here. We start with energy calibration and resolution, then present the methods for particle identification and we conclude by discussing the angular acceptance.

III.3.1 Energy calibration and resolution

Before the experiment, we adjusted the feed-back capacitance of the pre-amplifiers to match the energy range of the experiment. The ^{26}Ne beam had an energy of 58.6 MeV/n. The average deposited energy in the SSD layer and the Si(Li) were, according to calculations based on Bethe-Block formula, respectively 100 MeV and 1 GeV. Hence, the required energy range is a few MeV to 200 MeV in SSD and to 2 GeV in Si(Li). For Si(Li), this energy range exceeds the one of MUST array and specific preamplifiers were built at the Institut de Physique Nucléaire d'Orsay (IPN Orsay) with a gain of 1.5 mV/MeV. We also performed an estimation of the charge collection from the SSD which led us to tune their pre-amp gain to 4.4 mV/MeV. With a pulser the electronic linearity was checked by injecting different charges in the electronics chain.

To calibrate the silicon hodoscope, we prepared beams at several energies with very small momentum spread (0.1%). These secondary beams contained essentially ^{25}Ne with energies of 50, 55 and 60 MeV/n, in the same range as expected in the experiment. These beams were scattered off a lead target in order to be in the same condition of energy loss as the one during the experiment with ^{26}Ne beam. By calculating the energy losses in each layer of the hodoscope for each energy, we deduced the linear calibration functions in the region of interest. Results of calibration and comparison with expected values are presented in Table III.4.

²⁵ Ne Beam energy	E. loss SSD X [MeV]		E. loss SSD Y [MeV]		E. loss Si(Li) [MeV]	
	Calc.	Meas. (FWHM)	Calc.	Meas.	Calc.	Meas.
50 MeV/n	155.1	155.1 (4.7)	186.9	186.9 (7.5)	563.8	563.3 (28.2)
55 MeV/n	132.9	132.9 (4.1)	150.1	150.1 (5.2)	802.0	802.6 (24.6)
60 MeV/n	120.4	120.5 (3.4)	132.2	132.3 (4.7)	969.9	969.7 (20.7)

Table III.4: Calculated and measured energy losses after calibration, in the three different layers of silicon hodoscope. Error is defined as FWHM obtained with the events in all detectors (not only one) deconvoluted from beam momentum spread (negligible)

We measured the width of the elastic peak for ²⁵Ne at 60 MeV/n in the first SSD layer (X) to be 3.4 MeV (FWHM), in the second SSD layer (Y) 4.7 MeV and in the last Si(Li) layer 20.7 MeV[†]. This corresponds to the convolution of straggling effects in the crossed material by the intrinsic resolution of silicons. From the measured peak position in each detector we concluded that the resolution effect due to calibration is lower than 0.4%. While performing the Geant 3 simulation of the experiment we included the intrinsic resolution of silicon strip detector (FWHM \sim 1.5 MeV) and lithium-drifted silicons (FWHM \sim 9 MeV). The good agreement with data will be illustrated with the particle identification in Sec. III.3.2.

The angular resolution of the silicon setup placed at 1.2 m from the target with strips of 5 mm width is $\sigma = 0.07^\circ$. If we include the straggling generated by crossed materials, the simulation gives a typical value of $\sigma = 0.6^\circ$ in the center of mass for lead and $\sigma = 0.5^\circ$ for the aluminum target respectively, for ²⁶Ne at 55MeV/n.

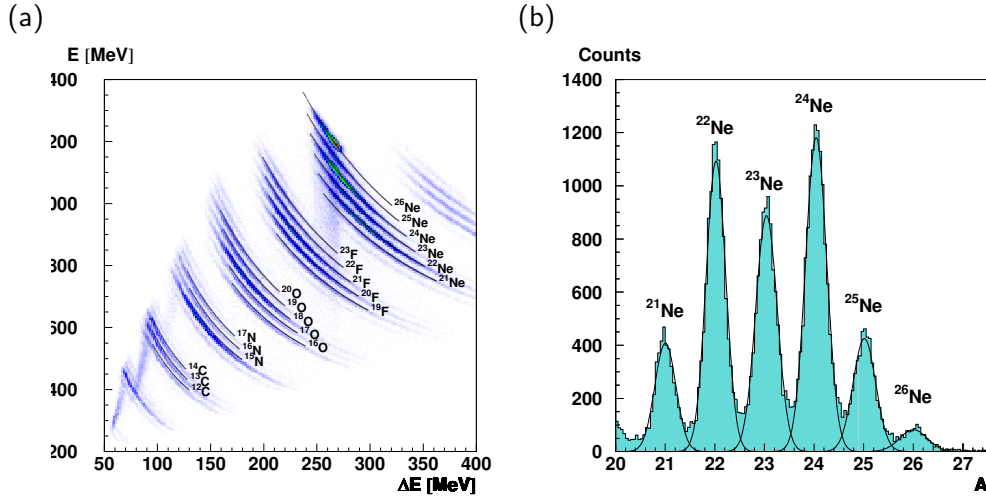


Figure III.12: (a) $E-\Delta E$ plot from silicon hodoscope from the $^{26}\text{Ne}+\text{natPb}$ reaction. (b) PID projection from $E-\Delta E$ in silicon hodoscope for Ne isotopes, detected in coincidence.

III.3.2 Particle Identification (PID)

The PID of charged fragment hitting the silicon hodoscope is done using the $E-\Delta E$ technique, where ΔE is obtained by summing the energy losses in the first and second layers of hodoscope (X and Y SSD) and E by adding to ΔE the energy deposited in the third layer (Si(Li)). A typical $E-\Delta E$ plot is shown in Fig. III.12 (a).

In order to be able to gate on different isotopes using a simple one-dimension gate, we projected the 2D distribution onto a 1D one using the formula [Goulding 85]:

$$A = \lambda \cdot (E^{\zeta+\eta\Delta E} - (E - \Delta E)^{\zeta+\eta\Delta E}) + \kappa, \quad (\text{III.7})$$

where A stands for mass number of Ne isotopes, adjusted by λ and κ whereas ζ and η were adjusted to suppress the energy dependence. This method provides a better energy independence than the simple projection onto a

[†]These values correspond respectively to 2.8%, 3.6% and 2% respectively

parabolic E - ΔE relation, and the mass number peak position interval remains constant. The results of this projection for neon isotopes in Fig. III.12 (b) shows that the peak shape is well reproduced by a Gaussian distribution. The peak position of ^{26}Ne and ^{25}Ne was checked using corresponding ^{26}Ne and ^{25}Ne secondary beam. For one isotope peak of mass A , and for lead target, the resolution achieved is $\sigma_A/A \sim 1\%$. We also test it with ^{25}Ne beam at 55 and 60 MeV/n, we achieved a mean at $A = 25.06$ ($\sigma_A/A = 0.91\%$) and $A = 25.03$ ($\sigma_A/A = 0.95\%$) respectively. We also test PID function for simulated data by Geant 3, which include both position of silicon hodoscope and resolution. We obtain $A = 24.93$ ($\sigma_A/A = 0.94\%$).

III.3.3 Geometrical acceptance

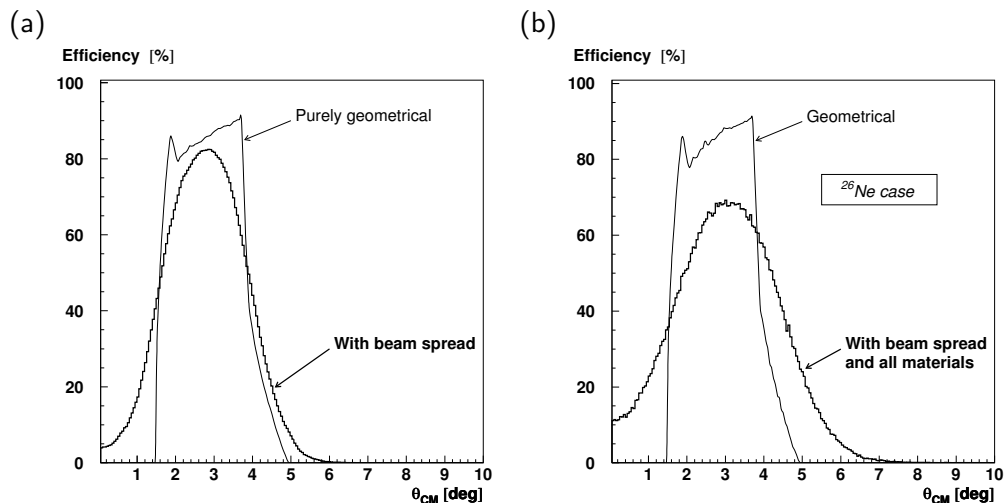


Figure III.13: (a) Angular acceptance of silicon hodoscope without and with beam angular spread effect. (b) Angular acceptance of silicon hodoscope for ^{26}Ne nucleus without and with beam angular spread effect and material angular straggling including the lead target. The angle is defined in the center-of-mass frame.

Assuming an intrinsic silicon efficiency of 100%, from Monte-Carlo simulation with Geant 3, we estimated the angular acceptance of the silicon

III.4 Neutron detection

hodoscope. The first case was purely geometrical[‡] *i.e.* we made the hypothesis that particles were emitted from the center of a infinitely thin virtual target. We only required the particles to hit the three layers of silicon. A second case was studied using real beam trajectories extracted from tracking information of the PPACs. The beam spread hence influences both incoming angle and position on target, see results in Fig. III.13 (a). One can note that efficiency at zero degree is then equal to zero no more but $\approx 4\%$.

A third study have been made for a $\beta = .32$ velocity ^{26}Ne beam and its results are displayed in Fig. III.13 (b). In the first case no spread from beam was added. There was neither the target, nor the surrounding air or He bag. This was just to test this effect of angular straggling in silicons, which appeared to be negligible. In the second case we used the experimental beam spread in angle and energy and added the target, the air and the helium bag to test the effect of straggling from upstream material. As one can expect, the acceptance interval becomes broader and the detection efficiency reaches $\sim 10\%$ at zero degree.

III.4 Neutron detection

This section deals with the neutron wall calibration. The different s of the calibration: energy, time-of-flight (TOF), position as well as their optimization are presented. They were performed, except for TOF, with the help of cosmic ray muon data taken during dedicated runs. Finally the efficiency of the detector (intrinsic and whole wall) is estimated.

[‡]With the use of the so-called *geantino* particle, a special particle in Geant 3 which never interacts but tests detectors geometry.

III.4.1 Calibration method for neutron detectors using cosmic rays

The procedure relies on the detection of cosmic-ray muon events which were accumulated in separate runs before and after the experiment. To record these events, the neutron detector wall was in self-triggering mode with the condition that at least 8 of the 116 scintillators were fired.

Muons reach the earth essentially vertically from the sky with a total energy of approximately 4 GeV [Hagiwara 02]. Their energy loss in plastic rods can be estimated by taking into account the fact that at this energy muons are located around the minimum of ionization of $\sim 2 \text{ MeV cm}^2/\text{g}$. BC408 neutron plastic rods used here have a density of $\sim 1 \text{ g/cm}^3$ and a 6 cm thickness which imply an energy loss of $\sim 12 \text{ MeV}$. A detailed analysis using simulations [Fukuda 04] for 1 GeV/c muons gives 11.7 MeV for the most probable energy loss.

Due to the small thickness of the neutron rods with respect to the cosmic ray energy, the deposited energy distribution follows a Landau distribution [Landau 44], which is characterized by a narrow peak followed by a long tail at higher energies as illustrated in our case in Fig. III.14 (a). This distribution well can be approximated by [Moyal 55]:

$$\Phi(\kappa) = \sqrt{e^{-(\kappa+e^{-\kappa})}/(2\pi)} \quad (\text{III.8})$$

where κ is proportional to the energy loss.

III.4.2 Energy calibration of light output

To properly set the detection threshold of deposited energy in the neutron scintillator rods, a calibration of light output amplitude was required. γ -rays from ^{60}Co (1.17 and 1.33 MeV[§]) as well as muon events ($\sim 12 \text{ MeV}$, see Sec. III.4.1) were used for this purpose.

[§]Hence a Compton peak at $\sim 1 \text{ MeV}$

III.4 Neutron detection

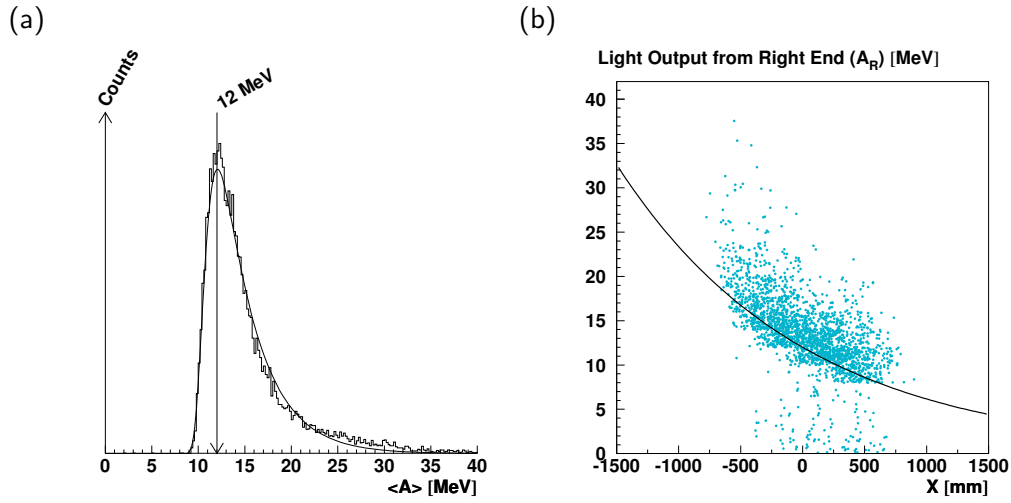


Figure III.14: (a) Experimental energy distribution of deposited energy of muons, fitted with the [Moyal 55] function. (b) Light attenuation measured using muons in a 2 m plastic rod, fitted with a $A_0 \exp(-x/\lambda)$ function, $A_0 \sim 12$ MeV and $\lambda \sim 1500$ mm.

The light attenuation effect in plastic scintillators, illustrated in Fig. III.14 (b), was studied by fitting the detector response as a function of the distance x to the center by $A_0 \exp(-x/\lambda)$, where A_0 is the energy deposited and λ is the bulk attenuation length. In an infinite bulk, λ only depends on the material properties, but here the finite geometry makes it strongly dependent on the size of the detectors. We typically obtain here $\lambda \sim 1.5$ m for 2 m long plastics, $\lambda \sim .7$ m for 2 m long rods made from two 1 m plastics glued together and $\lambda \sim .8$ m for 1 m long rod. The amplitude for a detector was then the geometrical mean of the light output at the right end (A_R) and at the left end (A_L):

$$A_L \approx A_0 e^{+x/\lambda} \quad \text{and} \quad A_R \approx A_0 e^{-x/\lambda} \quad (\text{III.9})$$

$$\Rightarrow \langle A \rangle = \sqrt{A_L A_R} \approx A_0, \quad (\text{III.10})$$

Here the middle of the plastic rod is given by $x = 0$ and $x > 0$ corresponds to the right side.

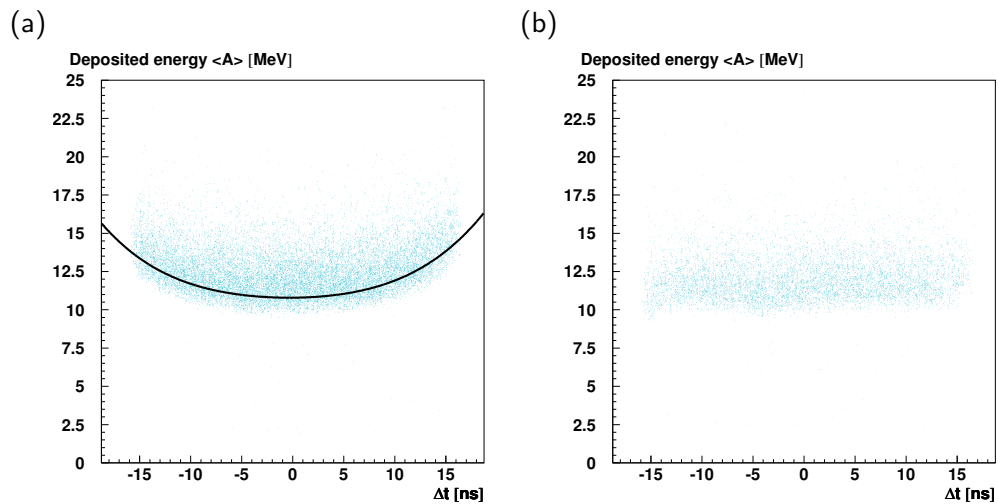


Figure III.15: Remaining amplitude/position dependence (a) before and (b) after correction, plot in case (a) with the polynomial fit. This is done before position calibration by using time difference between left and right end, instead of lengths to be free from position calibration, as described in Sec. III.4.5. These graphs are obtained using cosmic ray muons as source of charged particles.

Due to complex reflections and solid angle effects from which the photomultiplier sees the plastic, an amplitude/position dependence remains. We corrected it using a quadratic fit. The dependence is illustrated in Fig. III.15 (a) and its correction in Fig. III.15 (b). For some 2 m neutron detectors made from two 1 m plastic scintillators glued together, a discontinuity in amplitude is observed, and we correct this effect by adding an offset to the amplitude in one part of the detector.

III.4.3 Time calibration

A calibration of the absolute timing of each rod was made by a run utilizing a thick brass plate placed at the target position producing a large amount of prompt γ -rays and neutrons. For TOF measurement, the arrival time in one

III.4 Neutron detection

neutron detector is defined by:

$$\langle T \rangle = \frac{T_R + T_L}{2} \quad (\text{III.11})$$

where T_R is the time measured for the right PMT and T_L the time measured for the left one, the “start” signal being provided by the F2 plastic. The TOF from F2 to the target must then be subtracted, to obtain the TOF of the neutron from the reaction point, which we supposed in the middle of the target:

$$\text{TOF}_{\text{neutron, Target} \rightarrow \text{Wall}} = \langle T \rangle - \langle \text{TOF} \rangle_{\text{F2} \rightarrow \text{Target}} \quad (\text{III.12})$$

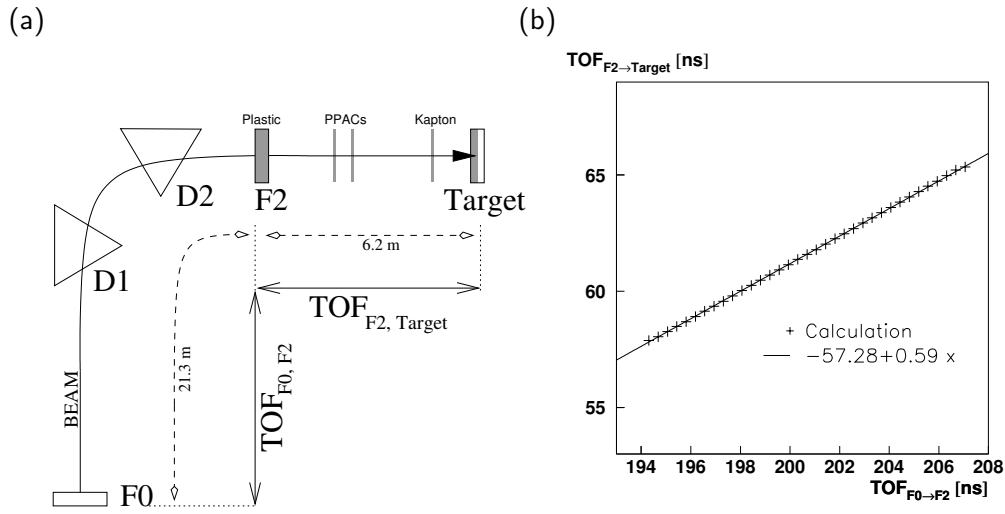


Figure III.16: (a) Definition of $\langle \text{TOF} \rangle_{\text{F2} \rightarrow \text{Target}}$ and $\langle \text{TOF} \rangle_{\text{F0} \rightarrow \text{F2}}$ visualized on a simplified RIPS scheme (b) $\langle \text{TOF} \rangle_{\text{F0} \rightarrow \text{F2}}$ vs $\langle \text{TOF} \rangle_{\text{F2} \rightarrow \text{Target}}$ calculated and fitted by an linear function.

Our setup does not yield a direct measurement of the time difference between F2 and the target. Hence, we extrapolated it from the TOF between the F0 production target to the F2 plastic. For that purpose we calculated the averaged $\langle \text{TOF} \rangle_{\text{F2} \rightarrow \text{Target}}$ value corresponding to a given $\langle \text{TOF} \rangle_{\text{F0} \rightarrow \text{F2}}$ for the ^{26}Ne beam, see Fig. III.16, *i.e.* :

$$\langle \text{TOF} \rangle_{\text{F2} \rightarrow \text{Target}} = f(\langle \text{TOF} \rangle_{^{26}\text{Ne}, \text{F0} \rightarrow \text{F2}}) \quad (\text{III.13})$$

where f is well described by a linear function. The time resolution for $\langle \text{TOF} \rangle_{^{26}\text{Ne}, \text{F0} \rightarrow \text{F2}}$ is $\sigma \sim 0.6$ ns. Since the path length is greater, the resolution on the energy of the incoming nucleus is better than the one obtained by the TOF between F2 and PPACs at F3 as reference (~ 0.8 ns). We took into account the effect of all materials crossed after F2: the F2 plastic, the two PPACs, the kapton window, the air between kapton and target and half of the target, while extracting the TOF between F2 and target.

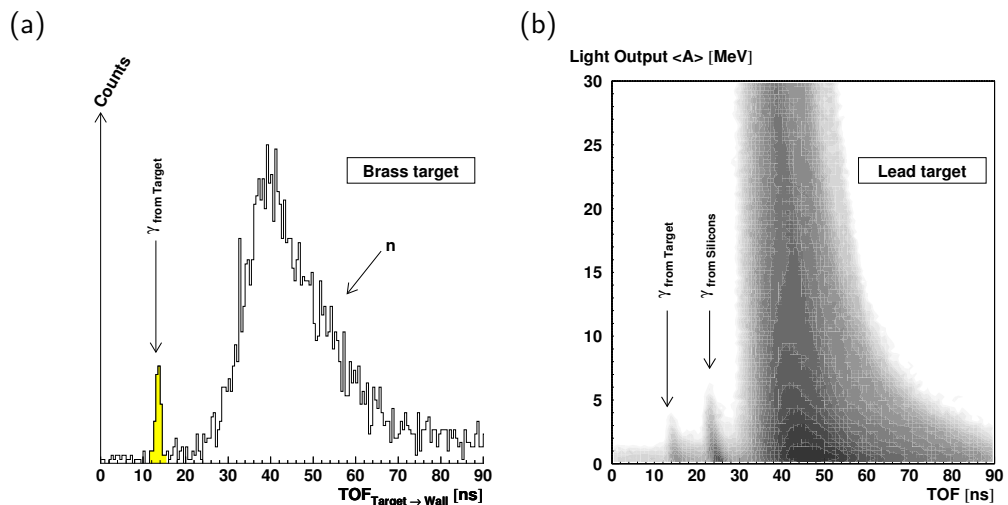


Figure III.17: (a) Example of calibrated absolute TOF spectrum with brass target in one neutron plastic. The first peak (γ) corresponds to gammas emitted from target, the bump (n) to neutrons. (b) Deposited energy vs time-of-flight in neutron detectors for ^{26}Ne impinging onto lead target. The second peak at ~ 23 ns correspond to γ -rays emitted from the silicon setup.

The TOF spectrum obtained with the brass target is displayed in Fig. III.17 (a) and the correlation plot between deposited energy and TOF for the lead target in Fig. III.17 (b). Since the neutron detector wall was placed 3.6 m after the target, the TOF for γ is ~ 12 ns and, with a beam of velocity $\beta \sim c/3$ the TOF for neutron is centered around 40 ns.

The deposited energy of γ -rays in the plastics is typically below 2 MeV whereas neutrons (and other particles)'s energy loss is more widely dis-

III.4 Neutron detection

Particle	Energy [MeV/n]	Time of Flight [ns]		Deviation [%]
		Calculated	Experiment	
protons	70	34.6	34.1 ± 1.1	1.5
protons	50	41.3	$41.4 \pm .75$	0.3
protons	40	46.7	$46.6 \pm .9$	0.2
tritium	87	30.6	30.0 ± 1.2	2.0

Table III.5: Results for proton TOF for a given Long Neutron detector (number 7, center) in the first layer of the wall. Due to the fact that protons essentially stopped in the first layer and their angular spread was rather limited, only few detectors of the first layer were able to be tested. The error presented is $\pm \text{FWHM}/2$ and the deviation is defined by $|E_{\text{th.}} - E_{\text{exp.}}|/E_{\text{th.}}$.

tributed. We confirm this fact by plotting the correlation between deposited energy and TOF, see Fig. III.17 (b). In this figure the average deposited γ -ray energy (at $\text{TOF} \sim 12$ ns) appears to be below 2 MeV. In the following we rejected events which deposited less than 2 MeV in order to disentangle between γ -ray and neutron events. One should note that this figure shows two γ peak: one at 12 ns and one at 23 ns. The first peak is γ -rays emitted from the target whereas the second γ are emitted from the silicon setup. The larger amount of the latter events is due to the trigger condition which required the silicons to be hit.

We checked the time calibration (after slew calibration, see Sec. III.4.4) by using four different energy proton (or tritium) secondary beams (70, 50, 40 MeV for protons and 87 MeV/n for tritium). Only a few central detectors were hit by these direct beams. As can be read in Table III.5, a good agreement is found between the calculated TOF and the experimental one extracted after calibration. However, the resolution is not good because protons (or tritium) cross and interact with many materials before arriving into the neutron wall.

III.4.4 Slew (walk) correction

Description

For timing signals, leading edge (LE) discriminators were used. It produces a strong time/amplitude dependence termed *walk* or *slew*. This effect is due to the fact that the time signal occurs when the amplitude exceeds the threshold. However, as illustrated in Fig. III.18 (a), the time to reach the threshold depends on the amplitude of the signal. For an improved resolution of TOF or position measurement, this effect must be corrected for.

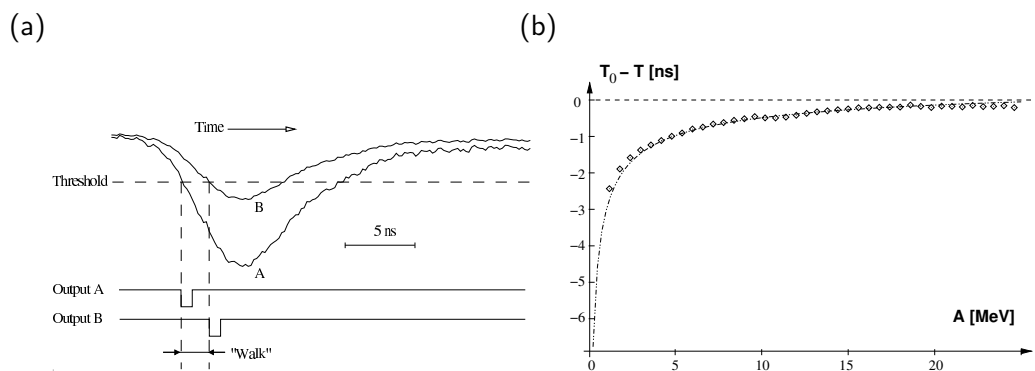


Figure III.18: (a) Illustration of the walk effect, using real signal from 2 m neutron plastic detector (presentation strongly inspired from [Leo 94]) (b) LE discriminator timing minus CFD timing we suppose without slew effect. The dashed line is obtained by fitting the data with the function $\Delta T = \Delta T_0 - K/\sqrt{E}$

For some detectors, we redirected the timing signal both into LE and a constant fraction discriminator (CFD). By supposing that the CFD does not create any slew, the dependence with the energy of the time difference $T_{LE} - T_{CFD}$ measures the slew effect for the LE. The result is displayed in Fig. III.18 (b) and one can see that the time/amplitude dependence can be well approximated by $T = T^0 - K/\sqrt{A}$, where A is the light output at one end (see Fig. III.18 (b)). In the following, K will be referred to as *slew coefficient*. The rise time of the plastic-scintillator signal is ~ 6 ns and therefore the time shift from the slew effect cannot be more than 6 ns.

III.4 Neutron detection

The slew is corrected for each rod's end according to the above formulas. We eliminated the time/amplitude dependence due to attenuation in the plastic scintillator by selecting events from the center of the plastic rod, thus obtaining similar light attenuation at both ends.

Finally, timing for one neutron detector is defined as:

$$\langle T \rangle = \frac{1}{2} \left(T_R + T_L - \frac{K_R}{\sqrt{A_R}} - \frac{K_L}{\sqrt{A_L}} \right), \quad (\text{III.14})$$

where R and L denotes the right and the left end respectively.

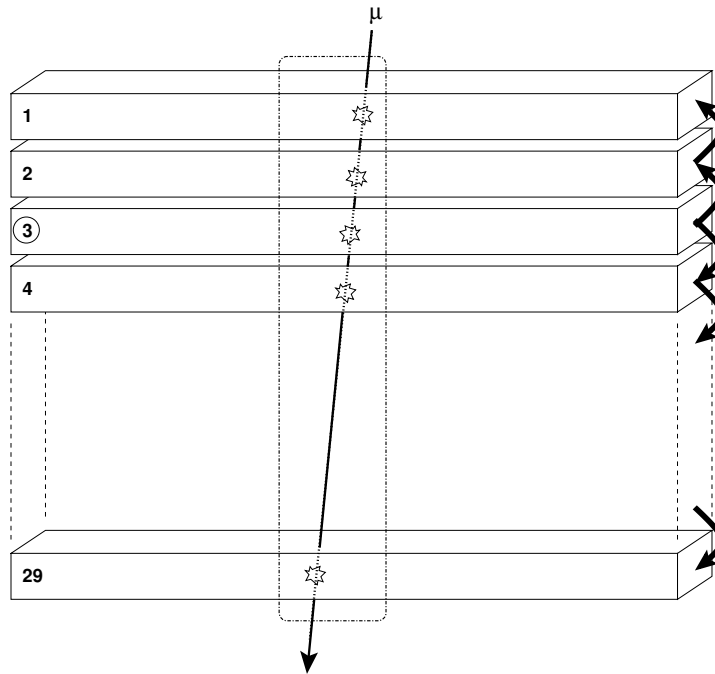


Figure III.19: Schematic explanation of propagation method through plastic scintillators. In this case, we start from detector 3 and propagate to both up and down, while selecting the center of the scintillators (dash-dot line area) to obtain a similar light attenuation at both ends.

The slew coefficients K have been determined in a procedure detailed in the next section.

Slew correction procedure

We considered two consecutive detectors in one layer: one for correction (\mathcal{C}) and one for reference (\mathcal{R}). We define:

$$\delta T_S(A_S^{\mathcal{C}}) = T_S^{\mathcal{C}}(A_S^{\mathcal{C}}) - T_S^{\mathcal{R}}(A_S^{\mathcal{C}}); S : \text{Left, Right} \quad (\text{III.15})$$

$$\delta T(\langle A^{\mathcal{C}} \rangle) = (\delta T_L(\langle A^{\mathcal{C}} \rangle) + \delta T_R(\langle A^{\mathcal{C}} \rangle)) / 2. \quad (\text{III.16})$$

We fitted the two dimensional δT_S vs $A_S^{\mathcal{C}}$ using the slew function, and obtained the slew coefficients.

We started from the top detector of a layer, called 1. By fitting, we obtained slew coefficients for both sides of the next rod below, called 2. Since the reference detector was not corrected yet, these coefficients included the slew effect from both the reference and corrected detectors. In the case of an \mathcal{R} detector with a high slew, coefficients of the \mathcal{C} detector can even be negative and the time for low-energy events appears less than that for high energy ones. We continued to propagate the correction, using 2 as a reference for 3, then 3 for 4, up to 28 as a reference for 29.

When the last detector had been fitted, we restarted the same propagation algorithm, from detector 2. This last detector is used as a reference for both 1 and 3, then 3 for 4 up to 28 as a reference for 29. We started again from 3 as a reference for 4 and 2, then 4 for 5, 2 for 1, and so on, see illustration in Fig. III.19 (b).

The coefficients obtained after using all the detectors as starting points, *i.e.*, after 29 resets, were averaged to give the 29 ($\times 2$ sides) slew coefficients. We validated the correction by confirming that neither δT_S nor δT depends on $A_S^{\mathcal{C}}$ or $\langle A^{\mathcal{C}} \rangle$, respectively, for all detectors. The extracted coefficients were of the order of 4 ns.MeV $^{\frac{1}{2}}$.

With the method using cosmic rays, a typical time resolution of 850 ps (FWHM) was for γ -rays. The same detectors, before correction, showed a average resolution of 2 ns. The ‘‘direct’’ correction using energetic neutrons, emitted from the ${}^7\text{Li}(p,n){}^7\text{Be}$ reaction, provides however a better correction and the resolution achieved is 700 ps [Fukuda 04]. However our method does

III.4 Neutron detection

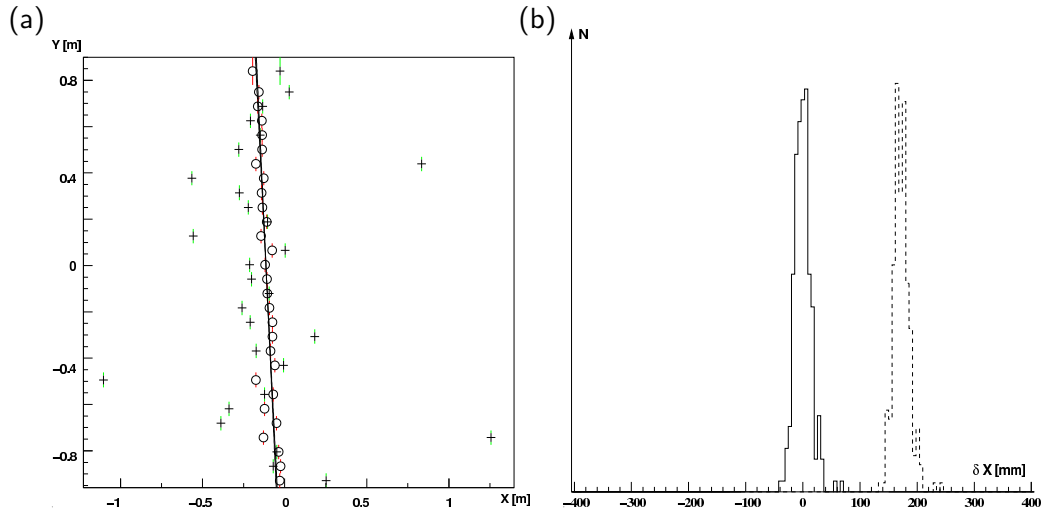


Figure III.20: (a) Example of muon's tracking before position correction (+) and after correction (o), plotted with a fitted track. (b) Example of position difference between the track and the real and non corrected hit position. After position calibration, this distribution also gives the error on the trajectory of the muons, which is $\sigma \approx 15$ mm.

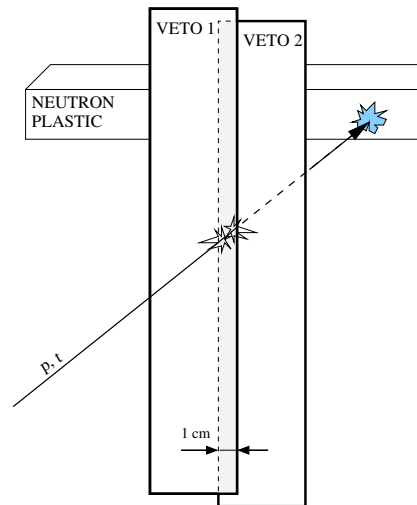
not require additional beam time.

III.4.5 Position calibration

The time difference $\Delta T = T_L - T_R$ provides the horizontal position. The maximum value of ΔT , ΔT_{\max} , corresponds to photons that travel the entire scintillator length L . We measured $\Delta T_{\max} \approx 30$ ns for $L = 2.1$ m and $\Delta T_{\max} \approx 18$ ns for $L = 1.1$ m. Then, $L/\Delta T_{\max}$ provides the mm \leftrightarrow ns correspondence.

For the relative position calibration between the detectors within one layer, we selected the highest multiplicity events in the cosmic ray measurement. For one event, 29 pairs of hit coordinates $(X_i, Y_i)_{i=1,29}$ were fitted to provide an equation that describes the muon's trajectory: $X = \alpha Y + \beta$ as one can see on Fig. III.20 (a). For each detector we obtained the dis-

Figure III.21: Illustration of the method of improvement of the absolute position calibration using vertical plastic detectors (vetoes) placed in front of the neutron wall. We required the incoming charged particle to hit to overlap vetoes before hitting the neutron plastic rod behind.



tribution of differences between the fitted trajectory and real coordinates, $\Delta_i X = X_i - (\alpha Y_i + \beta)$, which gives the individual horizontal position shift (for illustration see Fig. III.20 (a)). The overall horizontal position resolution for muons was found to be 2 cm (FWHM).

The absolute position of the first layer is obtained by utilizing a proton beam run. Protons stop in the first layer at a well-known position determined using the veto detectors placed in front of the neutron wall. The width of these vetoes is of 10 cm but they overlap over less than 1 cm which as illustrated in Fig. III.21. By taking only data in coincidence with 2 overlapped vetoes, we improved the position resolution. The three other layers are aligned on the first one by relying on the geometrical alignment of each edge at each side. This method is tested using the 87 MeV/n tritium run which stop in the second layer with a good result.

III.4.6 Efficiency and Angular acceptance

Efficiency

According to previous analysis [Fukuda 04] using the same plastic neutron detectors, the efficiency is well reproduced at our intermediate energies by code CECIL [Cecil 79].

III.4 Neutron detection

The code CECIL is a Monte-Carlo simulation of neutron propagation in plastic, which includes the $C(n, \gamma)$, $C(n, \alpha)$, $C(n, 3\alpha)$, $C(n, np)$, $C(n, 2n)$ and $H(n, p)$ reactions in their inelastic channels as well as in their elastic channels. The light response is taken into account. The finite size of the detector and the possible escaping charged particles are taken into account for the energy loss. The results presented in Fig. III.22 are obtained by supposing a neutron incident in the direction perpendicular to the center of the front [2.1 m×6 cm] face of a 6 cm thick parallelepipedic rod.

For experimental verifications, a ${}^7\text{Li}(p,n){}^7\text{Be}(\text{g.s.}+0.43 \text{ MeV})$ reaction [Taddeucci 90] was performed with proton of 70 MeV impinging on lithium target to produce neutrons with an energy of about 65 MeV. The neutron was identified by its time-of-flight. The accuracy on the efficiency for long neutron detectors is of 6%. The light-output threshold dependence of the efficiency as obtained in the experiment is comparable with simulation using the code CECIL, see Fig. III.22 (a).

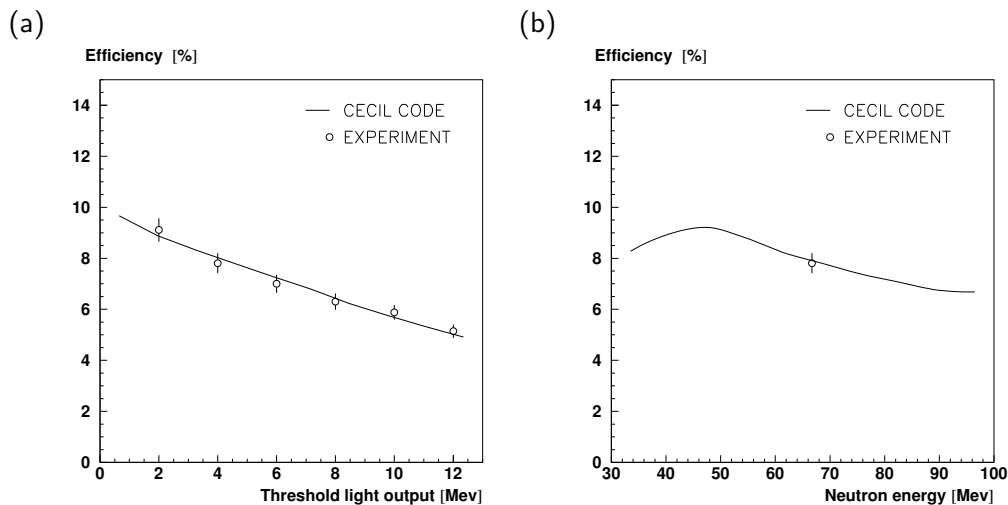


Figure III.22: (a) Neutron efficiency function of the light output threshold in LN plastic, as calculated by CECIL and as given by the experiment. (b) Neutron efficiency in LN plastics function of the neutron kinetic energy, as calculated by CECIL and as given by the experiment.

The same code is used to extrapolate the dependence of the efficiency on the energy of the detected neutron, see Fig. III.22 (b). The efficiency calculated has an average of $8.0\% \pm 0.8\%$ in the 30 MeV to 100 MeV neutron incident energy range.

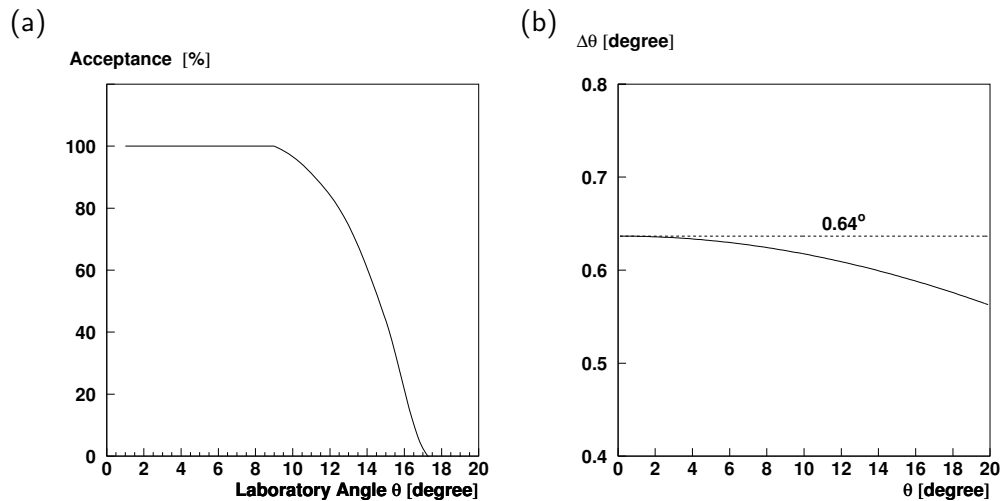


Figure III.23: (a) Neutron wall angular acceptance function of the angle in degrees (b) Neutron angular resolution (FWHM) function of the angle in degrees, with its minimum at 0.64° .

Angular acceptance and angular resolution

The geometrical acceptance is deduced using a Monte-Carlo simulation. Fig. III.23 (a) shows its angular dependence in the laboratory frame. This angle is defined between an hypothetical incident beam passing through the center of the target and the center of the neutron wall front face, and a neutron coming from the center of the target into the first layer of the neutron wall. The same definition of angle is used for estimating the angular resolution (FWHM). The position resolution of 4 cm correspond to an average angular resolution of 0.6° . The small angular dependence is shown in Fig. III.23 (b).

Chapter IV

Results

In this chapter, we present the results that we have obtained on the elastic and the inelastic scattering of the ^{26}Ne nucleus impinging on lead and aluminum targets.

The elastic scattering data were analyzed mainly for two purposes:

- i) to check the validity of the optical potentials to be used in the analysis of the inelastic scattering.
- ii) to confirm the normalization of the data as well as the geometrical efficiency extracted from the simulations.

In the second step, the excitation of the first 2^+ state in ^{26}Ne is studied by using two methods and the comparison with previous results is presented.

Finally, the inelastic excitations induced by aluminum and lead targets above the neutron emission threshold are investigated. The method to reconstruct the ^{26}Ne excitation energy in the $^{25}\text{Ne}+n$ decay channel is presented and applied for both targets. In the last part, the extracted strength is compared with the predictions using the most advanced microscopic models.

IV.1 Elastic scattering of ^{26}Ne

IV.1.1 Optical potential

In the elastic scattering, the projectile direction and/or state of polarization is changed during the interaction with the target, but without loss of kinetic energy. The Schrodinger equation can be written, in the center of mass system (CM) of the two nuclei:

$$\left(-\frac{\hbar^2}{2\mu}\nabla_r^2 + U(\vec{r})\right)\psi(\vec{r}) = E\psi(\vec{r}) \quad (\text{IV.1})$$

where $\psi(\vec{r})$ is the total wave function of the system, \vec{r} the relative position of the two particles, $U(\vec{r})$ the central potential. By analogy with optics, we can describe its asymptotic wave function, far from the reaction point, as the sum of an incident plane wave and an outgoing (scattered) spherical wave:

$$\psi(\vec{r}) \xrightarrow{r \rightarrow \infty} e^{i\vec{k}\vec{r}} + f(\theta, \phi) \frac{e^{ikr}}{r} \quad \text{with } r = |\vec{r}|. \quad (\text{IV.2})$$

Therefore, all the scattering information are contained in the scattering amplitude $f(\theta, \phi)$. The angular distribution is expressed by the differential cross section:

$$\frac{d\sigma}{d\Omega} = |f(\theta, \phi)|^2. \quad (\text{IV.3})$$

The optical model supposes that the interaction between an incident particle and a nucleus of mass number A is well described by an average nucleon-nucleus interaction written as a single absorbing central potential well, the optical potential $U(r) = V(r) + iW(r)$. $V(r)$ and $W(r)$ are the real and the imaginary potential: $V(r)$ corresponds to a simple reflection of the incoming wave whereas $W(r)$ is introduced to reproduce the possible absorptions before reemission, of this wave. Its expression is often simplified by a parametrization of a Woods Saxon form $\mathfrak{F}(x)$:

$$U(r) = -(V + iW) \mathfrak{F}\left(\frac{r - R}{a}\right) \quad ; \quad \mathfrak{F}(x) = \frac{1}{1 + \exp(x)} \quad (\text{IV.4})$$

IV.1 Elastic scattering of ^{26}Ne

with V, W real and positive, A the mass number of the nucleus, $R = r_0 A^{1/3}$ its radius (r_0 is call reduced radius) and a the diffuseness. To describe the data satisfactorily, a spin-orbit term (SO) and a Coulomb potential (C) are added to the real part (\Re) of the potential, and a surface term (D) to the imaginary part (\Im), which gives:

$$\Re(U(r)) = V(r) = V_C(r) - V\mathfrak{F}(x_V) + V_{SO} \left(\frac{\hbar}{m_\pi c} \right)^2 \frac{1}{r} \frac{\partial \mathfrak{F}(x_{SO})}{\partial r} \vec{L} \cdot \vec{\sigma}, \quad (\text{IV.5})$$

$$\Im(U(r)) = W(r) = -W\mathfrak{F}(x_W) - 4W_D \frac{\partial \mathfrak{F}(x_D)}{\partial r}, \quad (\text{IV.6})$$

where $x_\alpha = (r - R_\alpha)/a_\alpha$, m_π is the mass of pion, $\vec{L} \cdot \vec{\sigma}$ the scalar product between the spin of the incoming particle and the angular momentum, and $V_C(r)$ the Coulomb potential due to a pointless charge $Z_p e$ interacting with an uniformly charged ($Z_t e$) sphere of radius R_C :

$$V_C(r) = \begin{cases} \frac{Z_p Z_t e^2}{r} & \text{for } r \geq R_C \\ \frac{Z_p Z_t e^2}{2R_C} \left(3 - \frac{r^2}{R_C^2} \right) & \text{for } r < R_C \end{cases}. \quad (\text{IV.7})$$

One frequently assumes $R_D = R_W$ and $a_D = a_W$.

In heavy ion scattering, one should take into account the size of the two nuclei reacting, [Satchler 83] proposes:

$$R_i \approx r_i (A_t^{1/3} + A_p^{1/3}) \quad ; \quad R_C \approx R_{C,t} + R_{C,p} \quad (\text{IV.8})$$

as expressions for nuclear and Coulomb radius respectively, where the t and p in index stand for *target* and *projectile* respectively.

IV.1.2 Extraction of experimental angular distributions

Method

Elastic scattering data were obtained from downscaled beam events (see Chapter II) by selecting ^{26}Ne scattered particles in the silicon hodoscope. The scattering angle of ^{26}Ne in the laboratory frame θ_{lab} is deduced *via* the position measured in the silicon strip detectors, corrected from the incoming

beam angle. We suppose that the reaction occurs in the middle of the target and at the position extrapolated using the PPAC information as explained in Sec. III.1.2, hence :

$$\cos \theta_{\text{lab}} = \frac{\vec{p}_i}{|\vec{p}_i|} \cdot \frac{\vec{p}_f}{|\vec{p}_f|} \quad (\text{IV.9})$$

with \vec{p}_i and \vec{p}_f are incident and outgoing momenta*. We express the angle in the center of mass system of the incoming and target nuclei using the inverse of formula Eq. C.28:

$$\tan(\theta_{\text{CM}}) = \frac{\Gamma \tan(\theta_{\text{lab}}) \left(\sqrt{1 + \tan(\theta_{\text{lab}})^2 \Gamma^2} - \tan(\theta_{\text{lab}})^2 \Gamma^2 \chi^2 - \chi \right)}{\tan(\theta_{\text{lab}})^2 \Gamma^2 \chi + \sqrt{1 + \tan(\theta_{\text{lab}})^2 \Gamma^2} - \tan(\theta_{\text{lab}})^2 \Gamma^2 \chi^2}, \quad (\text{IV.10})$$

where χ is the ratio between the velocity of the CM and the velocity of the particle of interest as defined in Eq. C.27 for the ^{26}Ne . From the θ_{CM} distribution we deduced the angular distribution:

$$\frac{d\sigma}{d\Omega}(\theta_{\text{CM}}) [mb/sr] = \frac{N_{\text{scat}}(\theta_{\text{CM}})}{N_{\text{inc}} N_{\text{target}} \sin(\theta_{\text{CM}}) \Delta\theta_{\text{CM}} 2\pi \epsilon(\theta_{\text{CM}})} \quad (\text{IV.11})$$

where N_{scat} is the number of nuclei scattered, N_{inc} is the number of incident nuclei in the beam, N_{target} is the target thickness in mb^{-1} , $\Delta\theta_{\text{CM}}$ the histogram binning size and ϵ corresponds to the angular acceptance of the silicon detectors illustrated in Fig. III.13 (b).

To reconstruct the elastic distribution we subtract the inelastic scattering spectrum corresponding to ^{26}Ne in coincidence with γ -rays, as described in Sec. IV.2, from the inclusive spectrum. Events close to the center of the silicon hodoscope, corresponding to the direct beam, were rejected. The theoretical distribution is obtained by Monte-Carlo simulation using Geant 3 with an angular distribution calculated using ECIS 97 [Raynal 97] as input. The simulation included the real beam events as obtained from the PPAC data for downscaled beam events, taking into account all materials located after the vacuum pipe and the exact geometry of silicons.

*Note that it is not necessary to calculate the full momentum since $\vec{p}/|\vec{p}|$ is simply the direction.

IV.1 Elastic scattering of ^{26}Ne

Results

	V	W	r	a	r_c	a_c
	[MeV]	[MeV]	[fm]	[fm]	[fm]	[fm]
(a) $^{20}\text{Ne}+^{208}\text{Pb}$	63.2	32.4	1.168	0.637	1.2	0.559
(b) $^{26}\text{Ne}+^{27}\text{Al}$	67.0	35.0	1.080	0.750	1.2	0.556

Table IV.1: Optical parameters used in this analysis: (a) is extracted from [Suomijärvi 89] (b) Empirically deduced from various references (see text). Note that we have equality between real and imaginary part for the reduced radius r and the diffusiveness a .

The elastic scattering angular distribution of ^{26}Ne onto $^{\text{nat}}\text{Pb}$ at 55 MeV/n is shown in Fig. IV.1 (a). It is satisfactorily reproduced by using the experimental $^{20}\text{Ne}+^{208}\text{Pb}$ optical potential parameters at 40 MeV/n [Suomijärvi 89] listed in Table IV.1 (a). These potential parameters are hence considered valid for our further analysis.

In the case of elastic scattering on aluminum target, we tested different published potential parameters:

$$^{20}\text{Ne}(40 \text{ MeV/n})+^{90}\text{Zr} \text{ [Suomijärvi 89]}$$

$$^{12}\text{C}(84 \text{ MeV/n})+^{12}\text{C} \text{ [Buenerd 84]}$$

$$^{16}\text{O}(94 \text{ MeV/n})+^{12}\text{C}, ^{28}\text{Si} \text{ or } ^{40}\text{Ca} \text{ [Roussel-Chomaz 88]}$$

$$^{16}\text{O}(30 \text{ MeV/n})+^{16}\text{O} \text{ [Khoa 95]}.$$

Since none of them gave acceptable results for our case, we used them as starting point to deduce empirically the parameters listed in Table IV.1 (b).

The hypothesis made to extrapolate our parameters are:

- We considered that the reduced radius r and the nuclear diffusiveness a only depends linearly on the sum of the two nuclei radius of interest, *i.e.* $r, a \propto A_p^{1/3} + A_t^{1/3}$.
- We use the Coulomb parameters r_c and a_c from $^{20}\text{Ne}(40 \text{ MeV/n})+^{90}\text{Zr}$.

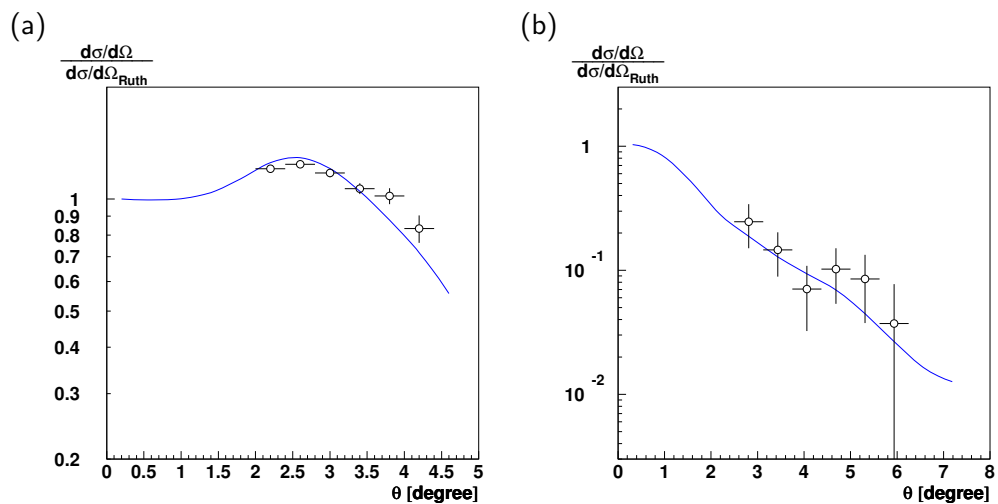


Figure IV.1: Experimental $\frac{d\sigma}{d\Omega} / \frac{d\sigma}{d\Omega_{\text{Ruth}}}$ ratio, in the center-of-mass system, for (a) lead target (b) aluminum target (open circles) compared to ECIS 97 calculation (solid lines).

- Following [Broglia 91], we suppose that the real volume part V of the potential depth depends linearly on the incident energy.
- The imaginary part of the potential reproduces the possible absorption and its dependence on the other parameters is more complicated. This is confirmed by the experimental values of the volume potential W . Checking that the other coefficients are acceptable by looking at the effect of their variation on the angular distribution, and knowing the deformation parameters from the analysis on lead target, we adjusted W to fit the elastic scattering as well as the $18 \pm 3(\text{stat})$ mb *total* cross section reaction for the first 2^+ state of ^{26}Ne obtained *via* the number of gamma-rays (see Sec. IV.2.2).

The result using these parameters is plotted in Fig. IV.1 (b) and we observe a good agreement with the data. It hence validates the use of these parameters in our case.

IV.2 Inelastic scattering of ^{26}Ne below the neutron emission threshold

By selecting the 2018 keV gamma decay from the first 2^+ to the ground state in coincidence with ^{26}Ne in silicon telescopes, we built the angular distribution for the inelastic scattering excitation to the 2^+ state. By fitting it using the ECIS 97 code we extracted its $B(E2; 0^+ \rightarrow 2_1^+)$ value. For comparison, this $B(E2; 2_1^+)$ was also deduced from the γ -decay of the 2_1^+ state measured with the photon detector array, using the virtual photon method.

IV.2.1 The Distorted Wave Born Approximation

The distorted wave Born approximation (DWBA) is the most frequently used method to analyze inelastic scattering data. The scattering potential $U(r)$ is described by the elastic scattering $U_0(r)$ potential to which we add a perturbation ΔU , causing the inelastic scattering. The transition matrix element from the initial state i to a given final state f is written:

$$T_{fi} = \int \chi_f^{(-)}(\vec{k}, \vec{r}) \langle f | \Delta U(r) | i \rangle \chi_i^{(+)}(\vec{k}, \vec{r}) d\vec{r}, \quad (\text{IV.12})$$

where $\chi^{(+)}$, $\chi^{(-)}$ are the solutions of the Schrödinger equations for the elastic scattering with outgoing and incoming boundary conditions respectively. The differential cross section for inelastic excitation in the center of mass of the two scattered particles is written:

$$\frac{d\sigma}{d\Omega} = \left(\frac{\mu}{2\pi\hbar^2} \right)^2 \frac{k_f}{k_i} |T_{fi}|^2, \quad (\text{IV.13})$$

where μ is the reduced mass of the system and k_i , k_f the initial and final momentum respectively.

If the excitation sustained deforms the nucleus, and within the framework of the dynamical theory of the collective motion of a liquid drop, this deformation can be expressed in terms of variation of the radius, which is

function of the azimuthal and polar angles, with a value around equilibrium radius R_0 i.e. $R(\theta, \phi) = R_0 + \delta R(\theta, \phi)$. In the deformed optical model, it is assumed that the optical potential follows the shape of the density of the nucleus, by expanding it about R_0 :

$$U(r, R) = U(r, R_0) + \left(\frac{\delta U}{\delta R} \right)_{R_0} (R - R_0) + \dots \quad (\text{IV.14})$$

which leads by identification at the first order to $\Delta U = \frac{\partial U(r, R_0)}{\partial R} (R - R_0)$.

The nuclear radius can be developed onto the spherical harmonics basis:

$$R = R_0 \left[1 + \sum_{\lambda\mu} \alpha_\lambda^\mu Y_\lambda^\mu(\theta, \phi) \right], \quad (\text{IV.15})$$

where α_λ^μ is proportional to the deformation parameter β_λ^μ . Inserting Eq. IV.15 into Eq. IV.14 leads to

$$\Delta U = R_0 \left(\frac{\delta U}{\delta R} \right)_{R_0} \sum_{\lambda\mu} \alpha_\lambda^\mu Y_\lambda^\mu(\theta, \phi) \quad (\text{IV.16})$$

The elastic scattering potential as written in Eq. IV.5 is composed of a nuclear term and a Coulomb term. For a given multipolarity λ , in the hypothesis we separate the hadronic deformation length δ_λ^N from the charge deformation length δ_λ^C , the nuclear part of the optical potential will be only affected by the nuclear deformation β_λ^N while the Coulomb potential will be affected by the charge deformation β_λ^C . Note that these different lengths and deformations are often related together *via* :

$$(\delta_\lambda^N = \beta_\lambda^N R_N) = (\delta_\lambda^C = \beta_\lambda^C R_C) = \beta_\lambda R \quad (\text{IV.17})$$

where R_N , R_C and $R = 1.115A^{1/3} - 0.53A^{-1/3}$ are respectively: the nuclear, the Coulomb and the half density radius .

For a $0^+ \rightarrow 2^+$ transition in an even-even nucleus, the collective deformation model gives the following relation between β_2^C and its corresponding $B(E2)$:

$$B(E2; 0^+ \rightarrow 2^+) = \left(\frac{3}{4\pi} Z_p e R_C^2 \beta_2^C \right)^2 \quad (\text{IV.18})$$

IV.2 Inelastic scattering below the neutron emission threshold

where R_C is the Coulomb radius written $1.2 A_p^{1/3}$ fm.

IV.2.2 $B(E2)$ calculation

^{26}Ne gamma decay analysis

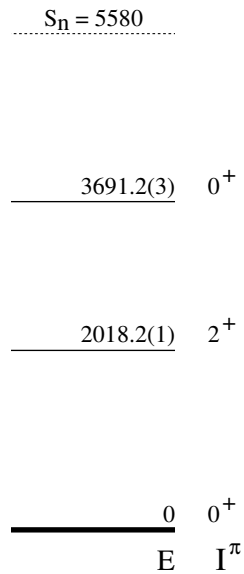


Figure IV.2: Adopted levels and gammas in ^{26}Ne

The adopted gamma transitions and levels for ^{26}Ne are given in Fig. IV.2. The Doppler corrected energy spectrum for a γ multiplicity strictly equal to 1, in coincidence with a ^{26}Ne in the silicon telescope, is presented in Fig. IV.3. The spectrum obtained with the empty target has been subtracted from both the lead and the aluminum target spectra after normalization to the same number of incident particles. The ^{26}Ne 2_1^+ state at 2022 ± 62 keV is clearly observed. The peak at 4130 ± 140 keV indicated by the arrow \downarrow is present in the non-Doppler corrected distribution, in lead, aluminum and empty target spectra with a narrow width so we conclude that it does not come from the interaction with the target.

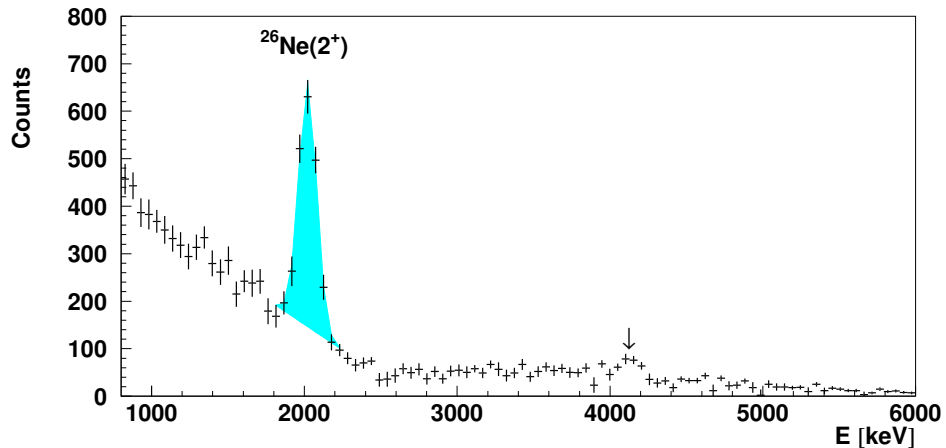


Figure IV.3: Doppler corrected γ -ray energy distribution in coincidence with ^{26}Ne , for lead target. The shaded area corresponds to the integrated number of gamma taken as really emitted from ^{26}Ne . The arrow \downarrow corresponds to γ -rays identified as emitted from the background (see text).

In order to investigate the feeding of the 2_1^+ state through the higher 0_2^+ excited state decay, we examined the gamma-gamma correlations. In a first step we plot the two dimensional energy spectrum of γ_2 versus energy of γ_1 , where γ_1 labeled the γ with higher energy, as shown in Fig. IV.4 (a). A correlation is clearly seen between ~ 2 MeV and ~ 1.7 MeV gammas. We assign the peak at 1683 ± 60 keV (Fig. IV.4 (b)) to the cascade from the adopted $3691.2(3)$ keV 0_2^+ to the $2018.2(1)$ keV 2_1^+ state. We estimated the ratio of the intensities of the 1667 keV/ 2018.2 keV lines to be $10 \pm 5\%$ for the reaction on lead and $20 \pm 5\%$ for aluminum target. In the following, we will take into account this contribution to the 2 MeV γ -ray cross section and angular distribution.

IV.2 Inelastic scattering below the neutron emission threshold

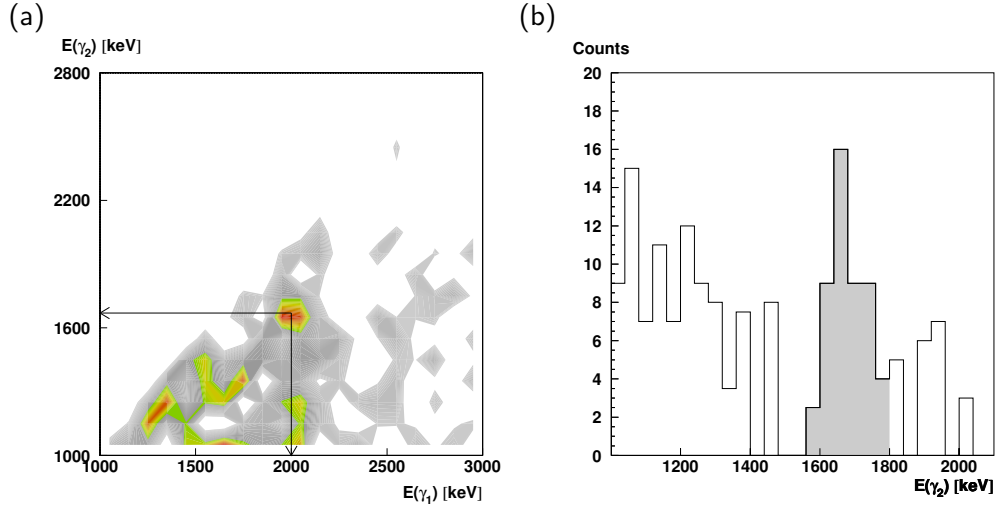


Figure IV.4: Analysis with gamma multiplicity strictly equals to 2: (a) γ_2 energy vs γ_1 energy where $E(\gamma_1) > E(\gamma_2)$, see details in Sec. IV.3.2. (b) Energy distribution of γ_2 in coincidence with $E(\gamma_1) \in [1950 : 2090]$ keV.

B(E2) extraction using angular distributions

The differential cross section for the inelastic scattering of the first 2^+ excited state in ^{26}Ne is obtained by building the angular distribution of ^{26}Ne in the silicon detectors in coincidence with the 2020 ± 150 keV gamma-rays. The peak in Fig. IV.5 (a) is superimposed onto a continuum, which can be well reproduced by means of an exponential fit normalized to the high energy part of the γ -rays spectrum [Yamada 04]. Here, the background is removed by subtracting from the angular distribution gated by the 2020 γ peak the angular distribution gated on the adjacent area (centered at 2320 keV) with the same ± 150 keV width and normalized by a 1.25 factor. This factor is obtained as the ratio of the areas delimited by the 2020 ± 150 and $(2020 + 300) \pm 150$ keV γ -rays in the exponential background previously discussed, see Fig. IV.5 (a).

The resulting angular distributions are presented in Fig. IV.5 (b) for the lead target. By using ECIS 97 code with the optical parameters of ^{20}Ne at

40 MeV/n impinging on ^{208}Pb [Suomijärvi 89] and under the hypothesis that the nuclear ($\delta_N^{L=2}$) and the Coulomb ($\delta_C^{L=2}$) deformation lengths are equal, we deduced a $B(E2)$ of $87 \pm 13 \text{ e}^2\text{fm}^4$ which reproduces the integrated excited γ -decay cross section of 68(8) mb (see below). The corresponding calculated angular distribution for the inelastically scattered ^{26}Ne well reproduce the experimental distribution. Note that the pure Coulomb assumption (dashed line) does not well reproduce the data.

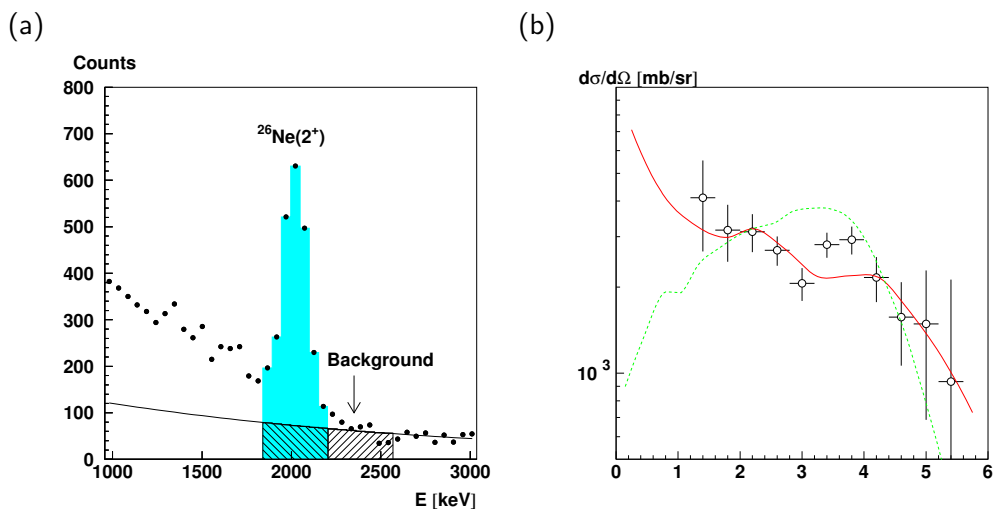


Figure IV.5: (a) Experimental ^{26}Ne energy gamma distribution (\bullet) with lead target. Solid line is an exponential fit to the background. Dashed \square area is gammas taken as equivalent background for the 2^+ γ -ray energy distribution (dashed \square area). (b) Angular distribution for the first 2^+ excited state of ^{26}Ne on lead target compared to ECIS 97 calculation: in solid line the calculated angular distribution with $\beta_N = 0.319$ and $\beta_C = 0.310$, in dashed line the calculated result with pure Coulomb excitation ($\beta_N = 0.0, \beta_C = 0.466.$). Both calculations give an integrated cross section of 68 mb.

The distribution obtained for the aluminum target, using the same method, with the above deformation parameters and the optical potential described in Sec. IV.1 gives a good agreement with the data as can be seen in Fig. IV.6 (b).

IV.2 Inelastic scattering below the neutron emission threshold

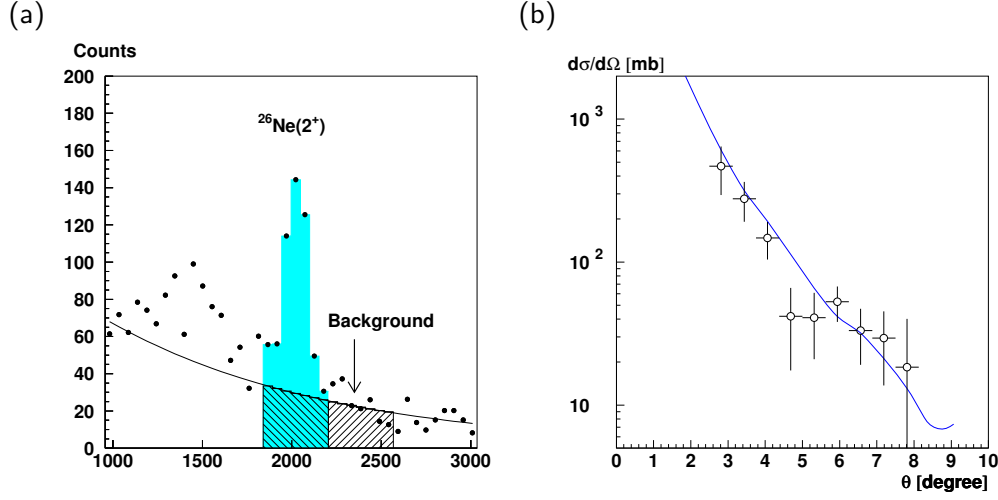


Figure IV.6: (a) Experimental ^{26}Ne energy gamma distribution (\bullet), for aluminum target. Solid line is an exponential fit of the background. Dashed \square area is gammas taken as equivalent background for the 2^+ γ -ray energy distribution (dashed \square area). (b) Angular distribution for the first 2^+ excited state of ^{26}Ne on aluminum target compared to ECIS 97 calculation.

B(E2) extraction using the equivalent photon method

Our result using angular distribution is now compared to the previous result and method using the equivalent photon method.

Theoretical considerations The reduced transition probability for electromagnetic transitions is defined by:

$$B(\pi\lambda; I_i \rightarrow I_f) = \sum_{\mu M_f} |\langle J_f M_f | \mathcal{M}(\pi\lambda\mu) | J_i M_i \rangle|^2 \quad (\text{IV.19})$$

$$= \frac{1}{2J_i + 1} |\langle J_f || \mathcal{M}(\pi\lambda) || J_i \rangle|^2 \quad (\text{IV.20})$$

where $\mathcal{M}(\pi\lambda\mu)$ is the multipole operator for electromagnetic transitions and $|J_i\rangle$ ($|J_f\rangle$) is the initial (respectively final) state of angular momentum J . According to Winther and Alder [Winther 79], it is directly related to exci-

tation cross section by:

$$\sigma_{i \rightarrow f} = \left(\frac{Z_p e^2}{\hbar c} \right)^2 \sum_{\mu M_f} k^{2(\lambda-1)} \frac{B(\pi\lambda; I_i \rightarrow I_f)}{e^2} \left| G_{\pi\lambda\mu} \left(\frac{c}{v} \right) \right|^2 g_\mu(\xi(b_{min})) \quad (\text{IV.21})$$

where $G_{\pi\lambda\mu}(x)$ is a function of the associated Legendre polynomials $P_\lambda^\mu(x)$ and $g_\mu(x)$ is function of the modified Bessel function $K_\mu(x)$. Their expressions in the electric transition case ($\pi = E$) are:

$$G_{E\lambda\mu}(x) = i^{\lambda+\mu} \frac{\sqrt{16\pi}}{\lambda(2\lambda+1)!!} \left(\frac{(\lambda-\mu)!}{(\lambda+\mu)!} \right)^{\frac{1}{2}} (x^2-1)^{-\frac{1}{2}} \quad (\text{IV.22})$$

$$\times \left(\frac{(\lambda+1)(\lambda+\mu)}{2\lambda+1} P_{\lambda-1}^\mu(x) - \frac{\lambda(\lambda-\mu+1)}{2\lambda+1} P_{\lambda+1}^\mu(x) \right)$$

$$g_\mu(x) = \pi x^2 \left(|K_{\mu+1}(x)|^2 - |K_\mu(x)|^2 - \frac{2\mu}{x} K_{\mu+1}(x) K_\mu(x) \right) \quad (\text{IV.23})$$

In Eq. IV.21 $g_\mu(x)$ is function of the adiabaticity parameter $\xi(b)$, where b is the impact parameter. In the non-relativistic limit ($v/c \ll 1$), it is given by the relation:

$$\xi(b) = \frac{\omega_{fi}}{v\gamma} \left(b + \frac{\pi Z_p Z_t e^2}{2 M v^2 \gamma} \right) \quad (\text{IV.24})$$

where $M_{[MeV]} \approx 981 \frac{A_p A_t}{A_p + A_t}$ is the reduced mass of the two nuclei of charge and mass (Z_p, A_p) and (Z_t, A_t) , v the velocity and γ the Lorentz factor. The energy of the transition is expressed by its frequency ω_{fi} . Finally, the minimum impact parameter b_{min} in Eq. IV.21 is the one below which nuclear reactions will occur with higher probability than Coulomb induced ones and hence should be greater than the sum of the two nuclear radii. According to [Scheit 98] it is nearly equal to the distance of closest approach and can be written:

$$b_{min} = 1.25 (A_t^{1/3} + A_p^{1/3}) + \Delta_s \quad ; \quad \Delta_s \sim 2-4 \text{ fm} \quad (\text{IV.25})$$

where A_t and A_p are mass number of target and projectile respectively.

IV.2 Inelastic scattering below the neutron emission threshold

Results According to Eq. IV.25 and by using the Rutherford scattering equation the maximum center of mass scattering angle below which Coulomb excitation is dominant in the $^{26}\text{Ne}+^{208}\text{Pb}$ reaction is $4.1 \pm .3^\circ$. Assuming this condition being fulfilled (see Fig. III.13 (a)), from the amount of detected 2018 keV 2^+ gammas emitted in coincidence with ^{26}Ne (see shaded area in Fig. IV.3), we evaluated the $B(E2; 0^+ \rightarrow 2^+)$ from the experimental Coulomb cross section which is defined as:

$$\sigma_{exp} = \frac{N_\gamma}{\epsilon_{tot}} \frac{1}{N_{inc} N_t} \quad \text{with} \quad N_t = \frac{\mathcal{N}_A \rho_t}{A_t} \quad (\text{IV.26})$$

where N_γ stands for the number of detected gammas of interest, ϵ_{tot} the total detection efficiency, N_i the integrated number of incident nuclei from the beam, and N_t the number of nuclei in the target, calculated from the Avogadro number \mathcal{N}_A , the target areal density ρ_t and its atomic mass number A_t .

In order to evaluate the total detection efficiency we needed to estimate the angular correlation between gamma and outgoing nucleus. It is expressed as a sum of even order Legendre polynomials:

$$W(\theta) = \sum_{k \text{ even}} a_k P_k(\cos(\theta)) \quad (\text{IV.27})$$

The a_k coefficients in the Coulomb excitation have been calculated using the following expressions:

$$\begin{aligned} a_k = & \sum_{\mu, L, L'} \left| G_{\pi\lambda\mu} \left(\frac{c}{v} \right) \right|^2 g_\mu(\xi(b_{min})) \begin{pmatrix} \lambda & \lambda & k \\ \mu & -\mu & 0 \end{pmatrix} \\ & \times \left\{ \begin{matrix} I_f & I_f & k \\ \lambda & -\lambda & I_i \end{matrix} \right\} F_k(L, L', I_{ff}, I_f) \sqrt{2k+1} \delta_L \delta_{L'} \end{aligned} \quad (\text{IV.28})$$

where ‘ $(\begin{smallmatrix} \dots \\ \dots \end{smallmatrix})$ ’ stands for Wigner 3j-symbol and ‘ $\left\{ \begin{smallmatrix} \dots \\ \dots \end{smallmatrix} \right\}$ ’ for Wigner 6j-symbol. F_k is the γ - γ correlation function which can be written:

$$\begin{aligned} F_k(L, L', I_1, I_2) = & (-1)^{I_1+I_2-1} \sqrt{(2k+1)(2I_1+1)(2L+1)(2L'+1)} \\ & \times \begin{pmatrix} L & L' & k \\ 1 & -1 & 0 \end{pmatrix} \left\{ \begin{matrix} L & L' & k \\ I_2 & I_2 & I_1 \end{matrix} \right\} \end{aligned} \quad (\text{IV.29})$$

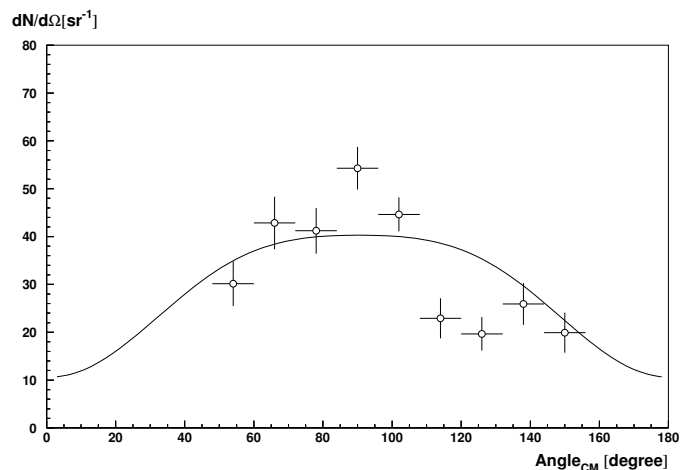


Figure IV.7: Experimental angular distribution (\circ) for $2^+ \rightarrow 0^+ \gamma$ in ^{26}Ne compared to calculations (plain line) based on [Alder 75]

The center of mass angular distribution of the gamma-ray from 2_1^+ to ground state transition in ^{26}Ne in coincidence with the detection of this nucleus in the silicon telescope is compared to the theoretical angular distribution in Fig. IV.7. The net result of the angular correlation effect with respect to an isotropic emission is a slight decrease of the efficiency from 13% to 11%. According to the efficiency measurement performed in Sec. III.2.2, the peak efficiency is subject to a relative 10% error. Taking this effect into account the background subtracted cross section is $\sigma = 68 \pm 8$ mb.

The $B(E2; 0^+ \rightarrow 2^+)$ is then evaluated using an equivalent program as [Pritychenko 99a]. According to Eq. IV.25 the error on the minimum impact parameter is ± 1 fm and we estimated its impact on the $B(E2)$ value as listed in Table IV.2. These variations were averaged to give $B(E2; 0^+ \rightarrow 2^+) = 230 \pm 30$ e²fm⁴ in very good agreement with 228(41) e²fm⁴ from [Pritychenko 99b].

IV.2 Inelastic scattering below the neutron emission threshold

(a)		(b)	
Impact parameter $1.25 (A_t^{1/3} + A_p^{1/3})$	B(E2) [$e^2\text{fm}^4$]	Cross section [mb]	B(E2) [$e^2\text{fm}^4$]
+2 fm	200	60 mb	190
+3 fm	230	68 mb	230
+4 fm	265	76 mb	270

At constant cross section (68 mb) At constant impact parameter (+3 fm)

Table IV.2: Variations of the $B(E2)$ value with (a) the impact parameter (b) the cross section

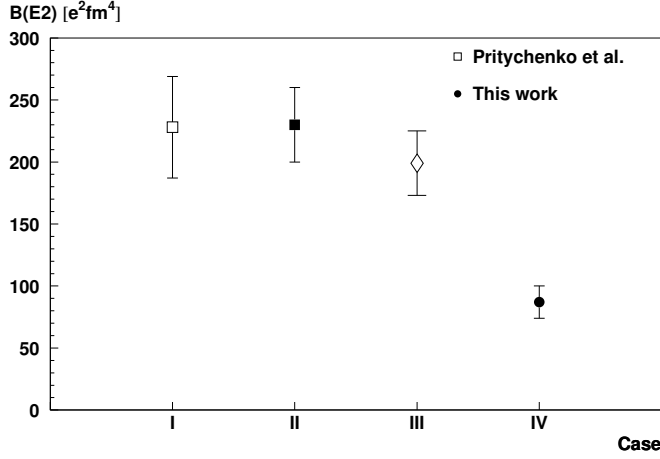


Figure IV.8: (□) Previous value of the $B(E2)$ in ^{26}Ne . Marker ■, ◇ and ●: Evolution of this value with the different methods of extraction (see text). The error bar comes from the statistics as well as the estimation of the feeding from the ^{26}Ne 0_2^+ to the 2_1^+ state.

Discussion on B(E2)

In the previous section two different methods of extraction of the $B(E2; 0^+ \rightarrow 2^+)$ of ^{26}Ne have been applied, leading to different values. In this section, we will discuss the origin of the discrepancy as well as the reliability of the new

result.

The method using the gamma-ray decay cross section presented in Sec. IV.2.2 supposes – as in [Pritychenko 99b] – that the reaction is purely a Coulomb excitation, due to a scattering angle selection. The former result extracted for ^{26}Ne at 41.7 MeV/n impinging on ^{197}Au and our result on $^{\text{nat}}\text{Pb}$ target, plotted as case (I) and case (II) on Fig. IV.8 (a) are consistent with each other. The advantage of this method is the perfect understanding of the reaction process. However it relies on the good estimation of the minimum impact parameter, see Eq. IV.21, *via* the scattering angle.

Using ECIS 97 and the hypothesis that no nuclear reaction – *i.e.* a null nuclear deformation parameter $\beta_N = 0$. – is involved, we calculated the Coulomb deformation parameter $\beta_C = 0.465 \pm 0.028$ that reproduces the reaction cross section. We hence present in Fig. IV.8 (a) case (III) the $B(E2) = 197 \pm 23 \text{ e}^2\text{fm}^4$ value deduced from this analysis. The error bar comes from discrepancies in β_C reproducing the error on the cross section. The value is in good agreement with the previous method.

However, at these incident energies, a contribution from nuclear processes to the cross section should be quantified. It is clear by looking at Fig. IV.5 (b) that the dashed line representing the angular scattering distribution in the hypothesis that no nuclear reaction is involved is hardly compatible with the experimental distribution. The angular distribution providing a constraint of the deformation parameters, it proves the necessity to include the nuclear contribution in the excitation process. In this last case (IV), we extracted a smaller value of $B(E2) = 87 \pm 13 \text{ e}^2\text{fm}^4$. Note that the error bars here only correspond to statistics. In order to evaluate the sensibility to the optical potentials we performed the same analysis using $^{20}\text{Ne}+^{208}\text{Pb}$ at 41 MeV/n optical potential parameters [Suomijärvi 90] and found a $B(E2) = 99 \pm 14 \text{ e}^2\text{fm}^4$ compatible with our results.

In the following we retained the $B(E2) = 87 \pm 13 \text{ e}^2\text{fm}^4$ value and compared to the other experimental $B(E2)$ of $A = 18$ to $A = 30$ even-even neon isotopes in Fig. IV.9 (b). One should note that the ^{28}Ne case

IV.2 Inelastic scattering below the neutron emission threshold

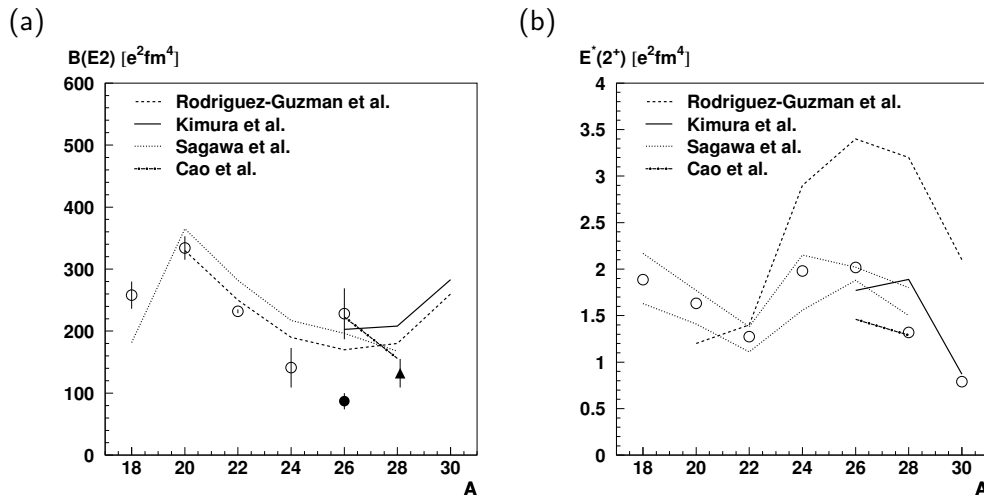


Figure IV.9: Even neon isotope (a) 2_1^+ energy and (b) $B(E2; 0^+ \rightarrow 2^+)$ value, compared with theoretical calculations. Open circles are previous experimental results, the closed circle and the closed triangle recent results.

from [Iwasaki 05], recently extracted by a method comparing the integrated cross section on lead and carbon targets, is much below and hardly compatible, within the error, with the one from [Pritychenko 99b]. We compared them with theoretical calculations recently published. Rodríguez-Guzmán *et al.* [Rodríguez-Guzmán 03] performed a Angular Momentum Projected Generator Coordinate Method (AMPGCM) with Gogny force (dashed line), and they reproduce well the $B(E2)$ trend. However their 2^+ excitation energies are almost twice larger than the experiment. Kimura and Horiuchi [Kimura 04] studied the low-lying level structures of ^{26}Ne in the framework of the deformed-basis antisymmetrized molecular dynamics plus generator coordinate method using Gogny D1S force (AMD+GCM). Their calculation (solid line) predicts well the excitation energies and follows the $B(E2)$ trend but gives an absolute transition strength twice as large as the experimental data. Concerning the Shell Model calculation of Sagawa *et al.* [Sagawa 04], their predicted excitation energies are in average for the neon isotope chain within 20% error bar and their $B(E2)$ trend deviates on aver-

age by 30%. Finally, in dotted-dashed line is presented the prediction from Cao et Ma article [Cao 05b] from which the $E1$ strength presented in introduction is extracted. Their theoretical prediction is larger than the new experimental value of ours.

In conclusion we cite a theoretical study [Obertelli 05b] in the Hartree-Fock Bogoliubov plus Generator Coordinate Method (HFB+GCM) which suggests the $N = 16$ sub-shell closure. It predicts an excitation energy of 2.19 MeV but a $B(E2)$ equals to $89 \text{ e}^2\text{fm}^4$. Note that the value obtained in our analysis is very close to the later values and the overall tendency of the E_{2+} and $B(E2)$ in neon isotopes is compatible with the $N = 16$ sub-shell closure.

IV.3 Excitation Energy spectrum of ^{26}Ne above the neutron threshold

IV.3.1 The method

The excitation energy of an unbound state in the nucleus ^AX decaying to a state in ^{A-1}X can be expressed by:

$$E^* = E_{rel} + S_n + \sum_j E_{\gamma_j} \quad (\text{IV.30})$$

where S_n is the one neutron emission threshold, E_{γ_i} the energies of the decay γ -rays emitted from $^{A-1}\text{X}^*$, E_{rel} is the relative energy between the neutron and the ^{A-1}X nucleus:

$$E_{rel} = I - M_{A-1\text{X}} - M_n \quad (\text{IV.31})$$

with $M_{A-1\text{X}}$ mass of ^{A-1}X and M_n mass of the neutron and I invariant mass.

The above formulae, when they are developed like in Sec. I.3.4, show that a measurement of the excitation energy requires the determination of the fragment and the neutron velocities and their relative angle as well as the

IV.3 ^{26}Ne excitation energy above S_n

total amount of energy released by the γ -rays emitted from the fragments after neutron emission. In our experiment, however, the γ -detection efficiency was not high enough to provide such a calorimetry so that the excitation energy spectrum could not be obtained on an event-by-event basis.

Alternatively, we used a method based on an adequate subtraction of relative energy spectra which will be presented in a simplified case in this first section.

Illustration by a simplified case

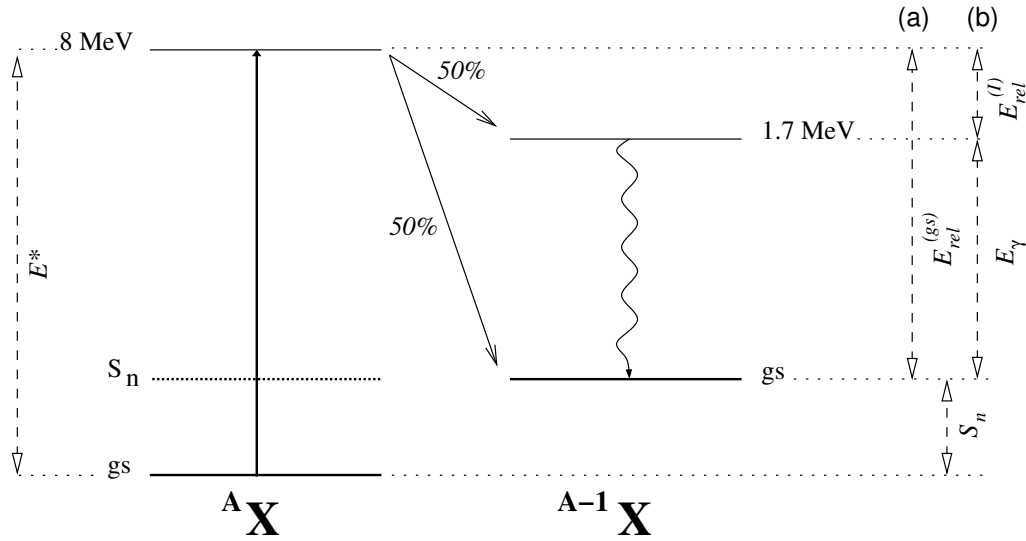


Figure IV.10: Level scheme for the mother and the daughter nuclei with their decay paths implemented in the simulation (see text). We plotted the different components of the reconstructed excitation energy in case (a) where the mother nucleus decays to the ground state of the daughter nucleus, and in case (b) where it decays to the excited state.

The method is illustrated in the schematic case where the daughter nucleus ^{A-1}X has only one excited state below its two-neutron emission threshold, as illustrated in Fig. IV.10. The excitation energy spectrum can be decomposed in the sum of two contributions:

- the decay of ${}^A\text{X}$ to the ground-state of ${}^{A-1}\text{X}$ (gs)
- the decay of ${}^A\text{X}$ to the excited state of ${}^{A-1}\text{X}$ (I).

In the following, $[\dots]$ stands for spectrum. The first contribution can be obtained by subtracting from the inclusive relative energy spectrum $[E_{rel}({}^{A-1}\text{X}, n)]$ the relative spectrum of γ -ray-coincidence events $[E_{rel}({}^{A-1}\text{X}, n)|_{\gamma}]$ divided by the γ -ray detection efficiency ϵ and finally shifted “ \leftrightarrow ” by the S_n value *i.e.* :

$$[E^*]^{(gs)} = \underbrace{[E_{rel}({}^{A-1}\text{X}, n)] - [E_{rel}({}^{A-1}\text{X}, n)|_{\gamma}]}_{[E_{rel}^{(gs)}]} / \epsilon \leftrightarrow S_n \quad (\text{IV.32})$$

The different components $(E_{rel}^{(gs)}, S_n)$ of the reconstructed energy and their correspondence in both daughter and mother nuclei level scheme are visualized in Fig. IV.10 case (a).

The second contribution is simply the relative energy spectrum of γ -ray-coincidence events shifted by the γ -ray energy, according to Eq. IV.30 :

$$[E^*]^{(I)} = \underbrace{[E_{rel}({}^{A-1}\text{X}, n)|_{\gamma}]}_{[E_{rel}^{(I)}]} / \epsilon \leftrightarrow S_n \leftrightarrow E_{\gamma} \quad (\text{IV.33})$$

Again Fig. IV.10 case (b) illustrates the different components $(E_{rel}^{(I)}, S_n)$ and E_{γ} of the reconstructed energy.

Finally, the excitation energy spectrum for the ${}^{25}\text{Ne}+n$ decay channel is given by the sum of the two contributions:

$$[E^*] = [E^*]^{gs} + [E^*]^{(I)} \quad (\text{IV.34})$$

Simulation

We performed a Monte-Carlo simulation using the Geant 3 code [Brun 86] where we suppose that ${}^A\text{X}$ is excited to one 8.5 MeV state and decays by neutron emission to the ${}^{A-1}\text{X}$ ground state or to the $E_I^* = 1.7$ MeV ${}^{A-1}\text{X}$

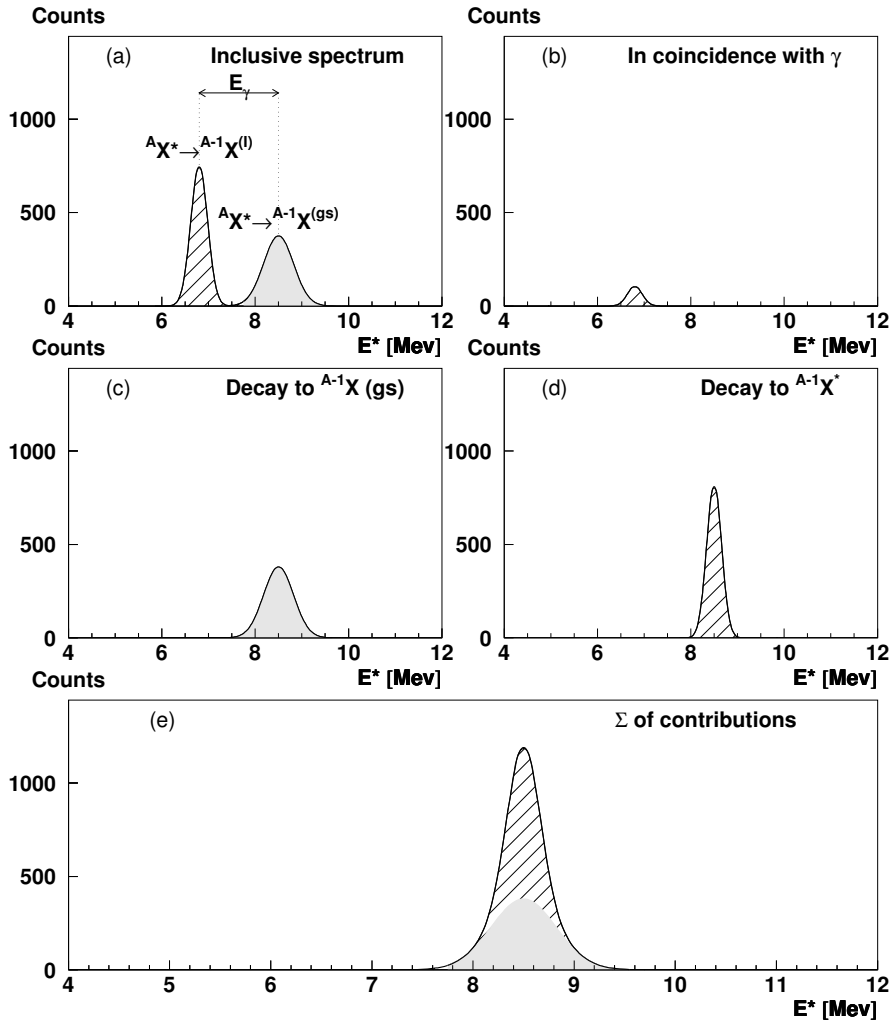


Figure IV.11: (a) Reconstructed excitation spectrum of ^{A-1}X which decay to all states of ^{A-1}X . (b) Same spectrum in coincidence with γ from ^{A-1}X decay, in order to compare the spectrum (a) is added in dotted line. (c) Rebuild excitation spectrum of ^{A-1}X which decay to $^{A-1}\text{X}(gs)$ (shaded area). The dotted histogram is the contribution removed from Fig. IV.11 (a) using Eq. IV.32. (d) Same spectrum for the decay to $^{A-1}\text{X}(l)$ (shaded area). It is obtained from Fig. IV.11 (b) (dotted histogram) using the transformation describe in Eq. IV.33. (e) Finally the last two contributions are added.

excited state with equal branching ratios. The intermediate spectra are presented in Fig. IV.11 (a) and Fig. IV.11 (b) respectively for the $^{A-1}\text{X-n}$ relative energy spectrum measured inclusively and the spectrum in coincidence with the 1.7 MeV decay γ -ray. One sees that in (a), where no gate on γ -ray energy is applied, two peaks are present: the one with higher energy corresponds to (gs) decay, whereas the one with lower energy (dashed area) the decay to (I). They are separated by 1.7 MeV *i.e.* the energy of the excited state E_I in the daughter nucleus. This is confirmed by the fact that in (b), relative energy spectrum obtained in coincidence with the γ -decay, only the lower energy peak (dashed area) subsists. The small amount of events is due to the γ detection efficiency of $\epsilon \sim 13 \pm 0.7\%$.

Fig. IV.11 (c) and Fig. IV.11 (d) corresponds to the next s of analysis. They are respectively the contribution from the excitation energy spectrum which decays to $^{A-1}\text{X}(\text{gs})$ and to one which decays to $^{A-1}\text{X}(\text{I})$, obtained by applying the treatment based on Eq. IV.32 and Eq. IV.33. One can see that the areas drawn by the distributions are equal, which is due to the fact that the probabilities of these two contributions were chosen equal.

Finally, following Eq. IV.34, the sum of the two contributions, is presented in Fig. IV.11 (e). We tested that the number of events in this spectrum is the same in Fig. IV.11 (a) and, as expected, that the average energy is 8.5 MeV. The energy resolution is ~ 800 keV (FWHM).

In the next section, we will extract the complete level scheme of ^{25}Ne . The method discussed above can be applied in the case of this more complicated level scheme of the daughter nucleus. In Appendix A, a generalization to the case of two excited levels in the daughter nucleus is presented. We will see in the next section that the $^{26}\text{Ne} \rightarrow ^{25}\text{Ne} + \text{n}$ channel can be reduced to this simple case.

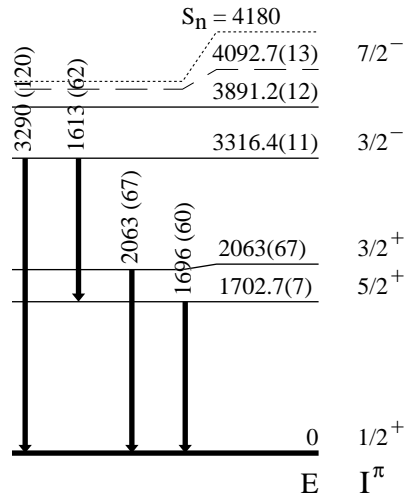


Figure IV.12: Known levels and confirmed ones in ^{25}Ne below one neutron emission threshold ($S_n = 4180$ keV), with detected gammas. The gammas in solid lines are these detected in this experiment, the dashed are known but not seen here. Spin and parity assignment comes from [Lemmon 05].

IV.3.2 Level scheme of daughter nucleus ^{25}Ne via γ -decay

The level scheme of ^{25}Ne obtained from the literature is displayed in Fig. IV.12. The four states at 1702.7(7) keV, 3316.4(11) keV, 3891.2(12) keV and 4092.7(11) keV were seen in [Wilcox 73], [Woods 85] and [Reed 99] and are considered established with certainty. The 2030(50) keV state is referenced only in [Wilcox 73].

Analysis by means of simulations, contributions

The gamma energy distribution measured by the NaI array DALI in coincidence with a ^{25}Ne in the silicon detector is displayed in Fig. IV.13 (a) for the lead target. The same spectrum gated further by the detection of one

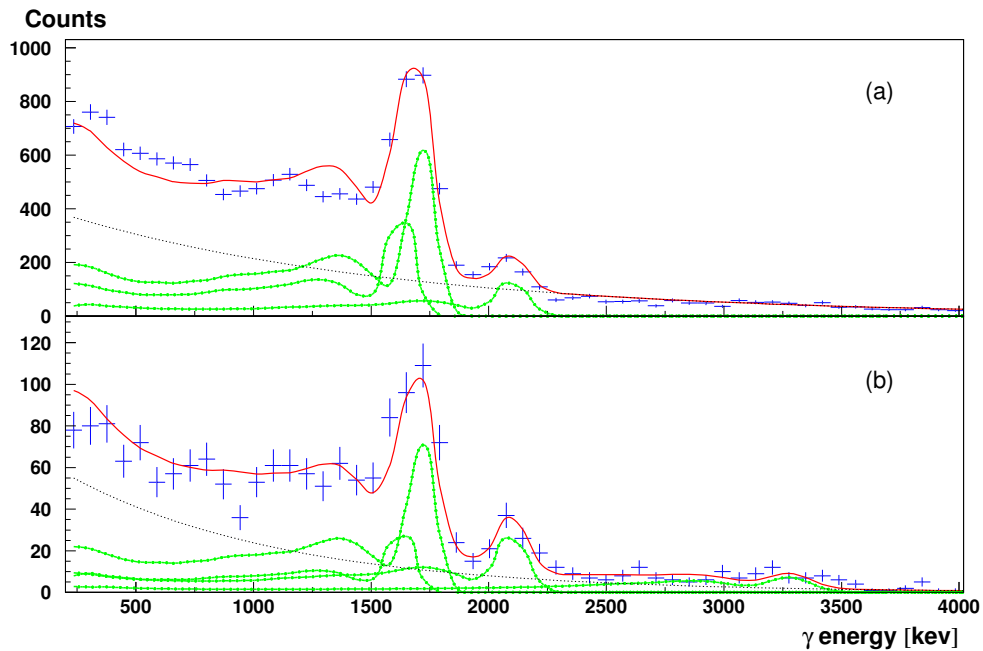


Figure IV.13: γ -ray energy distribution in DALI, fitted with simulation. Points represent data with statistical errors, plain line the sum of all simulated contribution and dot-dashed lines each gamma weighted contribution. The dotted line represents the exponential fit of the background. Graph (a) is obtained by DALI in coincidence with ^{25}Ne , (b) in coincidence with a ^{25}Ne and one neutron in the neutron wall.

neutron is shown in Fig. IV.13 (b). In both cases the normalized spectra obtained with the empty target were subtracted. Two peaks appear centered around 1700 keV and 2050 keV respectively. According to the DALI resolution analysis, presented in Sec. III.2.5, the 1700 keV peak is broad, and is expected to be composed of more than one line. In the neutron gated spectrum, an additional peak appears at higher energy around 3250 keV. In a first step, a simulation of the in-flight decay of ^{25}Ne was performed for the five transitions mentioned before.

Before performing a fit of the experimental data with these calculated contributions, the background component was evaluated. Its presence is

IV.3 ^{26}Ne excitation energy above S_n

confirmed by the high rate of low energy γ -rays and the rather homogeneous distribution at high energy, which cannot be explained by simulations which only treats the decay of the outgoing nucleus. The background is better reproduced by considering the excitations of the target, as for example explained in [Yamada 04]. This reference also shows that is not sufficient, and that the background can be modeled by an exponential fit, normalized to the high energy γ -rays data part of the spectrum. Its contribution is treated the same way as a contribution coming from ^{25}Ne gamma decay and we represented it in Fig. IV.13 (a) and Fig. IV.13 (b) by a dotted line.

The comparison of the experimental data with the result of the likelihood fit including the five gamma transitions and the background is shown in Fig. IV.13 (a) and Fig. IV.13 (b). This method allowed us to highlight the presence of a 3250 ± 125 keV gamma we assigned to the direct decay from 3316 keV excited state to ground state. The contributions of each transition are listed in Table IV.3 for both the lead and the aluminum target. Within the error bars, the population of the excited states of ^{25}Ne is similar for the two targets.

The fit has also been performed by simulating the 1613 keV and 1696 keV γ -rays cascade from the 3316 keV and the results found are comparable.

Gamma energy [keV]	γ contribution [%] in coincidence:			
	with ^{25}Ne		with ^{25}Ne and <i>one</i> neutron	
Target	Pb	Al	Pb	Al
1613 ± 62	25 ± 4 %	20 ± 10 %	20 ± 4 %	15 ± 4 %
1696 ± 60	50 ± 9 %	50 ± 10 %	50 ± 7 %	60 ± 6 %
2063 ± 80	15 ± 2 %	20 ± 5 %	20 ± 1 %	20 ± 2 %
3250 ± 125	5 ± 4 %	10 ± 7 %	10 ± 5 %	5 ± 2 %

Table IV.3: Contribution of each detected photons emitted from ^{25}Ne

Confirmation of the 2 MeV excited state

We measured a γ at 2063 ± 67 keV and thus confirm a state initially measured at 2030 ± 50 keV in the $^{26}\text{Mg}(^7\text{Li}, ^8\text{B})^{25}\text{Ne}$ transfer reaction [Wilcox 73] but unseen in the $^{26}\text{Mg}(^{13}\text{C}, ^{14}\text{O})^{25}\text{Ne}$ transfer reaction [Woods 85] and β decay from ^{25}F [Reed 99].

We exclude this 2050 keV photon to be contamination from both ^{26}Ne or ^{24}Ne $2^+ \rightarrow \text{gs}$ gamma decay (2018 keV and 1981 keV respectively) since our fragment separation is good enough as illustrated in Fig. IV.14 (b). This is also confirmed by looking at the two dimensional plot of the measure γ -energy versus the neon mass number of Fig. IV.14 (a). In coincidence with the ^{25}Ne ejectile two distinct peaks at ~ 1700 keV and ~ 2020 keV clearly appear. Finally this transition is observed in coincidence with a 1.25 MeV γ which corresponds to the decay cascade from the ^{25}Ne 3.3 MeV excited state (see below).

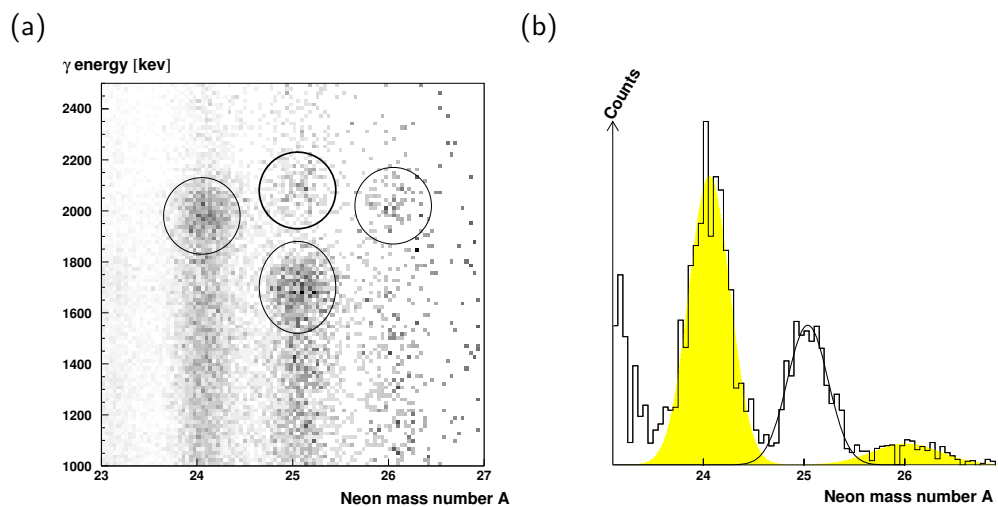


Figure IV.14: (a) Gamma energy distribution versus neon mass number, in coincidence with one neutron in the neutron wall. The circles highlight the ~ 2 MeV gammas for ^{24}Ne , ^{25}Ne and ^{26}Ne as well as the more intense 1.6 MeV and 1.7 MeV γ from ^{25}Ne . (b) Particle identification in silicons in coincidence with one neutron, showing the small overlap between $A = 24, 25$ and 26 neon isotopes.

Analysis of events with multiplicity equal to two

The resolution of ~ 125 keV (FWHM) is not sufficient to clearly separate the γ -ray lines at 1613 and 1703 keV in ^{25}Ne . However, we established the existence of the cascade from the 3316.4 keV excited state leading to both 1613 keV and 1703 keV γ by observing the photon energy distribution in coincidence with a second photon of energy 1700 to 1800 keV, *i.e.* the highest energy part of 1703 keV γ distribution[†]. For the events with γ -ray multiplicity two, the γ -ray energy spectrum in coincidence with a second transition of energies from 1700 keV to 1800 keV exhibits a peak centered at 1613 ± 62 keV, see Fig. IV.15 (a). Conversely a [1575; 1675] keV gate applied on the first gamma spectrum shows a peak at 1696 ± 60 keV in the second gamma spectrum.

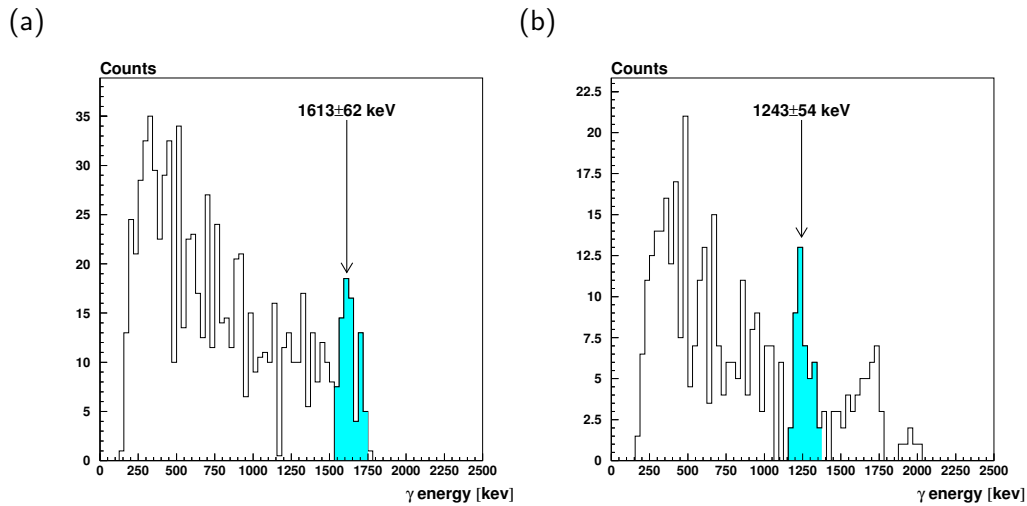


Figure IV.15: Doppler corrected gamma energy distribution in DALI, with multiplicity strictly 2: (a) represents the case in coincidence with a 1750 ± 50 keV γ in coincidence (b) the case where a 2050 ± 50 keV γ is required is coincidence.

The same analysis shows the presence of a cascade from the two transitions at 2063 ± 67 keV and 1243 ± 54 keV as illustrated in Fig. IV.15 (b). These

[†]Where the probability of an accidental detection of a 1613 keV photon is negligible.

γ -coincidence results confirm the one obtained by simulation in Sec. IV.3.2, on the existence of a 2 MeV excited state.

Conclusion on the ^{25}Ne level scheme

The previous sections allow us to draw the ^{25}Ne level scheme of Fig. IV.16. The γ -ray lines were observed at the 1613 ± 62 keV, 3290 ± 120 keV, 2063 ± 67 keV and 1696 ± 60 keV, which corresponds to three excited states at 1702 keV, 2063 keV and 3316 keV. This scheme will be used in the following analysis to reconstruct the ^{26}Ne excitation energy above the one neutron threshold.

IV.3.3 Excitation energy spectrum for ^{26}Ne , above one neutron emission threshold

We presented in Sec. IV.3.1 our method to build the ^{26}Ne excitation energy distribution is described using a simplified case. The starting point of the method is to build the relative energy spectra for the $^{25}\text{Ne}+n$ inclusive case and for the $^{25}\text{Ne}+n+\gamma_i$ coincidence events for each γ_i transition in ^{25}Ne . The level scheme for ^{25}Ne is displayed in Fig. IV.16. The two levels at 1.7 MeV and 2 MeV are considered to be degenerated since their energy difference is significantly smaller than the simulated resolution for relative energy (800 keV). Three levels in ^{25}Ne hence remain: the ground state (gs) and two excited states at ~ 1.9 MeV (I) and at 3.3 MeV (II). They can decay *via* the emission of three different gammas of 1882 keV, 1613 keV and 3316 keV, labeled $\bar{\gamma}^{(1)}$, $\gamma^{(2)}$ and $\gamma^{(3)}$ respectively.

Extraction We now apply the procedure presented in Sec. IV.3.1 to reconstruct the excitation energy spectrum for the $^{25}\text{Ne}+n$ channel. It was already pointed out in Sec. IV.3.2 that our energy resolution is not enough to separate the 1.7 MeV gamma emitted from the 1.7 MeV excited state ($\gamma^{(1)}$) decaying to the ground state and the 1.6 MeV gamma ($\gamma^{(2)}$) from the decay

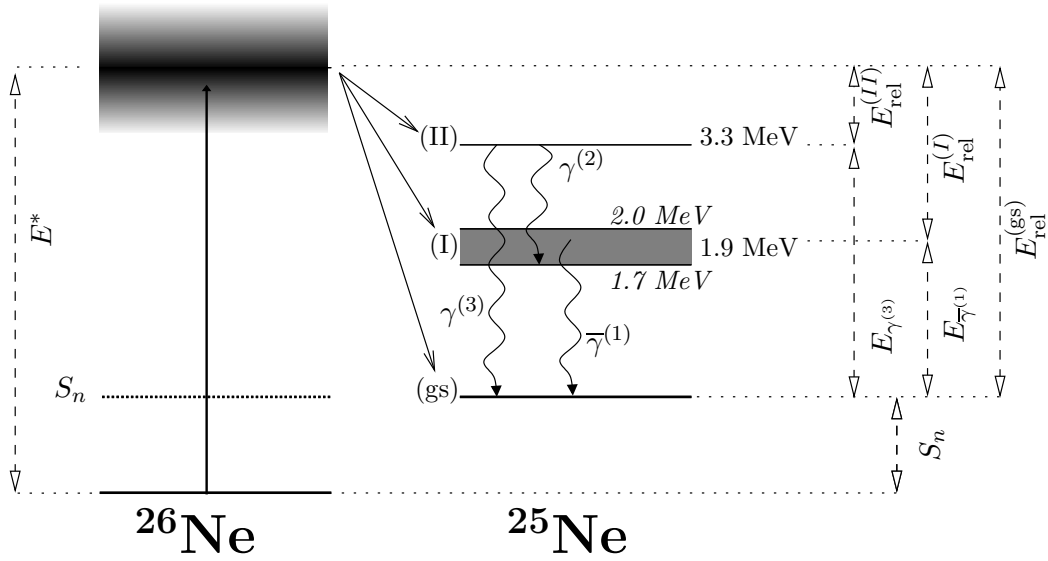


Figure IV.16: Retained scheme of decay from ^{26}Ne excited state above the one neutron emission threshold *via* $^{25}\text{Ne}+n$ channel. We present here a simplified level scheme for ^{25}Ne where the two first states are degenerated. We also illustrate the different components involved in the excitation energy reconstruction.

of the 3.3 MeV to the 1.7 MeV excited state. However, in the peak between 1500 and 1900 keV, the analysis of each contribution in Sec. IV.3.2 shows that the highest energy part (above 1750 keV) is almost ($\sim 95\%$) purely composed of $\bar{\gamma}^{(1)}$. We hence adopted as gate the [1750; 2200] keV energy interval to select our decay gamma of interest $\bar{\gamma}^{(1)}$ which includes the transition from the 2 MeV excited state. Finally in order to extract the events corresponding to the $^{25}\text{Ne}^*$ decay *via* $\gamma^{(2)}$ emission we consider the interval $E_\gamma \in [1500; 1615]$ keV from which we subtract with the adequate ratio ($\sim 20\%$) the events gated by the $E_\gamma \in [1750; 2200]$ keV energy interval.

The equations for each decay path contribution to the excitation energy

spectra thus become[‡]:

$$[E^{(II)}] = [E_{rel}|\bar{\gamma}^{(2)}] / \epsilon_{\bar{\gamma}^{(2)}} + [E_{rel}|\gamma^{(3)}] / \epsilon_{\gamma^{(3)}} \leftrightarrow S_n \leftrightarrow E_{\gamma^{(3)}}, \quad (IV.35)$$

$$[E^{(I)}] = [E_{rel}|\bar{\gamma}^{(1)}] / \epsilon_{\bar{\gamma}^{(1)}} - [E_{rel}|\bar{\gamma}^{(2)}] / \epsilon_{\bar{\gamma}^{(2)}} \leftrightarrow S_n \leftrightarrow E_{\bar{\gamma}^{(1)}}, \quad (IV.36)$$

$$[E^{(gs)}] = [E_{rel}] - [E_{rel}|\bar{\gamma}^{(1)}] / \epsilon_{\bar{\gamma}^{(1)}} - [E_{rel}|\gamma^{(3)}] / \epsilon_{\gamma^{(3)}} \leftrightarrow S_n, \quad (IV.37)$$

where $[E_{rel}]$ stands for the relative energy spectrum between the outgoing neutron and ^{25}Ne and $[E_{rel}|\gamma^{(i)}]$ is $[E_{rel}]$ in coincidence with the decay gamma $\gamma^{(i)}$ of energy $E_{\gamma^{(i)}}$. $\epsilon_{\gamma^{(i)}}$ is the corresponding gamma detection efficiency. According to the previous paragraph, $[E_{rel}|\bar{\gamma}^{(2)}]$ should be understood as:

$$[E_{rel}|\bar{\gamma}^{(2)}] = [E_{rel}|_{E_{\gamma} \in [1500; 1615] \text{keV}}] - [E_{rel}|_{E_{\gamma} \in [1750; 1900] \text{keV}}] / \epsilon_{12} \quad (IV.38)$$

where $1/\epsilon_{12} = 20\%$ is the estimated contribution of $\bar{\gamma}^{(1)}$ in the $[1500; 1615]$ keV interval of energy.

Results for the excitation energy spectra, $^{25}\text{Ne}+n$ channel

The relative energy spectra as well as the final excitation energy spectrum for the lead target are displayed in Fig. IV.17. The first upper four panels correspond to the inclusive spectrum for $^{25}\text{Ne}+n$ and the spectra associated with $\bar{\gamma}^{(1)}$, $\bar{\gamma}^{(2)}$ and $\gamma^{(3)}$ respectively. The next three in the middle as the spectra corresponding to Eq. IV.37, Eq. IV.36 and Eq. IV.35 for the excitation energy contribution decaying to (gs), (I) and (II) respectively. Finally the bottom panel is the sum of these three contributions. We checked that the number of events is conserved along the different procedures. The number of counts in the relative energy spectrum in coincidence with a photon from ^{25}Ne is, as expected, roughly the number of events from the inclusive spectrum which multiplied by the γ -ray efficiency. It is very interesting to note that the contribution of the ^{26}Ne decaying to the ground state of the

[‡]We remind that the notation $[...]$ stands for spectrum

IV.3 ^{26}Ne excitation energy above S_n

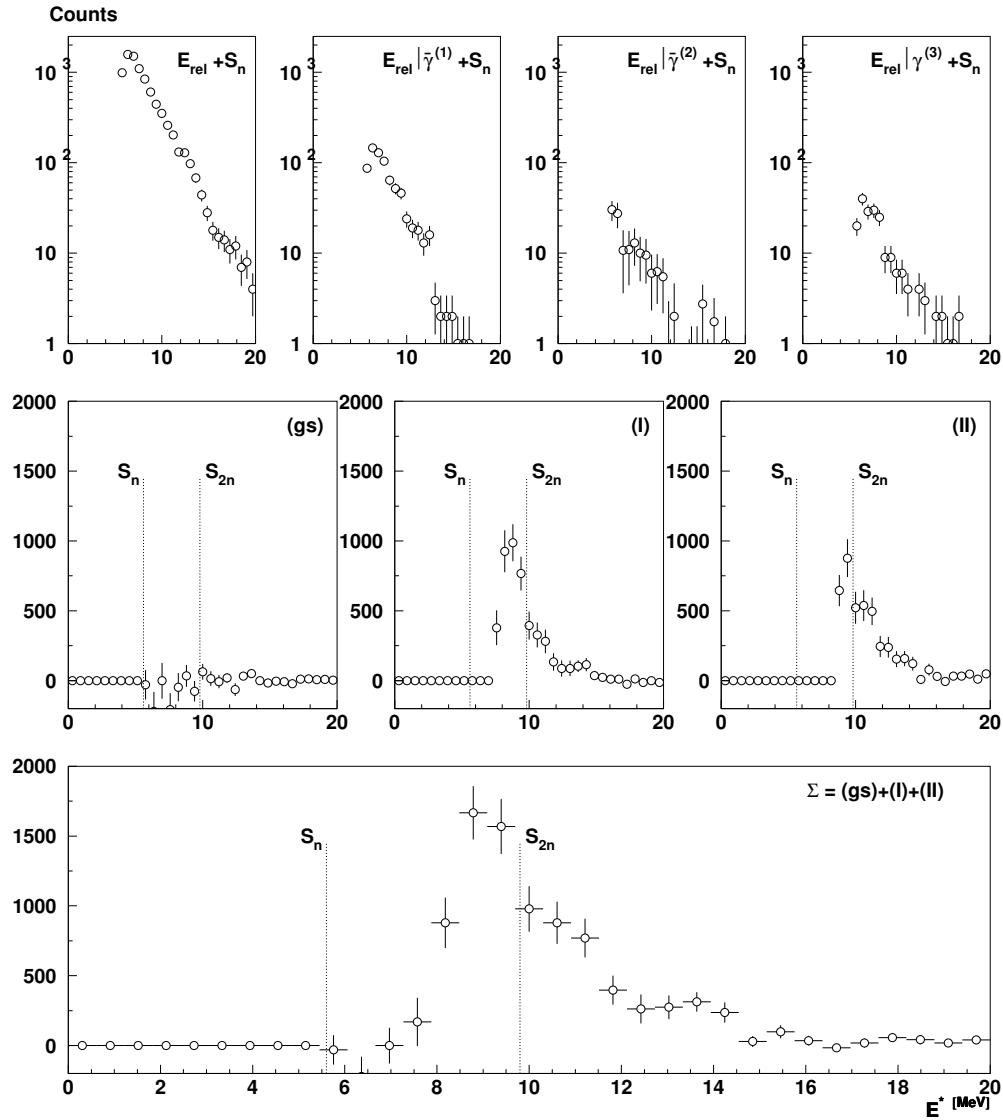


Figure IV.17: Relative energy spectrum, shifted with the one neutron emission threshold S_n . The first row presents the results for inclusive and exclusive spectra (see text). The second row shows the different components of the excitation energy spectrum for each decay path (see text). The last panel is the sum of the previous three histograms.

^{25}Ne is compatible with zero, and since the branching ratio from the initial state to the final state gives information on the initial wave function, this point will be discussed in the following. The contribution decaying to the two ^{25}Ne excited states both show a structure located around 9 MeV excitation energy. The same procedures have been applied to the case of the aluminum target.

We present in Fig. IV.18 the final results for the differential cross section spectra of the excitation energy for both lead and aluminum targets. The left column (Fig. IV.18 (a) and Fig. IV.18 (c)) compares the spectrum obtained without background subtraction (solid line) and its corresponding normalized background (dashed line), whereas the column on the right (Fig. IV.18 (b) and Fig. IV.18 (d)) is the result after subtraction of this background. The background presented here is obtained from the empty target data to which we applied the same analysis treatment as in the lead or aluminum target cases.

From the spectra of Fig. IV.18 (b) and Fig. IV.18 (d) we conclude that some strength is present above 8 MeV excitation energy for both lead and aluminum targets, with a lower cross section for the latter. This indicates a sizable contribution of nuclear excitation to the cross section observed with lead target. The shape of our distributions might be due to the presence at 9.8 MeV of the two-neutron emission threshold and does not necessarily reflect the existence of a single excited state broadened by the resolution. The present work investigates the amount of strength for excitation energies between S_n and S_{2n} , but no results can be drawn above S_{2n} , which would necessitate an analysis of the $^{26}\text{Ne} \rightarrow ^{24}\text{Ne} + 2n$ channel. This is beyond the scope of the present work.

Extraction of the Coulomb excitation cross section

In order to extract the $L = 1$, Coulomb excitation cross section from which the $B(E1)$ will be deduced, the contribution from other multipolarities should be evaluate. According to ECIS calculations presented in Fig. IV.19 (a) all

IV.3 ^{26}Ne excitation energy above S_n

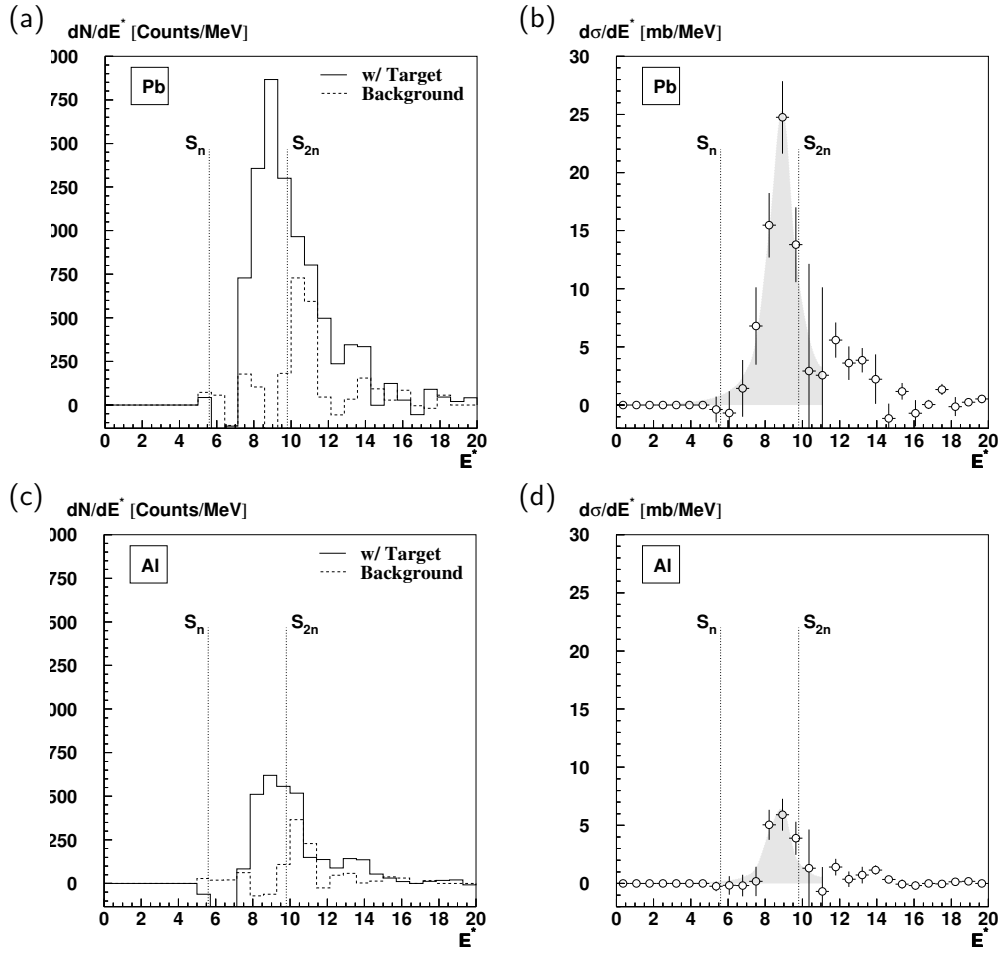


Figure IV.18: Excitation energy spectrum for ^{26}Ne impinging: (a), (b) on lead target ; (c), (d) on aluminum target. The left column present the results before background (empty target) subtraction (solid line) with the background (dashed line) superimposed. The right column presents the results of the subtraction. The shaded area is a tentative for Lorentzian fit.

the multipolarities greater than 2 present a rather similar shape of angular distribution. In the following, we will label by $L = 2$ the sum of all multipolarities greater or equal to 2.

We will now present two methods which have been used to extract the E1 contribution from the lead target data. In the first method, data taken

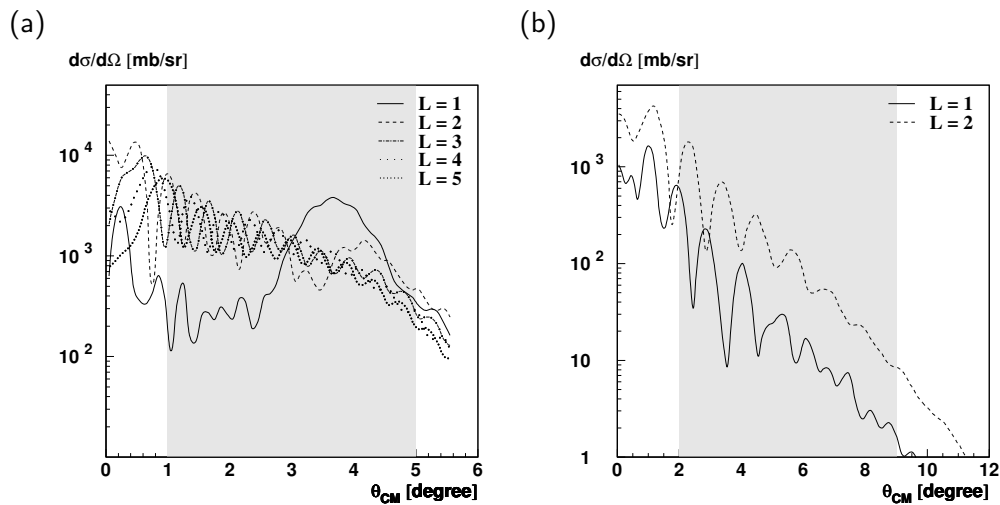


Figure IV.19: Angular distributions as predicted by ECIS 97, for ^{26}Ne impinging at 55 MeV/n on (a) lead and (b) aluminum target. We choose deformation parameters close to $\beta_{L=1} \sim 0.1$ and $\beta_{L \geq 2} \sim 0.2$, keeping the prescription on equal deformation lengths. The shaded area correspond to a silicon detector acceptance above 20%.

with the aluminum target are used to determine the $L = 2$ contribution to be subtracted.

The second method relies on the multipole decomposition of the angular distribution of the scattered ^{26}Ne , reconstructed from the $^{25}\text{Ne}+n$ events. It allowed us to evaluate the $L = 2$ contribution independently from the aluminum data.

Method 1: Integrated cross sections As mentioned above, the contribution of $L = 2$ for the lead target is obtained from the data on the aluminum target. In this section, we will use the total *integrated* cross section in lead and aluminum to deduce the *integrated* $L = 1$ cross section in lead *i.e.* :

$$\sigma_{\text{Pb}}^{L=1} \approx \sigma_{\text{Pb}} - \Lambda \sigma_{\text{Al}} \quad (\text{IV.39})$$

where Λ is a factor to be estimated.

IV.3 ^{26}Ne excitation energy above S_n

In order to extract these integrated cross sections, the overall detection efficiency for each target and each multipolarity was estimated. We hence simulated the reactions supposing an excitation energy of 9 MeV and the corresponding angular momentum.

Using the ECIS 97 code and assuming that the excitation energy spectra of Fig. IV.18 (d) corresponds only to $L = 2$ excitations with equal nuclear and Coulomb deformation lengths, we extract the deformation parameters which reproduce the integrated cross section in aluminum $\sigma_{\text{Al}} = 9.1 \pm 2.3$ mb.

The $L = 2$ cross section in lead was then calculated using the deformation lengths extracted in the previous step. We obtained $\sigma_{\text{Pb}}^{L=2} = 17 \pm 4.1$ mb. We deduced the corresponding number of events, from the experimental total number of events obtained with the Pb target, in order to obtain the remaining $L = 1$ events.

The resulting $\sigma_{\text{Pb}}^{L=1} = 49.4 \pm 4.7$ mb cross section corresponds, using ECIS 97, to a Coulomb deformation parameter of $\beta_C = 0.092 \pm 0.05$ which led to a $B(E1) = 0.602 \pm 0.059$ e²fm² via the relation $B(E1; 0^+ \rightarrow 1^-) = \left(\frac{3}{4\pi} Z_p e R_C \beta_C^{L=1}\right)^2$ with R_C the Coulomb radius [Bohr 98]. Note that β_C is obtained from the β_C^{eff} input in ECIS 97 by $\beta_C = \beta_C^{eff} * \frac{A}{2N}$ with A and N mass number and neutron number.

Note that using a simplistic approach (described below) we deduced a yield in the same order of magnitude. Since the reactions that excite the mother nucleus of mass A_p in a resonant state to the $^{25}\text{Ne}+n$ channel might be considered as a peripheral reaction and the ratio between the cross section with a target a of mass number A_a and a target b of mass number A_b can be written as the ratio of the sum of the radii [Nakamura 95]: $\Lambda = \frac{A_p^{1/3} + A_a^{1/3}}{A_p^{1/3} + A_b^{1/3}}$. Here $\Lambda = 1.49$. We obtained $\beta_C = 0.097 \pm 0.010$ hence $B(E1) = 0.773 \pm 0.055$ e²fm². This value is comparable to the previous result.

Method 2: Angular distribution Due to the high granularity and the good resolution of the present setup, it is possible to extract the angular distributions, despite the strong forward focusing of the reaction products.

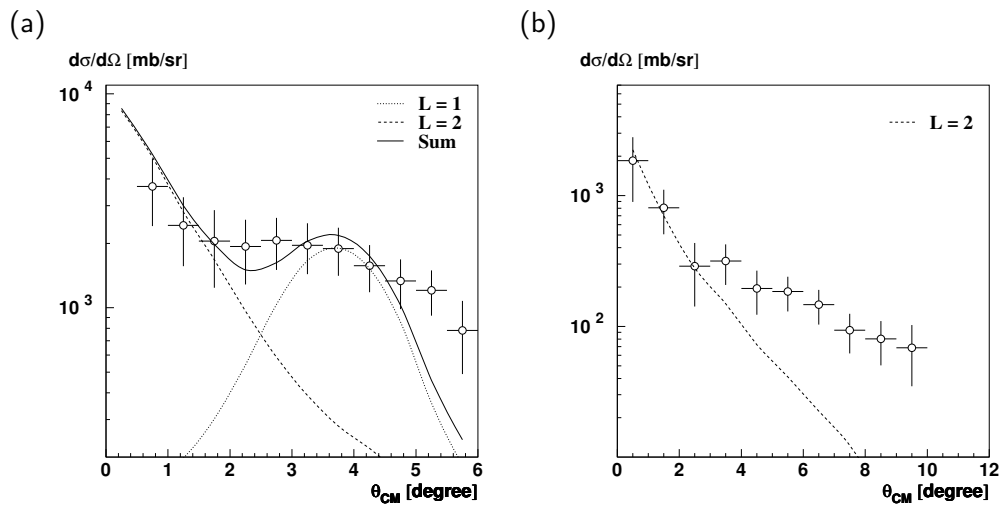


Figure IV.20: Angular distribution of scattered ^{26}Ne reconstructed from $^{25}\text{Ne} + n$ decay channel, for (a) lead target; (b) aluminum target. Dotted line is the theoretical, simulated angular distribution for $L = 2$, in dashed for the $L = 1$. Solid line is the sum of this theoretical contributions.

The second method that we have used to extract the E1 excitation relies on a multipole decomposition analysis of the angular distribution of the ^{26}Ne .

The scattering angle for the ^{26}Ne nucleus is build from the neutron and the ^{25}Ne momenta:

$$\cos \theta_{\text{lab}} = \frac{\vec{p}_n + \vec{p}_{25_{\text{Ne}}}}{|\vec{p}_n + \vec{p}_{25_{\text{Ne}}}|} \cdot \frac{\vec{p}_{26_{\text{Ne}}}}{|\vec{p}_{26_{\text{Ne}}}|} \quad (\text{IV.40})$$

where \vec{p}_n and $\vec{p}_{25_{\text{Ne}}}$ are the momentum of the outgoing neutron and ^{25}Ne respectively. $\vec{p}_{26_{\text{Ne}}}$ is the momentum of the ^{26}Ne before entering the target as obtained from beam detector informations.

The rather complex method of addition and subtraction which leads to the excitation energy spectra induces large error bars due to poor statistic in the relative energy spectra in coincidence with γ -rays. We hence did not perform it for the angular distribution. But since our strength is located within a narrow excitation energy interval and since no contribution decaying

to the ground state is seen in the different excitation energy spectra shown in Fig. IV.18 (b) and Fig. IV.18 (d), we can remove partly the high excitation energy events ($E^* \geq S_{2n}$) by gating our angular distributions with a relative energy lower than the emission threshold of two neutrons minus the first ^{25}Ne first excited state energy. Before converting the angular distribution spectrum in cross section, counts due to background has been subtracted using the run with empty target normalized to the same number of incident particles.

Results are displayed for lead and aluminum targets in Fig. IV.20 (a) and Fig. IV.20 (b) respectively. The $L = 1$ and $L = 2$ calculated angular distributions (dashed and dotted lines) were obtained from simulation based on ECIS 97 angular distribution calculated for $E^* = 9$ MeV. In a first step the $L = 2$ component was fitted to the Al data for small scattering angles and the corresponding deformation parameters were used to calculate the $L = 2$ component in Pb target. Finally, using this latter extrapolated contribution, a $L=1$ component is added and fitted to the data. We obtained a reduced transition probability of $B(E1) = 0.471 \pm 0.225$ e²fm². It has to be noted that the cross section at large angles for the aluminum target is not reproduced by a our $L = 2$ contribution. As can be seen on Fig. IV.20 (b) neither a $L = 1$ nor higher multi-polarities, whose predicted shapes are similar to $L = 2$, can be invoked to explain the disagreement. Since the cross section at these large center-of-mass angles is low, small contributions from processes other than elastic excitation (such as pick-up/break-up, direct break-up, ...) can become sizable. The origin of this contribution has not been understood so far. The same arguments can be given for the two points at large angle in the angular distribution obtained with lead target.

In a second method, the fit was performed directly, independently of the data on the aluminum target, by minimizing the chi square for a sum of calculated $L = 1$ and $L = 2$ distributions in the lead target. The result obtained for the contribution of the two multipolarity gives $\beta_N = 0.107 \pm 0.018$, $\beta_C = 0.085 \pm 0.014$ *i.e.* $B(E1) = 0.544 \pm 0.183$ e²fm². This method

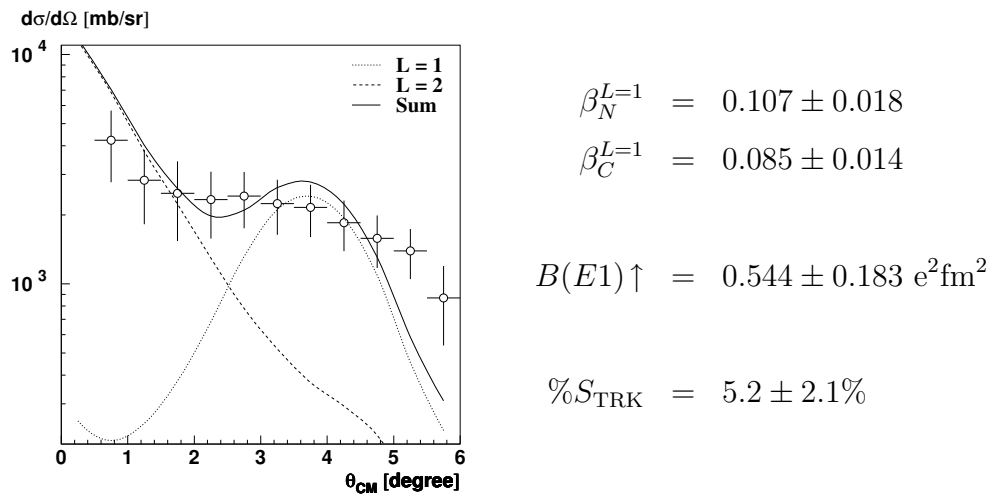


Figure IV.21: Angular distribution for the strength around $E^* = 9$ MeV and the value extracted from direct fit of $L = 1$ (dashed line) and $L = 2$ (dotted line) theoretical calculation

is the most direct since it does not necessitate any extrapolation from Al to Pb and we adopted it to deduce our results. These last are displayed in Fig. IV.21 with the obtained values. If we now suppose that our $L = 2$ distribution is *really* a $L = 2$ we obtain $\beta_N = 0.228 \pm 0.018$, $\beta_C = 0.206 \pm 0.016$ which corresponds to $B(E2) \uparrow = 38.8 \pm 6.0 \text{ e}^2\text{fm}^4$.

IV.3.4 Discussion on the B(E1) value

The results from the two methods are listed in Table IV.4. The error bars correspond to the deviation of the deformation parameter while taking into account the Coulomb cross section error. For the Thomas-Reiche-Kuhn sum rule, we also included the error of the excitation energy. The two results are in agreement but as previously mentioned, the second value of $B(E1) = 0.544 \pm 0.183 \text{ e}^2\text{fm}^2$ will be retained here. Note that the smaller error bar in the *integrated* cross section method comes from the fact that the extrapolation factor Λ in Eq. IV.39 is theoretically calculated using ECIS 97 and its error not estimated.

IV.3 ^{26}Ne excitation energy above S_n

	$\sigma_{\text{Pb}}^{L=1}$ [mb]	$B(E1)$ [$e^2\text{fm}^2$]	$\%S_{TRK}$
Method 1	50.1 ± 4.9	0.602 ± 0.059	$5.9 \pm 1.0\%$
Method 2		0.544 ± 0.183	$5.2 \pm 2.1\%$

Table IV.4: Deduced $L = 1$ cross section, $B(E1)$ value and exhausted energy weighted sum rule, using lead target. Method 1: integrated cross section lead/aluminum subtraction method. Method 2: With angular distribution fit on lead only (see text).

Comparison with mean-field calculations

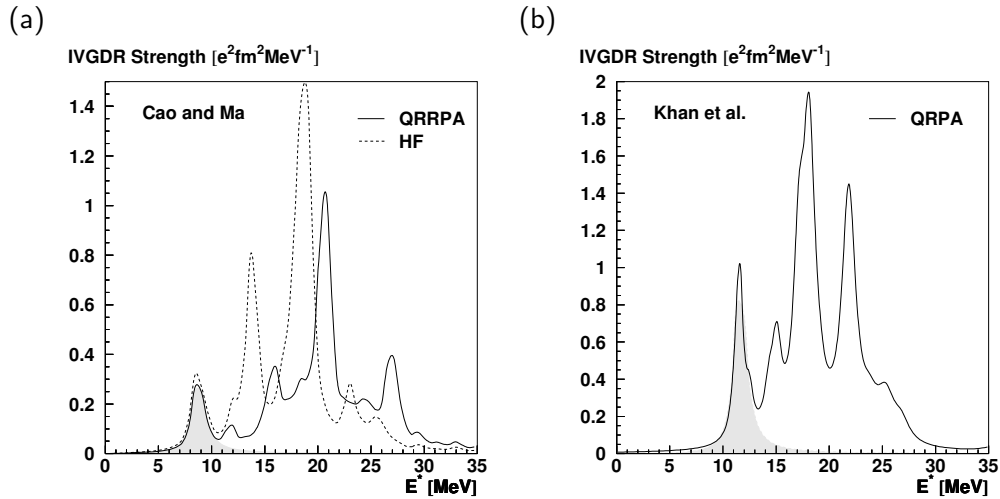


Figure IV.22: Iso-vector dipole strength in ^{26}Ne in (a) QRRPA framework, compared with Hartree-Foch calculations [Cao 05b] (b) in QRPA framework [Khan 05]

The results obtained from our experiment concerning the E1 transition are compared to theoretical mean field calculations.

In Chapter I we already presented results from Cao and Ma, displayed here in Fig. IV.22 (a). Using the Quasiparticle Relativistic Random Phase

Approximation framework and the response function formalism, in the extended RMF+BCS approach with the effective Lagrangian NL3 parameter set, they predicted a pygmy resonance centered around 8.4 MeV and which exhaust $\sim 4.5\%$ of the Thomas-Reiche-Kuhn energy weighted sum rule, which is closed to our experimental values. The comparison of their calculation with the Hartree-Foch calculation (in dashed line) tells us that the low-lying strength is dominated by non collective, single transitions. They predicted that the two configurations involved for the unperturbed strength are $\nu(2s_{1/2}^{-1}2p_{3/2})$ and $\nu(2s_{1/2}^{-1}2p_{1/2})$. We also remind here that this approach predicts for the 2_1^+ state $B(E2, \uparrow) = 223 \text{ e}^2\text{fm}^4$ at 1.46 MeV. The reduced transition probability is hence higher than our experimental $B(E2, \uparrow) = 87 \pm 13 \text{ e}^2\text{fm}^4$ result and the energy lower than the adopted value.

Another calculation has been performed by Khan *et al.* [Khan 05] and is presented in Fig. IV.22 (b). It is based on effective SGII Skyrme interactions and is performed in the spherical QRPA framework [Khan 00]. It predicts a redistribution of the strength at low energy centered around $E^* = 11.7 \text{ MeV}$ for which only one $\nu(1d_{3/2}^{-1}, 2p_{3/2})$ configuration contributes, which is radically different from the previous prediction. It however exhausts $\sim 5\%$ of the TRK. Note that this calculation gives $B(E2, \uparrow) = 206 \text{ e}^2\text{fm}^4$ for the 2_1^+ state at 2.73 MeV. The reduced transition probability is smaller than the previous theory, but still a little bit larger than our experiment. The differences with the experimental excitation energy are comparable.

Two other preliminary calculations have been performed in the QRPA framework using Gogny forces [Péru 05] and in the deformed relativistic QRPA framework [Ring 05]. They are displayed in Fig. IV.23 (a) and Fig. IV.23 (b) respectively. Both predict a redistribution of the strength at low energy, centered around 10.7 MeV and 7.5 MeV respectively. The first calculation also predicts that 1% of the TRK should be exhausted and gives a $B(E2, \uparrow) = 120 \text{ e}^2\text{fm}^4$ at $E^* = 2.3 \text{ MeV}$.

Note that recently shell-model calculations have been performed with suc-

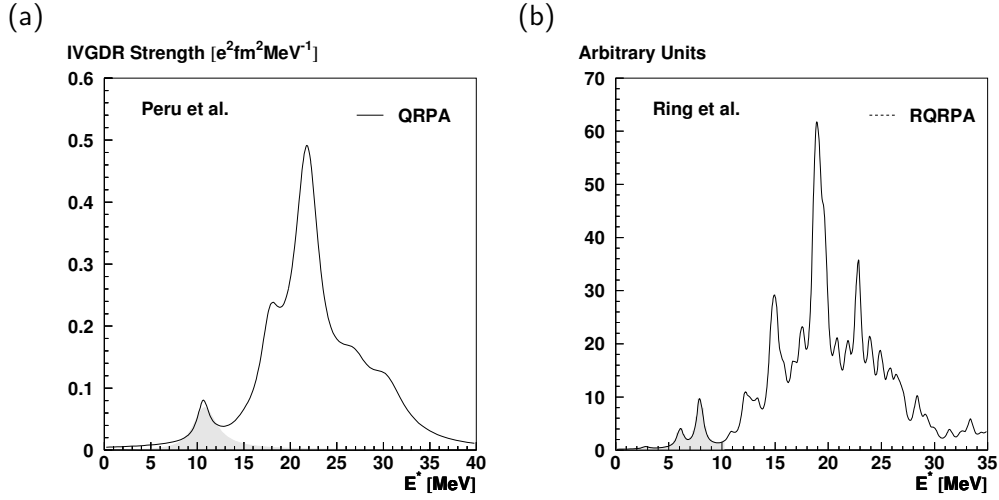


Figure IV.23: Iso-vector dipole strength in ^{26}Ne in (a) QRPA framework using Gogny force [Péru 05] (b) in deformed RQRPA framework [Ring 05]

cess [Nowacki 05] in that direction.

Comparison with other models

In order to discuss the collectivity of the corresponding 1^- state, we can express its $B(E1)$ in Weisskopf units for the single-neutron transition by [Van Der Woude 01]:

$$B_{\text{W.u.}}(E, 0 \rightarrow \lambda) = \frac{2\lambda + 1}{4\pi} \left(\frac{3}{\lambda + 3} \right)^2 (1.2A^{1/3})^2 \left(\frac{Z}{A} \right)^2 [\text{e}^2\text{fm}^{2\lambda}] \quad (\text{IV.41})$$

We obtain $B(E1, \uparrow) = 2.5 \pm 0.9$ W.u. This value indicates that a small number of single-particle transitions are present in the interval of energy observed and it might correspond to a small collectivity.

Another method to investigate the collectivity of our low lying state is given by the framework of the nuclear cluster state, where here the nucleus is divided into a core of Z_{Core} protons and N_{Core} neutrons and a additional cluster (Z_v, N_v) . We hence can express a cluster sum rules obtained from

this decomposition [Alhassid 82, Sagawa 90]. The *energy* weighted sum rule (S_{Clus}^{EW}) in case of a hypothetic neutron skin ($Z_v = 0$) then reads:

$$S_{\text{Clus}}^{EW} = \frac{9}{4\pi} \frac{N_v Z_{\text{Core}}^2 e^2 \hbar^2}{A A_{\text{Core}} 2m} = S_{\text{TRK}} \frac{Z_{\text{Core}} N_v}{A_{\text{Core}} N} \quad (\text{IV.42})$$

We compared it to the energy weighted cluster sum rule exhausted by our low lying structure and we obtained here $N_v \approx 2 \pm 1$ which would mean that only ~ 2 over 16 neutrons will participate to the excitation of this skin against a $^{24+1}_{11}\text{Ne}$ core. The non energy weighted cluster sum rule (S_{Clus}^{NEW}) can be related to the average fluctuation of the radial position $\langle R_v^2 \rangle$ of the center-of-mass of the participating N_v valence neutrons:

$$S_{\text{Clus}}^{NEW} = \frac{3}{4\pi} Z_{\text{Core}}^2 e^2 \left(\frac{N_v}{A_{\text{Core}}} \right)^2 \langle R_v^2 \rangle. \quad (\text{IV.43})$$

From the ratio with our $B(E1)$ value, we obtained here $\sqrt{\langle R_v^2 \rangle} = 2.5 \pm 1$ fm which has to be compared to the ^{26}Ne radius: $R = 1.2A^{1/3} \approx 3.6$ fm. In conclusion: in this classical framework 20% if the neutron of the ^{26}Ne will form a skin that, in case of collective excitation, will be shift away with a huge amplitude corresponding to almost 70% of the diameter of the nucleus. If we get back to our two fluids model of Sec. I.2.1 and by supposing the main giant dipole resonance peak to follow the systematic of Eq. I.6, by using the Eq. I.8 and the hypothesis that the core in a $^{24+1}_{11}\text{Ne}$ we obtain an excitation energy for the pygmy of $E^* = 5.0 \pm 1$ MeV, lower than our experiment.

Decay of pygmy resonances in ^{26}Ne

Our method allows us to extract for the first time data on the decay of pygmy resonance in ^{26}Ne . We present the experimental branching ratios on Table IV.5. The clear difference between the branching ratios obtained with lead and aluminum target proves that states of different nature have been excited. For comparison, we also performed a statistical decay calculation for $L = 1, 2, 3$ states using the CASCADE code [Puhlhofer 77], assuming spins and parities of ^{25}Ne states as presented in Fig. IV.12. It clearly shows

IV.3 ^{26}Ne excitation energy above S_n

Final ^{25}Ne state		Experiment		Statistical decay		
Label	J^Π	Pb	Al	$L = 1$	$L = 2$	$L = 3$
(gs)	$1/2^+$	$5_{-5}^{+17}\%$	$< 10\%$	40%	28%	22%
(I)	$5/2^+ + 3/2^+$	$66\% \pm 15\%$	$95_{-15}^{+5}\%$	55%	67%	75%
(II)	$3/2^-$	$35\% \pm 9\%$	$5_{-5}^{+6}\%$	5%	4%	3%

Table IV.5: Experimental branching ratio compared to statistical model for a given ^{26}Ne transition multipolarity to a given excited state in ^{25}Ne compared to experiment.

that the decay is not statistical, which is not surprising for a light nucleus. No predictions of the direct decay of pygmy states exist from the previously mentioned microscopic models. Future comparisons with our data should be a strong test for these models.

IV.3.5 Estimation of the direct break-up

It has been established for weakly bound nuclei like ^{11}Be , that the large cross sections observed for the Coulomb dissociation can be explained by a so-called *direct break-up* model [Nakamura 97]. Due to a large overlap between the tail of the valence neutron(s) wave function and the continuum, a non-resonant transition is possible to the continuum. The direct breakup strength distribution is extremely sensitive to the spatial extension of the single-particle wave function, and thus to the angular momentum of the valence neutron. It however decreases with increasing the binding energy. In order to estimate the direct break-up contribution to our experiment we performed two calculations of absolute break-up cross-sections. The first one is based on the resolution of the Time Dependant Schrödinger Equations (TDSE) and the second is based on the first order perturbation theory.

- (i) The Time Dependant Schrödinger Equation (TDSE) method as developed by Lacroix *et al.* [Lacroix 99] is a semi classical calculation. Each

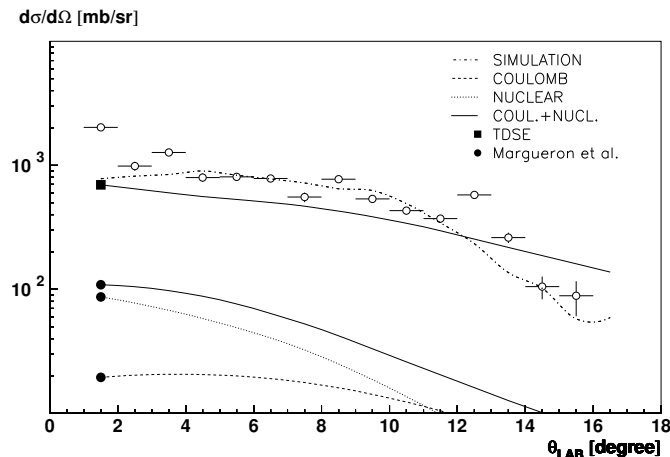


Figure IV.24: Neutron angular distribution from $^{26}\text{Ne} \rightarrow ^{25}\text{Ne} + n$ channel for lead target. Experimental results are displayed in open circle and are compared to two calculations: TDSE in close square and Margueron *et al.* in closed circle. For this last the Coulomb contribution (dashed line) and the nuclear contribution (dotted line) as well as their sum (solid line) is plotted. In dot-dash line is displayed the result of simulations of an isotropic emission of neutron in the center-of-mass system.

of the two nuclei involved in the reaction are initially supposed to be described properly by an independent particle model. The two nuclei of mass A_t (Target) and A_p (Projectile) are initially far away from one another and are prepared in their respective ground state. The projectile is initially boosted according to a given beam energy and impact parameter, and follows a trajectory of classical Rutherford scattering. A cut-off below the impact parameter corresponding to the grazing angle is set, since no rearrangement of the potential is performed. The dynamical evolution of the system is reduced to the set of evolutions of its $A_t + A_p$ single-particle wave-packets $|\phi_i\rangle$, via $A_t + A_p$ set of Schrödinger equations. We supposed here that the valence neutron is located in the $2s_{1/2}$ orbital and that the spectroscopic factor equals to one. Results are presented in the Fig. IV.24 with closed square (■) marker.

(ii) The second theoretical approach, developed by Margueron *et al.* [Margueron 02, Margueron 03], uses the first order perturbation theory for the Coulomb amplitude and an eikonal approach for the nuclear breakup. The formalism includes the effect of the nuclear distortion of the neutron wave function which is summed coherently with the Coulomb amplitude. The breakup amplitude hence becomes the sum of three terms: one has the form of the nuclear breakup in the eikonal model, one the form of the Coulomb breakup in first order perturbation theory and the third term mixes the Coulomb and the nuclear potentials (interferences). In this model, the probability to generate a direct break-up exponentially decreases below the strong absorption radius. The results supposing again a $2s_{1/2}$ neutron and a spectroscopic factor of one, are presented in the Fig. IV.24 with closed circle (\bullet) marker.

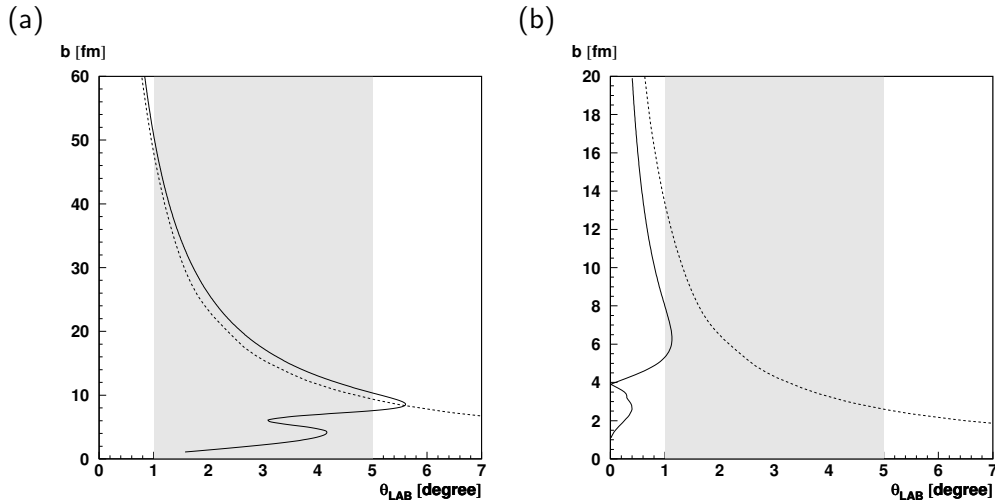


Figure IV.25: Classical calculation (solid line) of the impact parameter function of the scattering angle in laboratory system, for 55 MeV/n ^{26}Ne impinging: (a) on lead target (b) on aluminum target. In comparison the dashed line represents the pure Rutherford scattering. The shaded area stands for the silicon detector angular acceptance.

As previously described, these models are impact parameter dependent. We hence performed a classical estimation, based on an optical potential, of the impact parameter as function of the deviation angle for 55 MeV/n ^{26}Ne impinging on lead target and aluminum target, displayed in figures Fig. IV.25 (a) and Fig. IV.25 (b) respectively. We also represent on this figure the angular acceptance of the silicon detector (shaded area). We see that in case of lead target, our setup allows us to look essentially to the reactions above the grazing angle. On the other hand, for kinematic reasons, the impact parameter in aluminum is smaller than the sum of the two radii and the physics observed is essentially inelastic.

Results

For aluminum target, the experimental impact parameters are lower than the strong absorption radius below which these approaches are not valid. Therefore, no conclusion can be drawn here.

Concerning the angular distribution in lead target, the calculated amplitudes by the two models differ. TDSE gives an amplitude almost comparable with our data whereas the results predicted by the eikonal approach is ~ 10 times smaller than the experiment. In both cases the absolute cross section is an upper limit, and several structure effects which are not presently taken into account, should decrease the amplitude. The ^{25}Ne is theoretically generated in its ground state, which is not what is observed experimentally (Fig. IV.17). Taking into account the excited states in ^{25}Ne will decrease the cross section. The calculations has been performed for one neutron in the $2s_{1/2}$ since, according to a recent experiment [Obertelli 05a], the ^{26}Ne ground state configuration is essentially two neutrons in the $2s_{1/2}$. Experimentally the direct break-up seems to be dominant in odd nuclei [Adrich 05a] and wicker in even-even nuclei, and in the calculations the effect of the pairing is not taken into account. The calculations tend to show that direct break-up cross section is a small contribution to the experiment but structure effects need to be taken into account to improve the theoretical calculations.

IV.3 ^{26}Ne excitation energy above S_n

Finally, the neutron angular distribution as obtained from the simulation of a resonance break-up at 9 MeV excitation energy, taking into account the possible ^{25}Ne excited states, with an isotropic emission of the neutron in the center of mass reproduce the shape of the experimental data (dot-dash line in Fig. IV.24). However the shape is essentially due to kinematical effects and cannot be reliably used to distinguish between reaction mechanisms.

Summary & Conclusion

The elastic and inelastic scattering of ^{26}Ne on $^{\text{nat}}\text{Pb}$ and ^{27}Al target has been studied at the RIKEN Accelerator Research Facility. The experimental setup was designed for a complete kinematics measurement, in order to apply the invariant mass method for excitation energies above the particle emission threshold. It hence included a charged fragment hodoscope, a γ -ray array and a neutron detector wall.

Below the one neutron emission threshold, we measured the γ -decay from the 2_1^+ and 0_2^+ states at 2018 keV and 3691 keV respectively. We have extracted a $B(E2, 0_1^+ \rightarrow 2_1^+)$ value of $87 \pm 13 \text{ e}^2\text{fm}^4$, smaller than the one previously published by Pritychenko *et al.* The raw experimental results from the two studies are comparable but the discrepancy is explained by the different analysis of the data. In the case of Pritychenko *et al.* the nuclear part of the excitation was neglected.

The excitation energy spectrum of ^{26}Ne between the one neutron and the two neutron emission thresholds was reconstructed using the invariant mass method in the $^{25}\text{Ne}+n$ decay channel. A sizable amount of strength was observed within this interval. The multipole decomposition of the corresponding scattering angular distribution from the lead target shows the presence of E1 strength. We extracted a Coulomb deformation parameter corresponding to a reduced transition probability of $B(E1, \uparrow) = 0.544 \pm 0.183 \text{ e}^2\text{fm}^2$ and a fraction of the Thomas-Reiche-Kuhn energy weighted sum-rule of $5.2 \pm 2.1\%$

between $E^* = 8$ and 10 MeV. The results are compared to several theoretical predictions and the best agreement was found with the QRRPA calculation of Cao and Ma [Cao 05b].

Furthermore, the method used allowed us to study for the first time the decay pattern of the excited “pygmy” states. The branching ratios to the final ^{25}Ne states exhibit significant differences for the reactions on lead and aluminum target, which confirms that different multipolarities have been excited. A comparison with a Hauser-Feshbach calculation indicates that the decay is non statistical. Interestingly, the ^{25}Ne ground state is almost not fed in both cases. These results give a handle on the microscopic structure of the low-lying strength and this constitutes a strong constraint for the theoretical models. Indeed, all the mean-field calculations predict a redistribution of strength towards low energies in neutron rich nuclei, but the predicted wave functions strongly differ.

We demonstrated that intermediate energy reaction are a powerful spectroscopic tool. In particular the angular distributions can be measured with sufficient accuracy to perform a multipole decomposition analysis. The coincident γ -ray measurement allows us to extract branching ratios to the levels of the daughter nucleus. The direct break-up contribution was also investigated theoretically with the conclusion that it was not significant.

It would be important to investigate the states above the two neutron emission threshold. However the level density in the daughter nucleus become higher and the γ -detection may become a limitation. Furthermore the neutron acceptance was relatively low in our setup and its detection not dedicated to more than one neutron.

Giant Resonances being a general property of nuclei, it will be interesting in the future to investigate the redistribution of strength in a systematic way. A first case would be the predicted pygmy resonance in ^{28}Ne [Cao 05b]. An experimental ^{27}Ne level scheme was recently proposed [Obertelli 05a] but the very small one neutron emission threshold ($S_n = 1.4$ MeV) would necessitate in the measurement of the two neutron decay channel. Low ly-

ing dipole strength in neutron rich oxygen isotopes was already measured [Leistenschneider 01] using high energy beam. It would be interesting to investigate their decay branching ratios to the various states the daughter nuclei. The new information provided would be useful to constrain the theoretical calculations. For nuclei on the neutron poor side, calculations predicting pygmy resonances have been performed for example in ^{32}Ar [Ma 97, Paar 05]. Experimentally, such secondary beams have become available [Yamada 01] making these experiments feasible using a large charged particle array like MUST2.

The new facilities at Riken (RIBF and Big-RIPS) which will be able to generate heavier beam at few hundreds of MeV/n might be a good compromise between the high Coulomb cross section and the possibility to perform multipole decomposition based on angular distributions. A dedicated experimental setup, able to handle a neutron multiplicity greater than one with a good efficiency and to measure the γ -rays with accuracy, should however be constructed.

Appendix A

Extraction of ^{26}Ne excitation energy distribution, simulation test case

We presented in Sec. IV.3.1 our method to build the ^{26}Ne excitation energy distribution using a simplified case. The starting point of the method is to reconstruct the relative energy spectra for the $^{25}\text{Ne}+n$ inclusive events and for the $^{25}\text{Ne}+n+\gamma_i$ coincidence, for each γ_i transition in ^{25}Ne . In the following, we present the method, using a simulation, for a more general case corresponding to the experiment.

The level scheme for ^{25}Ne is displayed in Fig. IV.16. The two levels at 1.7 MeV and 2 MeV are considered degenerated since their energy difference is significantly smaller than the excitation energy resolution (~ 800 keV). Three levels in ^{25}Ne hence remain: the ground state (gs) and two excited states at ~ 1.9 MeV(I) and at 3.3 Me (II) respectively. They can decay *via* the emission of three different gammas of 1882 keV, 1613 keV and 3316 keV, labeled $\bar{\gamma}^{(1)}$, $\gamma^{(2)}$ and $\gamma^{(3)}$ respectively. For details on the simulation, please refer to Appendix B.

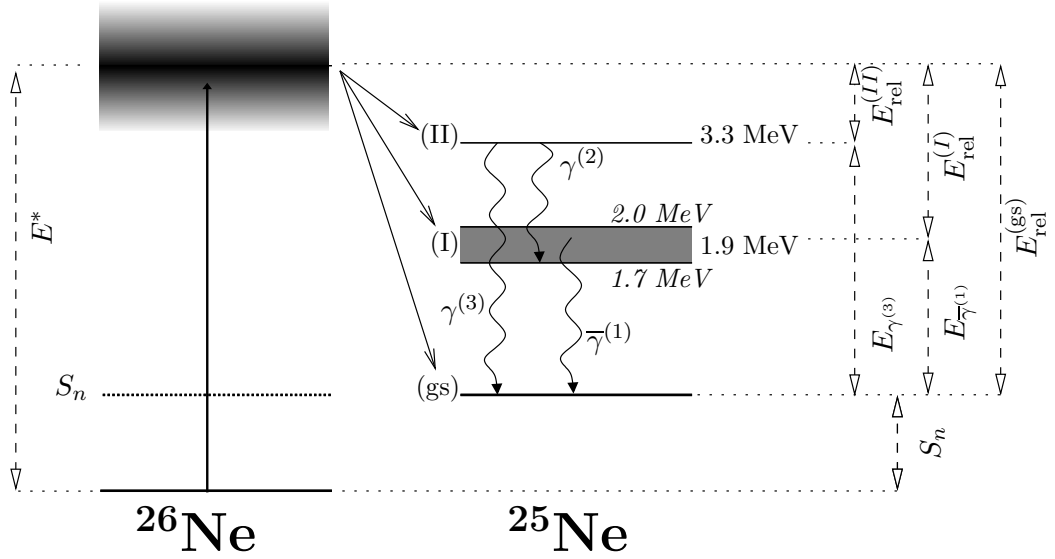


Figure A.1: Retained scheme of decay from ^{26}Ne excited state above the one neutron emission threshold *via* $^{25}\text{Ne}+n$ channel. We present here a simplified level scheme for ^{25}Ne where the two first states are degenerated. We also illustrate the different components involved in the excitation energy reconstruction.

In analogy with the simplified case of Sec. IV.3.1, the contribution to the excitation energy spectrum of the decay to the ground state (gs), the first (I) and the second (II) ^{25}Ne excited state read:

$$[E^{(II)}] = [E_{rel}|\bar{\gamma}(2)]/\epsilon_{\bar{\gamma}(2)} + [E_{rel}|\gamma(3)]/\epsilon_{\gamma(3)} \leftrightarrow S_n \leftrightarrow E_{\gamma(3)} \quad (\text{A.1})$$

$$[E^{(I)}] = [E_{rel}|\bar{\gamma}(1)]/\epsilon_{\bar{\gamma}(1)} - [E_{rel}|\bar{\gamma}(2)]/\epsilon_{\bar{\gamma}(2)} \leftrightarrow S_n \leftrightarrow E_{\bar{\gamma}(1)} \quad (\text{A.2})$$

$$[E^{(gs)}] = [E_{rel}] - [E_{rel}|\bar{\gamma}(1)]/\epsilon_{\bar{\gamma}(1)} - [E_{rel}|\gamma(3)]/\epsilon_{\gamma(3)} \leftrightarrow S_n \quad (\text{A.3})$$

where $[\dots]$ stands for spectrum and $[E_{rel}|\gamma^i]/\epsilon_{\gamma^i}$ is the relative energy spectrum in coincidence with γ^i and divided by the corresponding detection efficiency ϵ_{γ^i} . According to Sec. III.2.2 Geant 3 code [Brun 86] we reproduce the γ -ray peak efficiency. But in order to take into account the correlation

State	Branching ratio	γ -ray composition
(gs)	40%	—
(I)	40%	50% 1.7 MeV + 50% 2.0 MeV
(II)	20%	75% (1.7+1.6 MeV) + 25% 3.3 MeV

Table A.1: Branching ratio from the ^{26}Ne excited state to difference state of the ^{25}Ne for the lead and the aluminum target.

between the gamma-ray efficiency and the other efficiency and acceptances (silicon detectors and neutron wall) we simulated the reaction of a excited ^{26}Ne at 9 MeV decaying by neutron emission. We tested the $L = 1$ and $L = 2$ angular distribution cases.

We made the same supposition concerning the level scheme and the decay to ^{25}Ne as in Sec. IV.3.3. We re-displayed here its illustration. We suppose the branching ratios displayed in Table A.1. Note that that we simulated the decay from the non degenerated 1.7 MeV *and* 2.0 MeV.

We adjusted the ϵ_{γ^i} γ -ray efficiency in order to reproduce a peak at $E^* = 9 \text{ MeV}$ and suppress the background that can be generated by a bad efficiency estimation. We observed that wrong values of of the efficiency ϵ_{γ^i} induce distortions of the reconstructed excitation energy. It was however encouraging to note that the γ -peak efficiency obtained was very closed to the one obtained in Sec. III.2.2. We could also adjust the mixing between the unresolved 1.6 MeV and the 1.7 MeV gamma-rays, which also turned to be very closed to our independent contribution analysis.

Results a presented in Fig. A.2 for lead and Fig. A.3 for aluminum target. We checked that the same ratios as in Table A.1 are found after reconstruction. One can note that the value displayed in Fig. A.2 and Fig. A.3 show some discrepancy we could no perfectly suppress without generating some distortion in the shape of the excitation energy spectrum. The number of events was however conserved at the end of our analysis process.

Extraction of ^{26}Ne excitation energy distribution, simulation test case

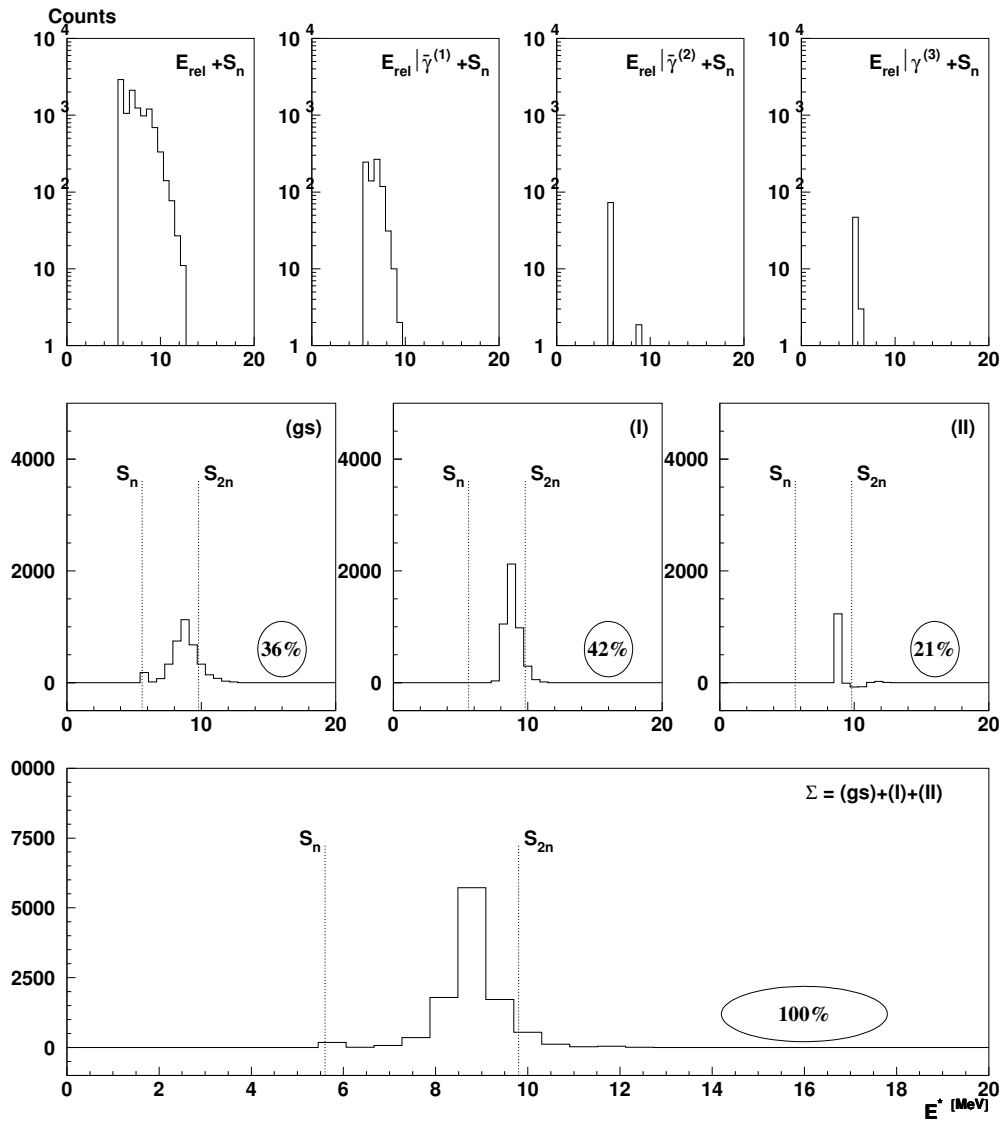


Figure A.2: Simulation on lead: Relative energy spectrum, shifted with the one neutron emission threshold S_n . The first row presents the results for inclusive and exclusive spectra (see text). The second row shows the different components of the excitation energy spectrum for each decay path (see text). The last panel is the sum of the previous three histograms.

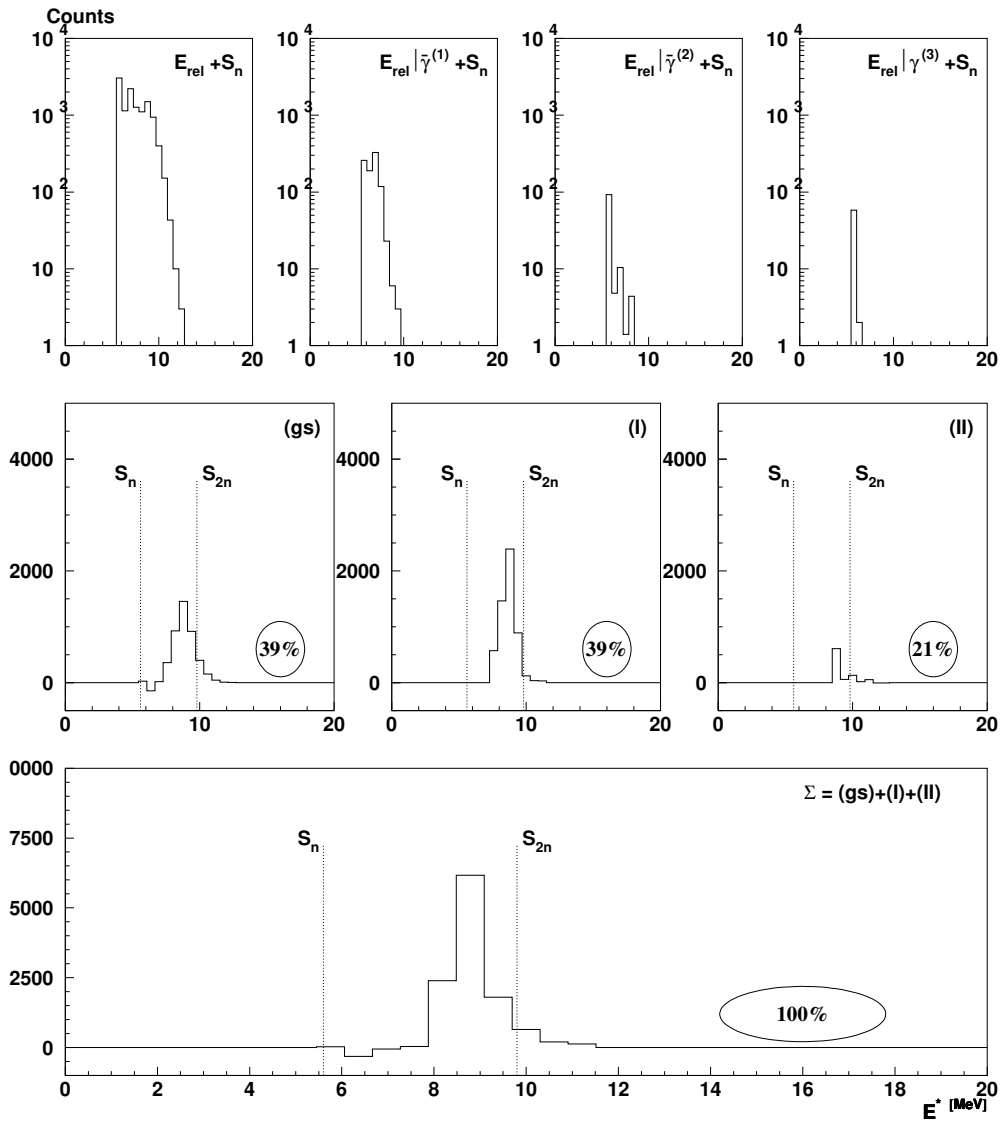


Figure A.3: Simulation on aluminum: target. Relative energy spectrum, shifted with the one neutron emission threshold S_n . The first row presents the results for inclusive and exclusive spectra (see text). The second row shows the different components of the excitation energy spectrum for each decay path (see text). The last panel is the sum of the previous three histograms.

Appendix B

Description of the simulation code

All simulations were performed using the Geant 3 [Brun 86] package, a system of detector description and simulation tools written in Fortran and developed at CERN. It allows to define and track various particles (like gammas, neutrons, muons, heavy ions, ...) and monitor their interaction with matters and especially those of detectors are made from. In further sections we will detail the procedures employed to simulate the whole experiment, from the experimental beam tracking to the gamma detector array DALI, the silicon hodoscopes and the neutron wall, successively. An overview of the experimental setup as computed by Geant 3 is displayed in Fig. B.1.

B.1 Description of the simulation code

B.2 Beam simulation

Experimental down scaled beam events is used as input to generate the momentum of the incident particles. Experimental observables input in simula-

B.2 Beam simulation

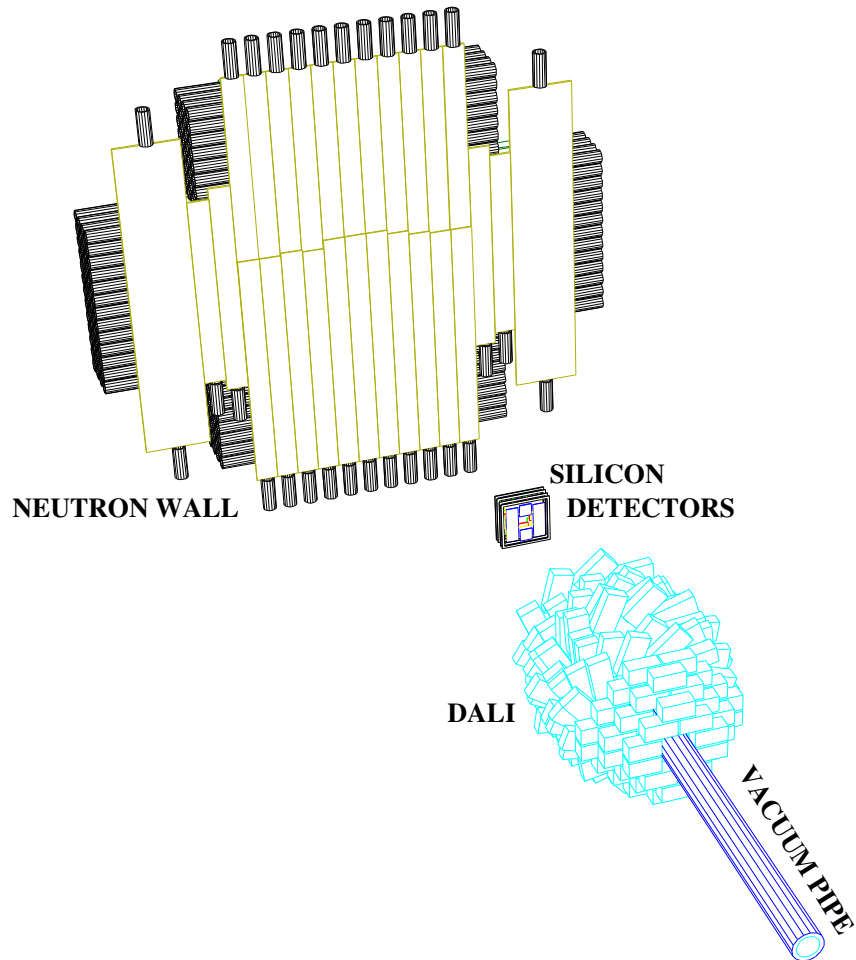


Figure B.1: Experimental setup as computed by Geant 3

tion are thus position in the first PPAC (PPACa) and in the second PPAC (PPACb) as well as the velocity β_{beam} of the beam. We simulate also the conditions with which the beam arrives on the targets *i.e.* the ^{26}Ne ions comes from a vacuum pipe, cross a kapton window of $25\ \mu\text{m}$ and air before impinging on the target.

B.3 Inelastic scattering and decay

At that point it is necessary to compute the specific reactions that occur in the target. In a first step we decide where the reaction occurs, by drawing lots for the reaction thickness. We let Geant 3 propagate the nuclei till this thickness, where we successively apply an elastic scattering followed by a break-up.

B.3.1 Inelastic scattering

From external reaction codes like ECIS [Raynal 97] we obtain the angular distribution of the inelastic scattering, for a given excitation energy. At the reaction point, we hence modify the mass of the incoming nuclei, in order to simulate its excitation, and its direction to simulate the scattering.

B.3.2 Decay

We suppose that the break-up occurs just after excitation. We randomly determine in the center of mass frame the direction of the resulting particles, *e.g.* ^{25}Ne and neutron in case of ^{26}Ne break-up. If excited states of the daughter nuclei are kinetically reachable, we allow with a given branching ratio to populate these states. The mass of decay particles is thus increased by their excitation energy.

In the case of daughter nuclei decaying by gamma, we simulate immediately after breakup the emission of the gamma(s), in the center of mass of the daughter nucleus. Note that if a cascade exists, it is systematically generated.

B.3.3 Illustration

The main simulated case is the coulomb excitation of ^{26}Ne followed by break-up in ^{25}Ne and one neutron. ^{25}Ne can be in excited state and emits γ .

B.4 DALI simulation

In order to test our inputs, we rebuild both the angular distribution of ^{26}Ne inelastic scattering and the invariant mass from position and energy of the ^{25}Ne and the neutron, recorded just after break-up (and not using the simulation of the detection). The reconstruction program is exactly the one used for experimental data and the results shown in Fig. B.2 proves that the consistency between it and the simulation.

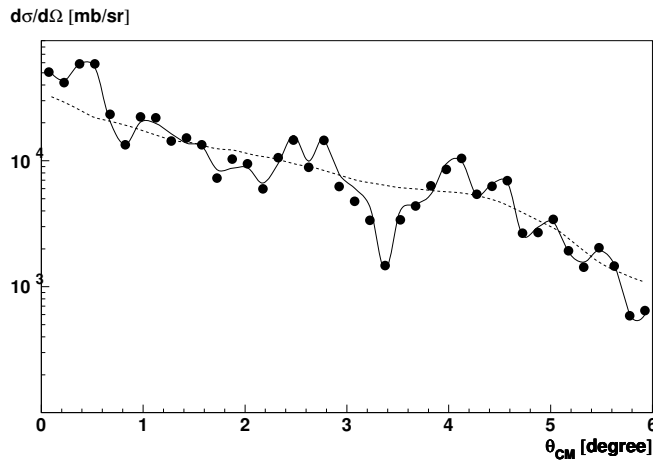


Figure B.2: Arbitrary ECIS 97 $^{26}\text{Ne}+^{208}\text{Pb}$ angular distribution (plain line) compared with the reconstruction just after break-up into $^{25}\text{Ne}+n$ (filled circles) as given by the simulation. The dotted line is obtain after simulation of the detection and illustrates the effect if the latter.

B.4 DALI simulation

DALI I & II are made from different shape and type of NaI crystal. The exact geometry and composition of each detector as well as their real positions in the whole detector was enter in the simulation. We also included the aluminum plate that supported the crystal. Geant 3 can not deal with intrinsic resolutions of detectors. By consequence, it was experimentally measured for each crystal (see Sec. III.2.5) and input to the simulation. The obtained

the energy distribution and the peak-efficiency were compared to experiment with a very good agreement. We display in Fig. B.3 (a) and Fig. B.3 (b) the figures already presented in Sec. III.2. In Fig. B.3 (a) the simulation of ^{60}Co source, with the corresponding intense 1173 and 1333 keV γ -ray emission is well reproduced by our simulation if we add the room background, non generated by Geant 3. Concerning the efficiency, we reproduce the experimental measurement from standard source ^{22}Na , ^{60}Co , ^{137}Cs , and the mixture of Am-Be, with a $\sim 10\%$ error, see Fig. III.2.2.

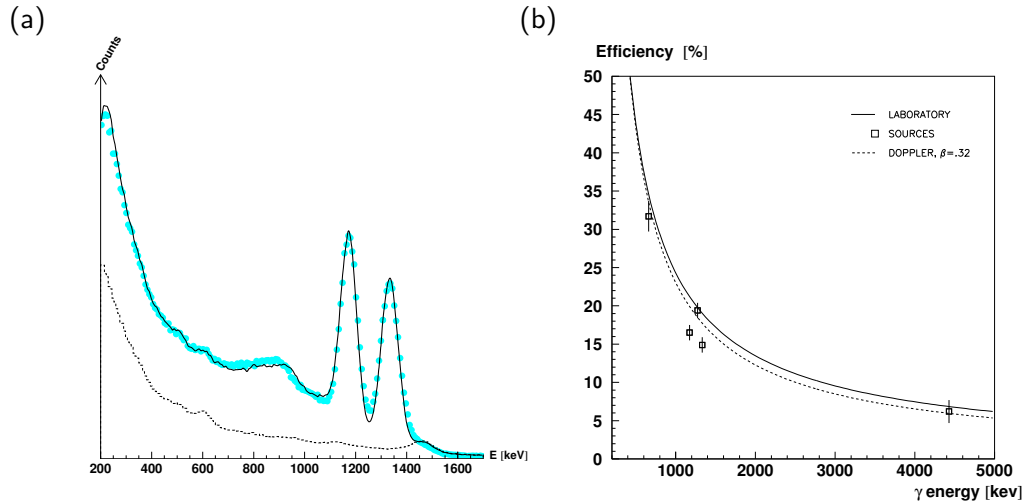


Figure B.3: (a) Deposited energy from 1173 and 1333 keV γ emitted from ^{60}Co standard source (\bullet) the whole DALI array, compared with simulation by Geant 3 (solid line). The measured background (dashed line) was added to simulation. (b) Evaluated DALI total efficiency for source emitter at rest (solid line) in addition to experimental values (\square), see details for experimental values in Sec. III.2.2. Efficiency (in %) is well reproduced by $8.7 \cdot 10^3 / E_\gamma^{0.87}$ with E_γ in keV. The dashed line is obtained by simulating a source emitting at velocity $\beta = 0.32$.

B.5 Silicon hodoscope simulation

The exact position of the silicons (strip and SiLi) is entered in simulations. However there are mainly two equivalent ways to simulate the resolution in position due to strip size of 5 mm. Either by dividing each 5 cm square silicon by 10 strips or by recording the position given by the simulation modulo .5 mm. For simplicity and since the size of the strip is negligible, we used the latter method.

We can check the accuracy between silicon thickness and position in experiment with the one entered in Geant 3 by superimposing the two E - ΔE distributions, where in both cases ΔE is the sum of deposited energies in silicon strip layer 1 (X) and 2 (Y) and E the sum of ΔE and the deposited energy in last SiLi layer. See for illustration Fig. B.4.

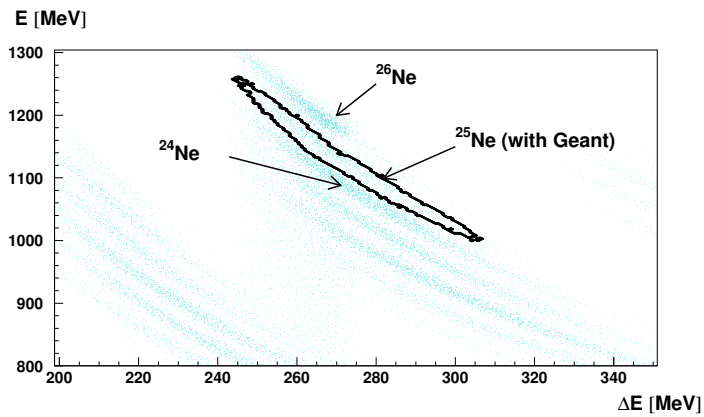


Figure B.4: Test on Geant 3 accuracy reproducing energy loss in silicon. Here the black contour is obtained from ^{25}Ne from ^{26}Ne break-up. It is superimposed to experimental results

In the same way, we compared the particle identification as obtained from the 1D projection. Experimentally with ^{25}Ne beam at 55 and 60 MeV/n, we achieved a mean at $A = 25.06$ ($\sigma_A/A = 0.91\%$) and $A = 25.03$ ($\sigma_A/A = 0.95\%$) respectively. For simulated data by Geant 3, which include both position of silicon hodoscope and resolution, we obtain $A = 24.93$ ($\sigma_A/A =$

0.94%), which is enough for our purpose.

B.6 Neutron wall simulation

Geant 3 deals with neutron through GHEISHA and/or FLUKA interface. But, experimental tests reported in [Celano 97] show difficulties to reproduce detection properties for ~ 50 MeV neutrons, partly because of the lack of data on the neutron kinematics on carbon at these energies. On the other hand results from CECIL code [Cecil 79] were tested good with the neutron plastics used in this experiment [Fukuda 04]. We thus decided to include CECIL simulated efficiency in Geant 3. Note also that Geant, in its version 3, can not handle light output.

For safety, we decided to make the neutron plastic *empty*, with vacuum as material. In case of a neutron interacting a plastic, according to its kinematic energy and following the efficiency dependences given by CECIL, we draw a lot on its probable detection. We hence did not simulate the neutron scattering in the detector at the origin of the cross talk. This is acceptable as long as we do not need to simulate the detection of more than one neutron.

Appendix C

Relativistic Kinematics

Most of the following equations are extracted from [Michalowicz 64].

C.1 Notations, Basic relations

C.1.1 Notations

$$m_i : \text{rest mass of particle } i \quad (\text{C.1})$$

$$E_i : \text{total energy of particle } i \quad (\text{C.2})$$

$$\vec{p}_i : \text{momentum of particle } i \quad (\text{C.3})$$

$$T_i : \text{kinetic energy of particle } i \quad (\text{C.4})$$

$$\vec{\beta}_i : \text{velocity of particle } i \quad (\text{C.5})$$

$$\gamma_i : \text{relativistic } \gamma \text{ of particle } i \quad (\text{C.6})$$

$$I : \text{Invariant Mass} \quad (\text{C.7})$$

C.1.2 Basic (one body) relations

$$\vec{\beta} = \vec{p}/E \quad (\text{C.8})$$

$$\gamma = \frac{1}{1 - |\vec{\beta}|^2} = \frac{1}{1 - \beta^2} \quad (\text{C.9})$$

$$|\vec{p}|^2 \equiv p^2 = E^2 - m^2 = T(T + 2m) \quad (\text{C.10})$$

$$T = E - m = \frac{p^2}{\sqrt{p^2 + m^2} + m} \quad (\text{C.11})$$

$$E = m\gamma \quad (\text{C.12})$$

$$\vec{p} = m\gamma\vec{\beta} \quad (\text{C.13})$$

$$T = m(\gamma - 1) = m \frac{\beta^2 \gamma^2}{1 + \gamma} \quad (\text{C.14})$$

C.2 Two-body reaction: Center of Mass (CM) frame

Here after observables calculated in CM frame will be denoted with a star (\star)

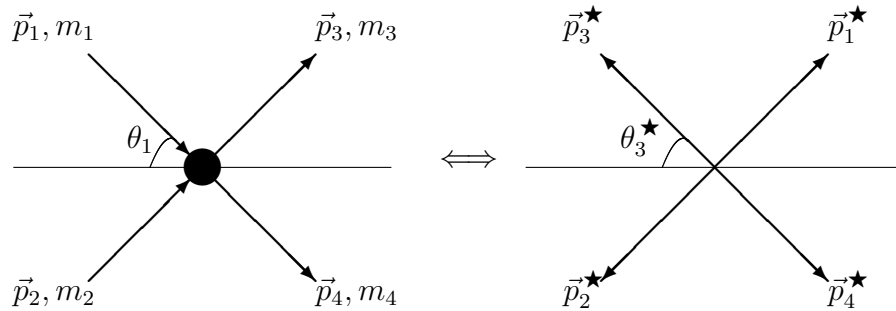


Figure C.1: Illustration of the notations in an unspecified (e.g. laboratory) frame (Right) and in center of mass system (Left).

C.2.1 Notations

$$M = \frac{m_1 m_2}{m_1 + m_2} \quad : \quad \text{reduced mass} \quad (\text{C.15})$$

$$E_T = E_1 + E_2 = E_3 + E_4 \quad : \quad \text{total energy} \quad (\text{C.16})$$

$$\vec{p}_T = \vec{p}_1 + \vec{p}_2 = \vec{p}_3 + \vec{p}_4 \quad : \quad \text{CM momentum} \quad (\text{C.17})$$

$$\Rightarrow \vec{p}_T^\star = \vec{0} \quad (\text{by definition}) \quad (\text{C.18})$$

$$\vec{B} \quad : \quad \text{CM velocity} \quad (\text{C.19})$$

$$\Gamma = \frac{1}{1 - B^2} \quad : \quad \text{CM relativistic gamma} \quad (\text{C.20})$$

C.2.2 Relations

$$\vec{B} = \frac{\vec{p}_1}{E_1 + m_2} \quad (\text{C.21})$$

$$E_T^\star = E_T / \Gamma \quad (\text{C.22})$$

$$E_3^\star = \frac{E_T^{\star 2} + m_3^2 - m_4^2}{2E_T^\star} = \frac{E_T^2 + \Gamma^2(m_3^2 - m_4^2)}{2\Gamma E_T} \quad (\text{C.23})$$

$$E_4^\star = \frac{E_T^{\star 2} + m_4^2 - m_3^2}{2E_T^\star} = \frac{E_T^2 + \Gamma^2(m_4^2 - m_3^2)}{2\Gamma E_T} \quad (\text{C.24})$$

$$p_i^{\star 2} = E_i^{\star 2} - m_i^{\star 2} \quad \text{with } i = 3 \text{ or } 4 \quad (\text{C.25})$$

$$\vec{\beta}_i^\star = \vec{p}_i^\star / E_i^\star \quad \text{with } i = 3 \text{ or } 4 \quad (\text{C.26})$$

$$\chi_i = B / \beta_i^\star \quad \text{with } i = 3 \text{ or } 4 \quad (\text{C.27})$$

$$\tan \theta_i = \frac{1}{\Gamma} \frac{\sin \theta_i^\star}{\cos \theta_i^\star + \chi_i} \quad \text{with } i = 3 \text{ or } 4 \quad (\text{C.28})$$

$$E_i = E_i^\star \Gamma (1 + B \beta_i^\star \cos \theta_i^\star) \quad \text{with } i = 3 \text{ or } 4 \quad (\text{C.29})$$

C.3 Two-body decay

The center of mass system coincides here with the rest frame of the decaying particle.

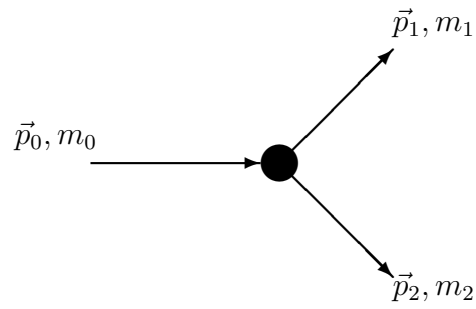


Figure C.2: Two body decay

$$E_1^\star = \frac{m_0^2 - m_2^2 + m_1^2}{2m_0} \quad (\text{C.30})$$

$$\text{or } E_2^\star = \frac{m_0^2 - m_1^2 + m_2^2}{2m_0} \quad (\text{C.31})$$

$$|\vec{p}_1^\star| = |\vec{p}_2^\star| \quad (\text{C.32})$$

$$(\text{C.33})$$

C.3.1 Doppler Effect

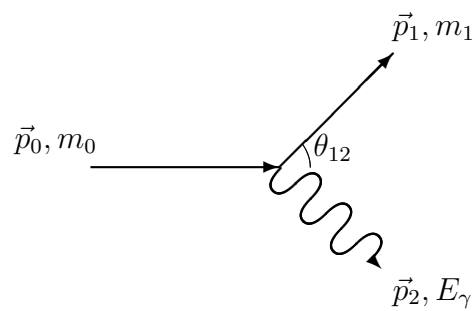


Figure C.3: Doppler Effect

C.4 Three-body breakup

It is a special case of two-body decay where one of the particle (e.g. number (2)) is a photon.

$$E_2 = T_2 = p_2 = E_\gamma \quad (\text{C.34})$$

$$E_\gamma = E_\gamma^\star \gamma_1 (1 - \beta_1 \cos \theta_{12}) \quad (\text{C.35})$$

$$E_\gamma^\star = E_\gamma \gamma_1 (1 + \beta_1 \cos \theta_{12}) \quad (\text{C.36})$$

$$\theta^\star = \quad (\text{C.37})$$

$$(\text{C.38})$$

C.4 Three-body breakup

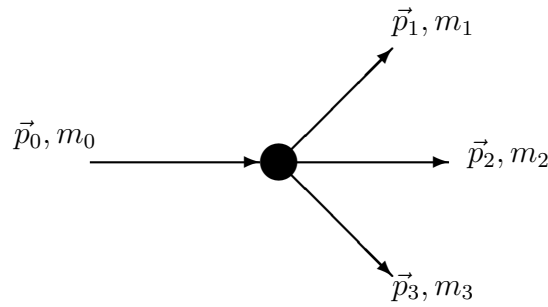


Figure C.4: Three body decay

Bibliography

- [Adrich 05a] P. Adrich. *Observation of Pygmy and Giant Dipole Resonances in ^{132}Sn and neighboring mass isotopes*. PhD thesis, Jagiellonian University, 2005.
- [Adrich 05b] P. Adrich *et al.* *Evidence for Pygmy and Giant Dipole Resonances in ^{130}Sn and ^{132}Sn* . Phys. Rev. Lett., vol. 95, page 132501, 2005.
- [Alder 75] K. Alder & A. Winther. *Electromagnetic excitation*. North-Holland Pub. Comp., 1975.
- [Alhassid 82] Y. Alhassid, M. Gai & G. F. Bertsch. *Radiative Width of Molecular-Cluster States*. Phys. Rev. Lett., vol. 49, pages 1482–1485, 1982.
- [Aumann 98] T. Aumann. *Multiphonon giant resonances in nuclei*. Annu. Rev. Nucl. Part. Sci., vol. 48, pages 351–399, 1998.
- [Baba 01] H. Baba *et al.* *Development of New Data Acquisition System Babar/DAQ for Nuclear Physics Experiments*. RIKEN Accel. Prog. Rep., vol. 34, page 221, 2001.

Bibliography

- [Baldwin 47] G. C. Baldwin & G. S. Klaiber. *Photo-Fission in Heavy Elements*. Phys. Rev., vol. 71, no. 1, pages 3–10, 1947.
- [Barrette 88] J. Barrette *et al.* *Coulomb excitation of giant resonances in ^{208}Pb by $E = 84$ MeV/Nucleon ^{17}O projectiles*. Phys. Lett. B, vol. 209, pages 182–186, 1988.
- [Bertulani 88] C. A. Bertulani & G. Baur. *Electromagnetic processes in relativistic heavy ion collisions*. Phys. Rep., vol. 163, pages 299–408, 1988.
- [BICRON] BICRON. *Premium Plastic Scintillators Product Data Sheet*. Also available as <http://www.detectors.saint-gobain.com/Media/Documents/S00000000000000000003/pdsbc400416.pdf>.
- [Blumenfeld 99] Y. Blumenfeld *et al.* *MUST: A silicon strip detector array for radioactive beam experiment's*. Nucl. Ins. and Meth. A, vol. 421, pages 471–491, 1999.
- [Bohr 98] A. Bohr & B.R. Mottelson. *Nuclear structure*. World Scientific Publishing Comp., Inc., 1998.
- [Bothe 37] W. Bothe & W. Gentner. *Z. Phys.*, vol. 71, page 236, 1937.
- [Broglia 91] R. A. Broglia & A. Winther. *Heavy ion reactions*. Addison Wesley Pub. Co., 1991.
- [Brun 86] R. Brun *et al.* *GEANT 3*. CERN DD/EE/84-1, 1986.

- [Brun 89] R. Brun *et al.* *PAW, a general-purpose portable software tool for data analysis and presentation*. CERN-DD-89-17, 1989.
- [Buenerd 84] M. Buenerd *et al.* *Elastic and inelastic scattering of carbon ions at intermediate energies*. Nucl. Phys. A, vol. 424, pages 313–334, 1984.
- [Cao 05a] L.-G. Cao & Z.-Y. Ma. Private communication, 2005.
- [Cao 05b] L.-G. Cao & Z.-Y. Ma. *Low-lying dipole modes in $^{26,28}\text{Ne}$ in the quasiparticle relativistic random phase approximation*. Phys. Rev. C, vol. 71, page 034305, 2005.
- [Cecil 79] R. A. Cecil *et al.* *Improved predictions of neutron detection efficiency for hydrocarbon scintillators from 1 MeV to about 300 MeV*. Nucl. Ins. and Meth., vol. 161, pages 439–447, 1979.
- [Celano 97] L. Celano *et al.* *Performance of a long plastic scintillator detector for neutron studies*. Nucl. Ins. and Meth. A, vol. 392, pages 304–309, 1997.
- [Dufour 86] J.P. Dufour *et al.* *Projectile fragments isotopic separation: Application to the lise spectrometer at GANIL*. Nucl. Ins. and Meth. A, vol. 248, pages 267–281, 1986.
- [Fermi 24] E. Fermi. Z. Phys., vol. 29, page 315, 1924.
- [Fukuda 04] N. Fukuda. *Break-up reaction of the One-neutron Halo Nucleus ^{11}Be* . PhD thesis, University of Tokyo, 2004.

Bibliography

- [Goldhaber 48] M. Goldhaber & Teller E. *On Nuclear Dipole Vibrations*. Phys. Rev., vol. 74, no. 9, pages 1046–1049, 1948.
- [Goulding 85] F. S. Goulding. *Treatise on Heavy-Ion Science*, volume 7. Bromley, D. A., Plenum, New York, 1985.
- [Hagiwara 02] K. Hagiwara *et al.* *Review of Particle Physics*. Physical Review D, vol. 66, pages 010001+, 2002.
- [Imai 04] N. Imai. *Quadrupole Collectivity of ^{16}C* . PhD thesis, University of Tokyo, 2004.
- [Iwasaki 01] H. Iwasaki. *In-beam gamma spectroscopy of ^{12}Be with inelastic scattering*. PhD thesis, University of Tokyo, 2001.
- [Iwasaki 05] H. Iwasaki *et al.* *Quadrupole collectivity of ^{28}Ne and the boundary of the island of inversion*. Phys. Lett. B, vol. 620, pages 118–124, 2005.
- [Jackson 99] J.D. Jackson. *Classical electrodynamics*. John Wiley and Sons, 1999.
- [Khan 00] E. Khan & N. V. Giai. *Low-lying 2^+ states in neutron-rich oxygen isotopes in quasiparticle random phase approximation*. Phys. Lett. B, vol. 472, pages 253–257, 2000.
- [Khan 05] E. Khan *et al.* Private communication, 2005.
- [Khoa 95] D. T. Khoa *et al.* *Equation of State for Cold Nuclear Matter from Refractive $^{16}\text{O} + ^{16}\text{O}$ Elastic Scattering*. Phys. Rev. Lett., vol. 71, pages 34–37, 1995.

- [Kimura 04] M. Kimura & H. Horiuchi. *Many-Particle and Many-Hole States in Neutron-Rich Ne Isotopes Related to Broken $N=20$ Shell Closure*. Prog. Theor. Phys., vol. 111, page 841, 2004.
- [Kubo 92] T. Kubo *et al.* *The Riken radioactive beam facility*. Nucl. Ins. and Meth. B, vol. 70, pages 309–319, 1992.
- [Kumagai 01] H. Kumagai *et al.* *Delay-line PPAC for high-energy light ions*. Nucl. Ins. and Meth. A, vol. 470, pages 562–570, 2001.
- [Lacroix 99] D. Lacroix, J. A. Scarpaci & Ph. Chomaz. *Theoretical description of the towing mode through a time-dependent quantum calculation*. Nucl. Phys. A, vol. 658, pages 273–281, 1999.
- [Landau 44] L. D. Landau. *On the Energy Loss of Fast Particles by Ionization*. J. Physics (USSR), vol. 8, 1944.
- [Leistenschneider 01] A. Leistenschneider *et al.* *Photoneutron Cross Sections for Unstable Neutron-Rich Oxygen Isotopes*. Phys. Rev. Lett., vol. 86, page 5442, 2001.
- [Lemmon 05] R. C. Lemmon. Private communication, 2005.
- [Leo 94] W. R. Leo. *Techniques for nuclear and particle physics experiments*. Springer, 1994.
- [Ma 97] Z. Ma *et al.* *The Giant Dipole Resonance in Ar-Isotopes in the Relativistic RPA*. Prog. Theor. Phys., vol. 98, pages 917–926, 1997.
- [Margueron 02] Jerome Margueron, Angela Bonaccorso & David M. Brink. *Coulomb-nuclear coupling and interference*

Bibliography

- effects in the breakup of halo nuclei.* Nucl. Phys. A, vol. 703, pages 105–129, 2002.
- [Margueron 03] J. Margueron, A. Bonaccorso & D. M. Brink. *A non-perturbative approach to halo breakup.* Nucl. Phys. A, vol. 720, pages 337–353, 2003.
- [McLean 91] D.J. McLean *et al.* ^{14}C photoproton cross section. Phys. Rev. C, vol. 44, pages 1137–1147, 1991.
- [Michalowicz 64] A. Michalowicz. *Cinématique des réactions nucléaires.* Dunod, 1964.
- [Moyal 55] J.E. Moyal. *Theory of Ionization Fluctuations.* Phil. Mag., vol. 46, page 263, 1955.
- [Nakamura 97] T. Nakamura *et al.* *Coulomb excitation of ^{11}Be .* Phys. Lett. B, vol. 394, pages 11–15, 1997.
- [Nakamura 95] T. Nakamura. *Coulomb excitation of ^{11}Be .* PhD thesis, University of Tokyo, 1995.
- [Nowacki 05] F. Nowacki *et al.* Private communication, 2005.
- [Obertelli 05a] A. Obertelli. *La fermeture de sous couche $N = 16$.* PhD thesis, Université Paris XI, 2005.
- [Obertelli 05b] A. Obertelli *et al.* *$N = 16$ subshell closure from stability to the neutron drip line.* Phys. Rev. C, vol. 71, no. 2, page 024304, 2005.
- [Paar 05] N. Paar, D. Vretenar & P. Ring. *Proton Electric Pygmy Dipole Resonance.* Phys. Rev. Lett., vol. 94, page 182501, 2005.
- [Palit 03] R. Palit *et al.* *Exclusive measurement of breakup reactions with the one-neutron halo nucleus ^{11}Be .* Phys. Rev. C, vol. 68, page 034318, 2003.

-
- [Péru 05] S. Péru *et al.* Private communication, 2005.
- [Pritychenko 99a] B.V. Pritychenko. *Intermediate-Energy Coulomb Excitation of the Neutron-Rich Radioactive Isotopes $^{26,28}\text{Ne}$, $^{28-31}\text{Na}$, $^{30-34}\text{Mg}$, $^{34,35}\text{Al}$, ^{33}Si and ^{34}P* . PhD thesis, Michigan State University, 1999.
- [Pritychenko 99b] B.V. Pritychenko *et al.* *Role of intruder configurations in $^{26,28}\text{Ne}$ and $^{30,32}\text{Mg}$* . Phys. Lett. B, vol. 461, pages 322–328, 1999.
- [Puhlhofer 77] F. Puhlhofer. *On the interpretation of evaporation residue mass distributions in heavy-ion induced fusion reactions*. Nucl. Phys. A, vol. 280, pages 267–284, 1977.
- [Raynal 97] J. Raynal. *ECIS-97*. Unpublished, 1997.
- [Reed 99] A. T. Reed *et al.* *Radioactivity of neutron-rich oxygen, fluorine, and neon isotopes*. Phys. Rev. C, vol. 60, page 024311, 1999.
- [Reinhard 99] P. G. Reinhard. *Skyrme forces and giant resonances in exotic nuclei*. Nucl. Phys. A, vol. 649, pages 305–314, 1999.
- [Ring 05] P. Ring *et al.* Private communication, 2005.
- [Rodríguez-Guzmán 03] R.R. Rodríguez-Guzmán, J.L. Egido & L.M. Robledo. *Quadrupole collectivity of neutron-rich neon isotopes*. Eur. Phys., vol. 17, page 37, 2003.
- [Roussel-Chomaz 88] P. Roussel-Chomaz *et al.* *^{16}O elastic scattering at $E_{\text{lab}} = 94 \text{ MeV}/n$* . Nucl. Phys. A, vol. 477, pages 345–364, 1988.

Bibliography

- [Sagawa 90] H. Sagawa & M. Honma. *Sum rule approach to decoupled giant dipole state*. Phys. Lett. B, vol. 251, pages 17–22, 1990.
- [Sagawa 04] H. Sagawa *et al.* *Deformations and electromagnetic moments in carbon and neon isotopes*. Phys. Rev. C, vol. 70, page 054316, 2004.
- [Satchler 83] G. R. Satchler. *Direct nuclear reactions*. Oxford University Press, 1983.
- [Scheit 98] H. Scheit. *Low-Lying Collective Excitations in Neutron-Rich Even-Even Sulfur and Argon Isotopes Studied via Intermediate-Energy Coulomb Excitation and Proton Scattering*. PhD thesis, Michigan State University, 1998. Also available as www.nsc1.msu.edu/ourlab/library/publications/thesis.php?file=Scheit1998_146.pdf.
- [Steinwedel 50] H. Steinwedel & J. H. D. Jensen. *Hydrodynamik Von Kerndipolschwingungen*. Z. Naturforsch, vol. 5a, page 413, 1950.
- [Suomijärvi 89] T. Suomijärvi *et al.* *Excitation of giant resonance in $^{20}\text{Ne}+^{90}\text{Zr}$ and ^{208}Pb inelastic scattering at 40 MeV/u*. Nucl. Phys. A, vol. 491, page 314, 1989.
- [Suomijärvi 90] T. Suomijärvi *et al.* *Excitation of Giant Resonances in Heavy-Ion Reactions at Intermediate Energies: Results from the $^{40}\text{Ar}+^{90}\text{Zr}$ and ^{208}Pb experiments at 41 MeV/u*. Nucl. Phys. A, vol. 509, page 369, 1990.

-
- [Suzuki 90] Y. Suzuki *et al.* *New type of dipole vibration in Nuclei.* Prog. Theor. Phys., vol. 83, page 180, 1990.
- [Suzuki 01] T. Suzuki *et al.* *Low-energy dipole modes in Unstable nuclei.* Prog. Part. Nucl. Phys., vol. 46, page 135, 2001.
- [Taddeucci 90] T.N. Taddeucci *et al.* *Zero-degree cross sections for the ${}^7\text{Li}(p,n){}^7\text{Be}(g.s.+0.43\text{ MeV})$ reaction in the energy range 80-795 MeV.* Phys. Rev. C, vol. 41, page 2548, 1990.
- [Takeuchi 02] S. Takeuchi *et al.* *Development of NaI(Tl) detector for array in-beam γ -ray spectroscopy.* RIKEN Accel. Prog. Rep., vol. 36, pages 148–149, 2002.
- [Triggstad 01] E. Triggstad *et al.* *Dipole strength function in ${}^{20}\text{O}$.* Nucl. Phys. A, vol. 687, page 231c, 2001.
- [Van Der Woude 01] A. Van Der Woude & M.N. Harakeh. *Giant resonances: Fundamental high-frequency modes of nuclear excitation.* Oxford University Press, 2001.
- [Van Isacker 92] P. Van Isacker *et al.* *Effect of the neutron skin on collective states of nuclei.* Phys. Rev. C, vol. 45, page R13, 1992.
- [Varlamov 00] V.V. Varlamov & M.E. Stepanov. *The giant dipole resonance decay main channels analysis and photoneutron and photoproton reaction cross sections evaluation for ${}^{20,22}\text{Ne}$.* Bull. Rus. Acad. Sci. Phys., vol. 64, page 491, 2000. Obtained via EXFOR.
- [Weiszäcker 34] C.F. Weiszäcker. Z. Phys., vol. 88, page 612, 1934.

Bibliography

- [Wilcox 73] R. H. Wilcox *et al.* *New Spectroscopic Measurements via Exotic Nuclear Rearrangement: The Reaction $^{26}\text{Mg}({}^7\text{Li}, {}^8\text{B})^{25}\text{Ne}$* . Phys. Rev. Lett., vol. 30, page 866, 1973.
- [Williams 34] E.J. Williams. Phys. Rev., vol. 45, page 729, 1934.
- [Winger 92] J. A. Winger *et al.* *INTENSITY: a computer program for the estimation of secondary beam intensities from a projectile fragment separator*. Nucl. Ins. and Meth. B, vol. 70, pages 380–392, 1992.
- [Winther 79] A. Winther & K. Alder. *Relativistic Coulomb Excitation*. Nucl. Phys. A, vol. 319, page 518, 1979.
- [Woods 85] C. L. Woods *et al.* *A study of ^{25}Ne via the $^{26}\text{Mg}({}^{13}\text{C}, {}^{14}\text{O})^{25}\text{Ne}$ reaction*. Nucl. Phys. A, vol. 437, page 454, 1985.
- [Yamada 01] K. Yamada *et al.* *RF Deflector System for RI Beams on RIPS*. RIKEN Accel. Prog. Rep., vol. 34, page 201, 2001.
- [Yamada 04] K. Yamada *et al.* *E1 strength of the subthreshold $3/2^+$ state in ^{15}O studied by Coulomb excitation*. Phys. Lett. B, vol. 579, pages 265–270, 2004.
- [Yano 89] Y. Yano. *Status report on RIKEN Ring Cyclotron*. In Martin B. & Ziegler K., editors, Proc. 12th Int. Conf. on Cyclotrons and their Applications, Berlin, page 13. World Scientific, 1989.
- [Zegers 99] R.G.T. Zegers. *Search for isovector giant monopole resonances*. PhD thesis, Rijksuniversiteit Groningen, 1999.

Résumé

Nous avons effectué l'excitation Coulombienne, sur une cible de plomb, d'un faisceau exotique à 58 MeV/nucéron de ^{26}Ne , noyau riche en neutrons, afin d'étudier la possible existence de résonances dipolaires pygmées au dessus du seuil d'émission neutron. L'expérience a été conduite auprès de l'accélérateur de l'institut RIKEN, à Tokyo (Japon) et incluait un détecteur de gammas, un hodoscope pour particules chargées et un détecteur de neutrons. A l'aide de la méthode de la masse invariante appliquée dans la voie de décroissance $^{25}\text{Ne}+n$, et en comparant la section efficace de réaction sur le plomb et sur une cible légère d'aluminium, nous observons de la force de moment angulaire égal à un entre les seuils d'émission un neutron et deux neutrons. A l'aide des distributions angulaire de diffusion du ^{26}Ne nous en confirmons la nature et extrayons la valeur de probabilité de transition réduite dipolaire correspondante $B(E1) = 0.54 \pm 0.18 \text{ e}^2\text{fm}^2$. Notre méthode nous permet aussi d'accéder pour la première fois aux rapports d'embranchement de la décroissance d'une résonance pygmée. Par ailleurs, en détectant les photons de décroissance des états au-dessous du seuil d'émission neutron et en analysant les distributions angulaires de diffusion du ^{26}Ne correspondant au premier état excité 2^+ , nous en déduisons sa probabilité de transition réduite, à partir de l'état fondamental. La valeur obtenue de $B(E2) = 87 \pm 13 \text{ e}^2\text{fm}^4$ est en désaccord avec le résultat d'une expérience précédente.

Abstract

We carried out the Coulomb excitation, on a lead target, of an exotic beam of neutron-rich nucleus ^{26}Ne at 58 MeV/n, in order to study the possible existence of a pygmy dipole resonance above the neutron emission threshold. The experiment was performed at the RIKEN Research Facility, in Tokyo (Japan) and included a gamma-ray detector, a charged fragment hodoscope and a neutron detector. Using the invariant mass method in the $^{25}\text{Ne}+n$ decay channel, and by comparing the reaction cross section on the lead target and a light target of aluminum, we observe a sizable amount of E1 strength between the one neutron and the two neutron emission thresholds. The corresponding ^{26}Ne angular distribution confirms its nature and we deduce its reduced dipole transition probability value of $B(E1) = 0.54 \pm 0.18 \text{ e}^2\text{fm}^2$. Our method also enables us to extract for the first time the decay pattern of a pygmy resonance. By detecting the decay photons from the excited states below the neutron emission threshold and by analyzing the angular distribution of the inelastically scattered ^{26}Ne we deduce the reduced transition probability of the first 2^+ state, from the ground state. The value obtained of $B(E2) = 87 \pm 13 \text{ e}^2\text{fm}^4$ being in disagreement with a previous result.